Mécanismes d'endommagement du polyamide-66 renforcé par des fibres de verre courtes, soumis à un chargement monotone et en fatigue : Influence de l'humidité relative et de la microstructure induite par le moulage par injection

Muhamad Fatikul Arif

Muhamad Fatikul Arif. Mécanismes d'endommagement du polyamide-66 renforcé par des fibres de verre courtes, soumis à un chargement monotone et en fatigue : Influence de l'humidité relative et de la microstructure induite par le moulage par injection. Mécanique des matériaux [physics.class-ph]. Ecole nationale supérieure d'arts et métiers - ENSAM, 2014. Français. NNT : 2014ENAM0008 . pastel-01064878

HAL Id: pastel-01064878
https://pastel.hal.science/pastel-01064878

Submitted on 17 Sep 2014

2014-ENAM-0008

École doctorale n° 432 : Science des Métiers de l'Ingénieur

Doctorat ParisTech

THÈSE

pour obtenir le grade de docteur délivré par

l'École Nationale Supérieure d'Arts et Métiers

Spécialité “ Mécanique et Matériaux ”

présentée et soutenue publiquement par

Muhamad Fatikul ARIF

le 25 mars 2014

Damage mechanisms in short glass fiber reinforced polyamide-66 under monotonic and fatigue loading: Effect of relative humidity and injection molding induced microstructure

Directeur de thèse : **Fodil MERAGHNI**
Co-encadrement de la thèse : **Joseph FITOUSSI** et **Nicolas SAINTIER**

Jury

M. Habibou MAITOURNAM, Professeur, LMS, École Polytechnique	Président
M. André CHRYSOCHOOS, Professeur, LMGC, Université Montpellier 2	Rapporteur
M. Cetin Morris SONSINO, Professeur, Fraunhofer LBF, TU Darmstadt (Allemagne)	Rapporteur
M. Lucien LAIARINANDRASANA, Maître de recherches (HDR), MAT, Mines ParisTech	Examinateur
M. Gilles ROBERT, Docteur, Solvay Engineering Plastics - Lyon	Examinateur
M. Fodil MERAGHNI, Professeur, LEM3, Arts et Métiers Paristech - Metz	Examinateur
M. Joseph FITOUSSI, Maître de conférences, PIMM, Arts et Métiers Paristech - Paris	Examinateur
M. Nicolas SAINTIER, Maître de conférences (HDR), I2M, Arts et Métiers Paristech - Bordeaux	Examinateur
M. Yves CHEMISKY, Maître de conférences, LEM3, Arts et Métiers Paristech - Metz	Invité

THÈSE

Arts et Métiers ParisTech - Centre de Metz
Laboratoire d'Etude des Microstructures et Mécanique des Matériaux (LEM3)

Avant-propos

Ce manuscrit de thèse présente les approches expérimentales dédiées à l'investigation de l'endommagement ainsi que les résultats marquant des premiers travaux de recherche menés dans le cadre du projet DURAFIP, FUI-DGCIS. La finalité de celui-ci est de proposer des outils fondés sur un modèle multiéchelles en vue du dimensionnement en fatigue de pièces automobiles, en particulier celles faites en polyamide-66 renforcé par des fibres de verre courtes sous chargement multiaxial. Cette démarche permettra d'aboutir à une conception fiable de ces composants automobiles, notamment en fatigue, validera le développement de ce matériau dans une dynamique de réduction du coût et du poids des véhicules.

Le travail effectué dans le cadre de cette thèse est considéré comme la première pierre du projet DURAFIP, posée par le groupe de recherche des Arts et Métiers ParisTech. Il se caractérise sur une vaste approche expérimentale menant à l'identification des mécanismes d'endommagement en monotone et en fatigue du polyamide-66 renforcé à 30% en masse par des fibres de verres courtes, obtenu par moulage à injection (PA66/GF30), en prenant en compte l'influence de la teneur en eau et de la microstructure induite par le procédé de fabrication.

Le manuscrit est principalement écrit en anglais mais comporte une version abrégée en français. Ce document est donc divisé en deux parties : le résumé en français **(Partie I)** puis un rapport détaillé en anglais du travail de recherche réalisé **(Partie II)**.

Preface

This thesis manuscript presents experimental approaches on damage analysis, as well as the important results of the initial research work carried out under the context of DURAFIP, FUI-DGCIS project. The purpose this project is to propose tools based on a multiscale model for fatigue design of automotive parts, especially those made of short glass fiber reinforced polyamide-66 under multiaxial loading. This approach will lead to a reliable design of such automotive components, notably under fatigue loading, that will validate the development of this material towards cost and weight reduction of vehicles.

The current work is considered as the first phase of DURAFIP project undertaken by the research group of Arts et Métiers ParisTech. The work focuses on extensive experimental approaches to identify monotonic and fatigue damage behavior of injection molded 30 wt% short glass fiber reinforced polyamide-66 (PA66/GF30), considering effects of relative humidity and injection process induced microstructure.

The manuscript is mainly written in English, with an extended summary in French. Therefore, this document is divided into two parts: an extended summary in French **(Part I)** and a detailed report of the current research work in English **(Part II)**.

To my daughter, Nadya.

Acknowledgements

I would like to express my sincere gratitude to Pr. Fodil Meraghni, my thesis director and main supervisor, for his guidance and support, and for providing me with numerous opportunities for professional growth and development. His enthusiasm and friendly attitude made my stay in doctoral school a wonderful experience. His patience, availability and flexible supervising time have been the driving force in my ability to finish the doctoral studies. I have learned a great deal from him, and I am truly grateful. I owe my sincere gratitude to Nicolas Saintier, my co-supervisor, for the valuable discussions and for the fruitful one month experimental work in Bordeaux. I am really grateful to Joseph Fitoussi, my co-supervisor, for his valuable time and his technical guidance, who always welcomed us enthusiastically during our frequent group meetings in Paris. I would like to thank all my supervisors, for their generosity and willingness to send me to international conferences, where I could learn about recent advances in my field and meet well known scientists around the world. I am also grateful for the opportunities they gave to attend and present our research work at several steering committee meetings of the DURAFIP project, which allowed me to see the project from a broader perspective. These experiences will undoubtedly be beneficial in my future professional endeavors.

Many people apart from my supervisors have also contributed to my advancement throughout my doctoral studies at Arts et Métiers ParisTech. First and utmost, sincere thanks to Gilles Robert, who provided me valuable data and knowledge about the properties and behavior of the studied material, helped me with great passion on tomography technique and warmly welcomed me for a one week study in Solvay Engineering Plastics, Lyon. I also profited greatly from valuable interactions with Yves Chemisky during the fruitful discussions on data analysis and paper writing. Moreover, I highly appreciate for his rigorous assistance during my individual study on micromechanical modeling and its implementation into C++ coding. This work is also benefitted from the comments and corrections from the jury members; Pr. Moris Sonsino, Pr. André Chrysochoos, Pr. Habibou Maitournam and M. Lucien Laiarinandrasana, for which I am truly grateful.

I would also like to thank Nicolas Despringre, the PhD student of DURAFIP project, for the good times, valuable discussions and for helping me in numerous occasions. Many thanks are also due to Héloïse Rolland, the PhD student of DURAFIP project, for the fruitful discussion on tomography results. I would also like to express my gratitude towards Nadine Bourgeois, who took the time to accompany and teach me meticulously during digital image correlation (DIC) experiments. Special thanks to Laurent Peltier and Patrick Moll, for the great assistance throughout the experimental tasks during my study in Metz. I would also like to express my appreciation to Marc Wary. All the SEM images presented in this work are available due to his great assistance. I would like to thank Boris Piotrowski, who assisted me with great care on various tasks such as knowledge on coding, software error handling and some administrative issues.

I have enjoyed interacting with numerous friends at Arts et Métiers ParisTech – Centre de Metz. I have met a lot of caring and concerned friends in this school. They provided me with immeasurable help, advices, and encouragement. I am thankful to all of them for the good times we spent together during the coffee break, lunch time and weekend leisure. I will forever cherish our friendship. I feel lucky to count among my friends; Rachid E, Dimitris C, Dimitris A, George C, Stephen C, Akbar G, Lotfi M, Francis A, Abderrahim N, Thomas A, Koffi A, Celia C, Oussama E, Fedia M, Célestin B, Ammar G, Tanh Hung N, Armaghan K, Liaqat S, Abdelwahed B, Nejah J and Zhongkai C.

As a final note, I would like to express my gratitude and appreciation to my parents for their inspiration, prayer and endless support. I am indebted to my wife for her encouragement, immense patience and love, and for giving me our beautiful daughter Nadya, whose smile has always lifted my spirits.

Contents

List of Figures

List of Tables

Part I

Résumé étendu

Introduction générale

La réduction de la masse d'un véhicule est une préoccupation majeure de l'industrie automobile, afin notamment de réduire les émissions de CO_2 vis-à-vis d'une politique de régulation de la pollution. Les matériaux thermoplastiques renforcés par fibres courtes, parmi lesquels se trouve le polyamide-66 renforcé par des fibres de verre courtes, sont alors de bons candidats pour fournir un compromis entre la légèreté requise et les performances thermomécaniques attendues. Cependant, leur durabilité n'est pas encore pleinement étudiée ni maîtrisée, en particulier en ce qui concerne le comportement en fatigue de ces composites. Un travail est donc requis afin de déterminer le scénario des mécanismes d'endommagement en vue d'une modélisation à fort contenu physique du comportement en fatigue.

Le projet DURAFIP, FUI-DGCIS voit ainsi le jour. Ce dernier est mené par Solvay Engineering Plastics et rassemble 14 partenaires industrielles et académiques. Le but final de ce projet est d'étendre la modélisation multiéchelles à la fatigue afin de pouvoir prédire le comportement de pièces structurelles en composite, et en particulier celles faites en polyamide-66 renforcé de fibres de verre courtes. Une conception solide des composants intégrant le comportement en fatigue est particulièrement importante car beaucoup de pièces automobiles sont sujettes à un chargement répété, comme par exemple celles situées près du moteur subissant les vibrations de ce dernier, ou encore les composants structurelles supportant les vibrations du châssis. Une telle modélisation multiéchelles nécessite une approche expérimentale menée aux échelles pertinentes et permettant la caractérisation du comportement du composite ainsi que les interactions entres ses différentes phases ou constituants. A noter que le procédé de fabrication, à savoir le moulage par injection, contribue largement à plusieurs caractéristiques du polyamide-66 renforcé par des fibres de verre courtes, tels que l'orientation des fibres, le comportement viscoélastique-viscoplastique de la matrice, l'initiation et la propagation de l'endommagement, le taux de chargement ainsi que les conditions environnementales (i.e. température et humidité relative).

Le travail effectué dans le cadre de cette thèse est considéré comme la première pierre du projet DURAFIP, posée par le groupe de recherche des Arts et Métiers ParisTech. Il se caractérise par une vaste approche expérimentale menant à l'identification des mécanismes d'endommagement en fatigue du polyamide-66 renforcé à 30% en masse par des fibres de verres courtes, obtenu par moulage à injection (PA66/GF30) ; en ayant toujours à l'esprit les nombreux effets influençant la durée de vie en fatigue telles que l'humidité relative et la microstructure induite par le procédé de fabrication. Les mécanismes d'endommagement du PA66/GF30 ont également été étudiés sous chargement monotone afin de renforcer la compréhension du comportement endommageable de ce matériau. Dans le cadre de cette étude, plusieurs techniques expérimentales ont été mises en œuvre pour étudier l'endommagement du PA66/GF30 : l'exploitation de données résultant de tests mécaniques à échelle macroscopique, de la thermographie infrarouge ou encore de la micro-tomographie aux rayons X assistée par ordinateur (μCT).

Les résultats de cette étude sur les mécanismes d'endommagement, ainsi que ceux à venir de la thèse en cours d'H. Rolland sur l'endommagement en fatigue du PA66/GF30 pour des conditions hygrométriques variées et sous chargement à amplitude variable, seront implémentés dans un modèle prédictif micromécanique intégrant la fatigue. Cette modélisation est en cours de réalisation dans le cadre de la thèse de N. Despringre. Le modèle ainsi développé prendra en compte la cinétique d'endommagement à l'interface fibre/matrice couplée à la rhéologie visqueuse de la matrice polyamide, le tout associé à la microstructure du PA66/GF30.

Ce rapport est organisé en quatre parties majeures :

- Le matériau composite et la microstructure induite par le procédé de fabrication
- Comportement mécanique globale et endommagement du PA66/GF30
- Etude in-situ des mécanismes d'endommagement du PA66/GF30
- Caractérisation multiéchelles de l'endommagement en fatigue du PA66/GF30

Les conclusions et perspectives de ce travail seront ensuite résumées.

Le matériau composite et la microstructure induite par le procédé de fabrication

Le matériau utilisé dans ce travail est le Technyl A218V30, une dénomination commerciale du PA66/GF30 que fournit par Solvay Engineering Plastics-France. Il est préparé en combinant des granules de polyamide-66 avec des fibres de verre courtes taillées, à hauteur de 30% en masse et à l'aide d'une extrudeuse à double hélice. Le mélange est ensuite envoyé vers la machine de moulage par injection qui permet la fabrication d'une plaque rectangulaire de $360 \times 100 \times 3.2$ mm^3.

Une microstructure hétérogène selon l'épaisseur du matériau est couramment observée avec ce procédé de fabrication. Afin d'étudier celle du PA66/GF30, la technique de μCT est utilisée. Ces expériences ont été menées à la ligne ID19 de l'ESRF (European Synchrotron Radiation Facility) à Grenoble (France) [ID19 ESRF]. Pour pouvoir observer la microstructure, le matériel a été calibré de manière à atteindre une résolution en voxel de 1.4 μm. Deux échantillons A et B ont été prélevés à deux positions de la plaque d'injection, dans le sens de la direction d'écoulement (MFD), comme montré par la Fig. 1. Ces emplacements ont été choisis relativement loin des extrémités de la plaque d'injection, où le flux de remplissage est complexe ce qui y provoque généralement une microstructure non-uniforme et non représentative du matériau étudié. Les dimensions de ces échantillons sont de $2 \times 2 \times 3.2$ mm^3, 3.2 mm étant l'épaisseur.

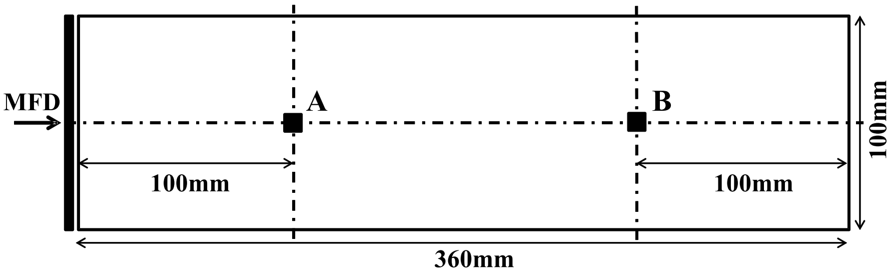

FIGURE 1: Positions A et B de prélèvement des échantillons sur la plaque injectée, pour les études de microstructure.

La microstructure du PA66/GF30, obtenue par μCT de l'échantillon A de la Fig. 1, est présentée sur la Fig. 2. On y observe que le PA66/GF30 possède une microstructure caractéristique du procédé d'injection, représentée par une structure cœur-peau-surface. De plus, on observe également une couche de transition entre le cœur et la peau. La microstructure issue de la position B de la Fig. 1 est similaire à celle de l'emplacement A. A noter que cette configuration microstructurale à l'échelle microscopique a été obtenue grâce à une optimisation des paramètres d'injection (températures du moule et du cylindre d'injection, vitesse d'injection, etc.), qui assure un compactage élevé du composite et réduit l'épaisseur de la couche à cœur.

Afin d'obtenir les variations réelles de l'orientation des fibres dans l'échantillon, le tenseur d'orientation à différentes épaisseurs a été calculé à partir des résultats issus de

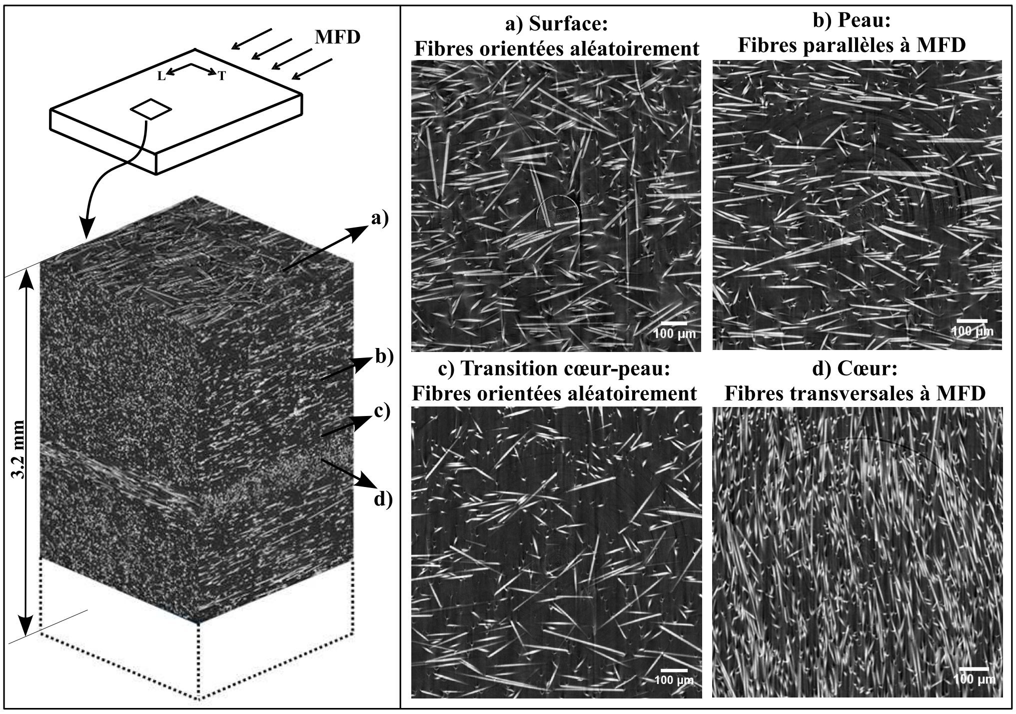

FIGURE 2: Observation de la microstructure cœur-peau-surface du PA66/GF30 par μCT.

la μCT. Une méthode adaptée de segmentation des fibres sur les images 3D récoltées par μCT a été mise au point pour récupérer les angles d'Euler des fibres, en utilisant un seuillage par niveau de gris. Les logiciels utilisés à cet effet sont Avizo et Visilog. Une fois le processus de seuillage terminé, on peut extraire une reconstruction 3D des fibres ainsi que leurs caractéristiques, dont leurs angles d'Euler. Les tenseurs d'orientation des fibres du second ordre ont été calculés à l'aide de ces données. A noter que le traitement numérique d'obtention des tenseurs d'orientation a été réalisé par le partenaire industriel. C'est pourquoi toutes les procédures associées sont confidentielles et les résultats présentés sont normalisés.

Les tenseurs d'orientation des fibres du second ordre ont été calculés. Les coefficients normalisés des tenseurs des deux volumes étudiés par μCT sont représentés sur la Fig. 3. Les valeurs a_{11}, a_{22} et a_{33} correspondent à l'inclinaison des fibres selon les directions respectivement longitudinale, transverse et transverse courte (suivant l'épaisseur) par rapport à la direction d'écoulement. Plus grande est la valeur normalisée d'un coefficient, plus les fibres ont tendances à s'orienter selon la direction associée. La Fig. 3 met en exergue la structure cœur-peau-surface des deux volumes observés par μCT. Par ailleurs, les fines couches de transitions entre cœur et peau sont également observables.

En se basant sur ces analyses qualitatives et quantitatives de la microstructure du PA66/GF30, on remarque que les couches surfaciques supérieure et inférieure des échantillons ont une orientation des fibres plutôt aléatoire. Cependant, les coefficients a_{11} des tenseurs d'orientations pour les positions A et B montrent que les fibres en surface tendent

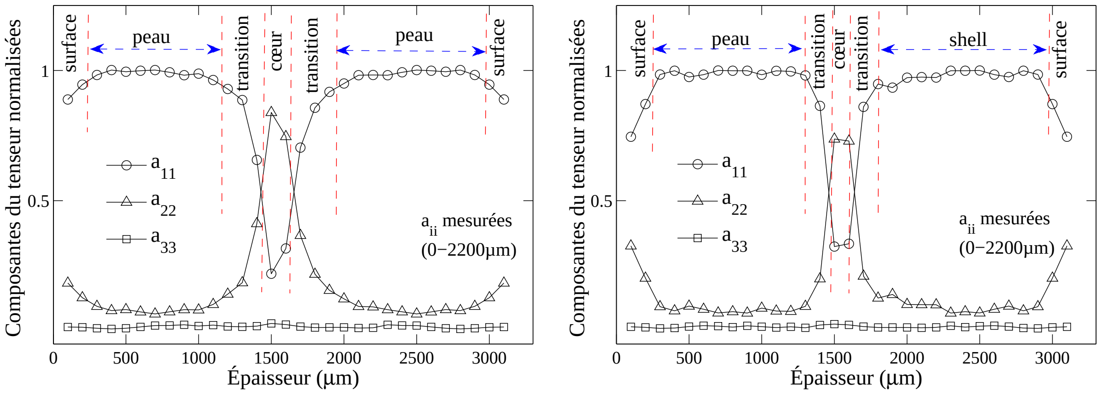

(a) Echantillon extrait de l'emplacement A

(b) Echantillon extrait de l'emplacement B

FIGURE 3: Coefficients normalisés a_{11}, a_{22} et a_{33} du tenseur d'orientation, le long de l'épaisseur des deux échantillons étudiés.

à s'orienter selon la direction d'écoulement. La couche intermédiaire (peau) est la plus dominante avec une orientation préférentielle des fibres selon la direction d'écoulement. La couche à cœur est mince et la plupart des fibres sont orientées perpendiculairement à la direction d'écoulement. A noter que les fibres ne sont pas strictement orientées transversalement par rapport à cette direction, mais forment plutôt un angle compris entre 5^o et 20^o avec celle-ci, comme représenté sur la Fig. 2d. Cela se remarque également au niveau du tenseur d'orientation des fibres à cœur, de par la valeur non nulle du coefficient a_{12}, comme le montre la Fig. 4. En plus de la microstructure cœur-peau-surface, on peut également observer les couches de transition entre cœur et peau tel que sur les Figs. 2c et 3.

Les tenseurs d'orientation normalisés des deux échantillons étudiés révèlent que les deux emplacements ont pratiquement la même configuration des fibres. Seules quelques petites différences sont notables, dont la largeur des zones de transition cœur-peau et l'orientation des fibres en surface. Il peut donc être affirmé que les microstructures développées selon l'axe d'écoulement sont globalement homogènes dans la plaque moulée par injection.

Le présent travail sur la microstructure du PA66/GF30 fournit une ligne directrice à de futures études sur son influence sur le comportement mécanique du composite. Les échantillons utilisés pour les essais de traction et de fatigue ont été usinés sur les plaques rectangulaires produites en moulage par injection. Afin de considérer l'anisotropie du composite, les éprouvettes ont été découpées soit longitudinalement soit transversalement à la direction d'écoulement, donnant la dénomination d'échantillon longitudinal ou transverse. Afin de garantir une microstructure homogène sur toutes les éprouvettes, la zone utile de ces dernières se trouve au niveau de l'axe d'écoulement. De plus, elles ont été prélevées loin des extrémités de la plaque, où les conditions de remplissage du moule

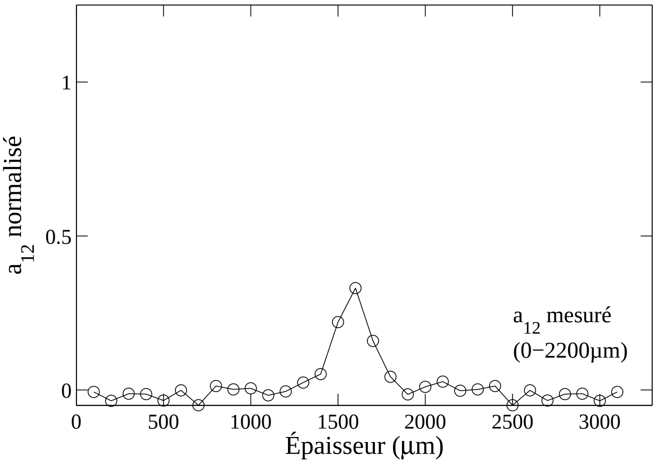

FIGURE 4: Coefficients normalisés a_{12} du tenseur d'orientation à l'emplacement A de la plaque injectée, le long de l'épaisseur.

ne garantissent pas une microstructure uniforme (flux complexe du polymère fondu en début et fond de moule). L'usinage des éprouvettes longitudinales et transverses et leurs dimensions sont illustrées sur la Fig. 5. Pendant les essais mécaniques, les deux types d'éprouvettes ont été sélectionnées de manière aléatoire par rapport à ces positions.

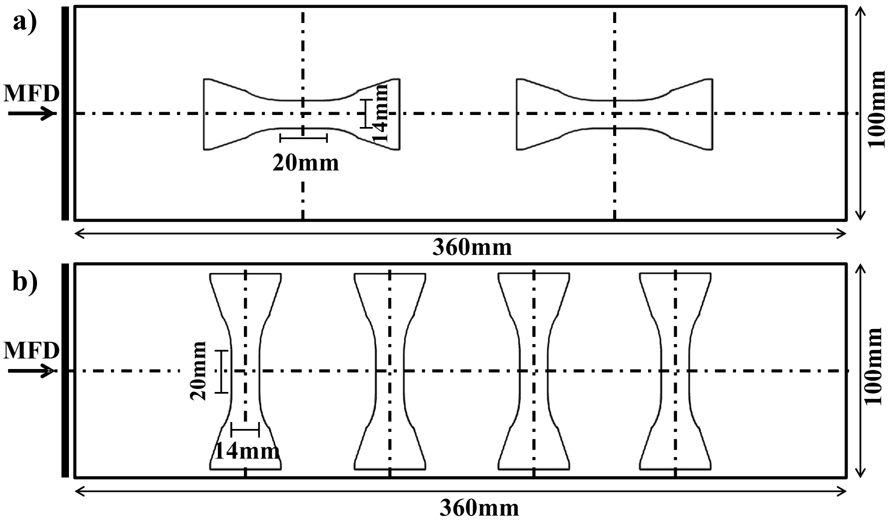

FIGURE 5: Emplacements des éprouvettes de PA66/GF30 a) longitudinales et b) transverses, avec les principales dimensions de celles-ci.

Comportement mécanique globale et endommagement du PA66/GF30

Dans cette partiex, le comportement et les propriétés mécaniques du PA66/GF30 sont étudiées, ainsi que ses mécanismes d'endommagement. La microstructure cœur-peau-surface caractéristique de ce matériau – la peau étant la couche prédominante – offre une forte anisotropie du comportement. Les Figs. 6 and 7 illustrent ce point en montrant les différences de propriétés mécaniques et du comportement anisotrope (dans le plan) entre les échantillons longitudinaux et transverses.

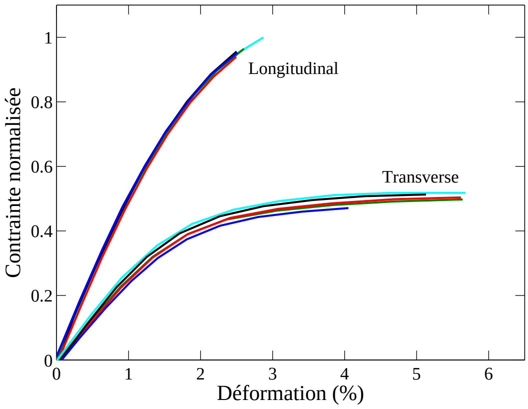

FIGURE 6: Propriétés relatives à la traction des échantillons de PA66/GF30 longitudinaux et transverses.

Les propriétés du PA66/GF30 sont également très dépendantes de la vitesse de déformation et de la température, comme le montre la Fig. 8. La contrainte à rupture et le module du matériau augmentent avec la vitesse de déformation, alors qu'une température plus élevée les réduit.

Le profil de température du PA66/GF30 en traction, représenté Fig. 9, montre que la température diminue durant la première phase de chargement, pour les éprouvettes transverses et longitudinales. Cela correspond au comportement général d'un solide élastique en traction où la temperature est en opposition de phase par rapport au chargement.

Avec l'augmentation du chargement, le matériau s'endommage progressivement et la température devient constante puis augmente. Le couplage de la rhéologie (propriétés visqueuses) du PA66/GF30 à l'endommagement prend alors effet. Ce couplage se manifeste par une augmentation de la température inhérente à une dissipation de chaleur.

Des tests de traction avec décharges complètes pour plusieurs taux de déformation ont été réalisés. L'hystérésis de chaque cycle charge-décharge est notable et est due aux effets visqueux, que ce soit pour les échantillons transverses ou longitudinaux (Fig. 10). La boucle d'hystérésis peut également être partiellement due à de l'endommagement. Sa pente est alors déterminée et on remarque une baisse du module dans les échantillons

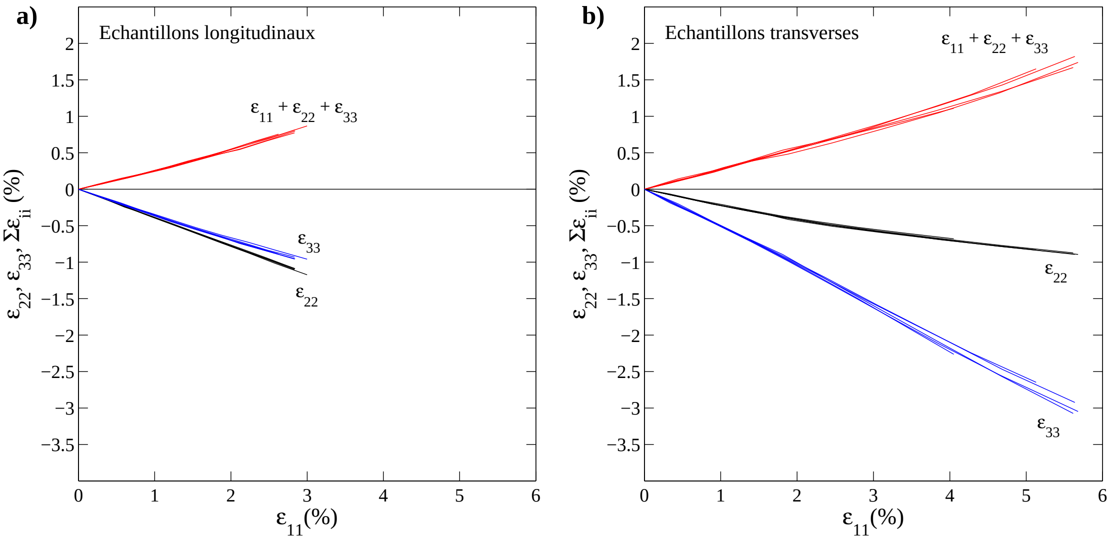

FIGURE 7: Comportement plan anisotrope des échantillons de PA66/GF30 a) longitudinaux et b) transverses, observés pendant des essais de traction le long de l'axe 1. Les axes 2 et 3 représentent respectivement les directions selon la largeur (transverse) et l'épaisseur (transverse court).

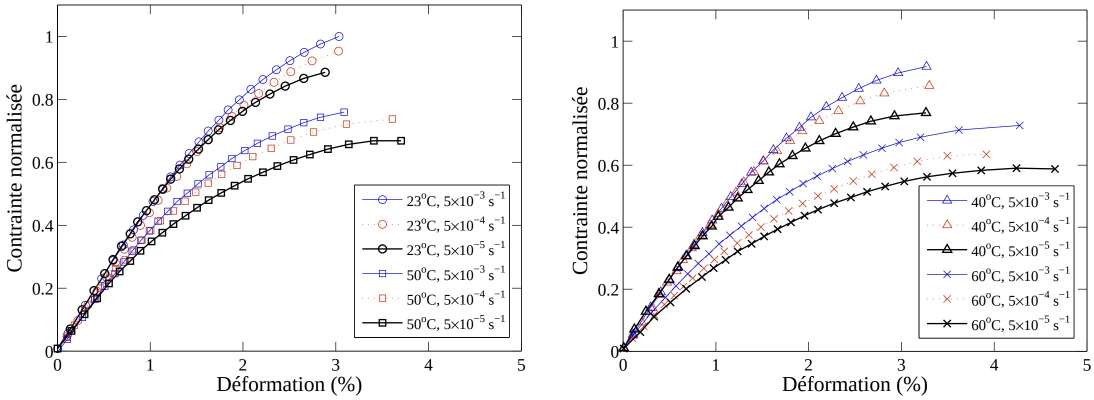

FIGURE 8: Effets de la vitesse de déformation et de la température sur les propriétés mécaniques du PA66/GF30. Deux représentations de la figure sont utilisées pour une meilleure clarté.

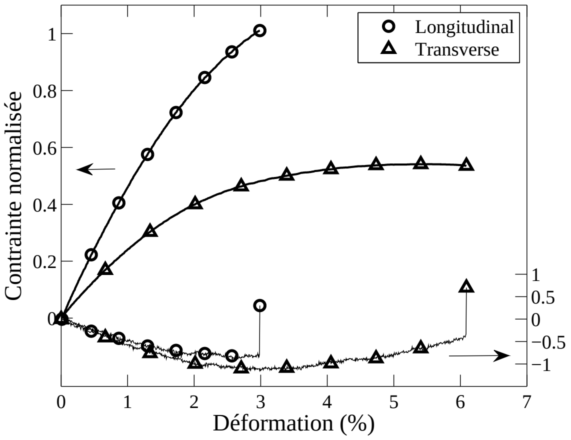

FIGURE 9: Profils de température et courbes contrainte/déformation des échantillons de PA66/GF30 longitudinaux et transverses lors d'un chargement en traction

transverses et longitudinaux. Cette diminution du module peut être attribuée aux effets combinés de l'endommagement et de la viscosité du matériau.

Afin d'observer exclusivement l'endommagement, des tests de tractions avec décharges partielles ont été réalisés et la tangente à la courbe de déchargement a été évaluée. La Fig. 11 représente les diminutions du module en phase dans le cadre de ces essais, qui sont environ moitié plus faibles que celles observées lors d'une décharge complète. On peut alors affirmer que la baisse du module lors des essais en traction avec décharges partielles est majoritairement due à l'endommagement.

Des essais en fatigue ont été menés sur le PA66/GF30 sec, à une fréquence de 3 Hz et avec un rapport de charge de 0.1. Une courbe de Wöhler en a été obtenue, et les valeurs maximales de la vitesse de déformation ont été analysées. S'inscrivant dans la continuité des essais monotones, la résistance en fatigue des éprouvettes longitudinales est environ deux fois plus grande que celle des éprouvettes transverses (Fig. 12). Les vitesses de déformation des deux échantillons sont similaires et vont de 7×10^{-2} à 2×10^{-1} s^{-1}, même si leur contrainte maximale est très différente (Fig. 13). Ces valeurs sont bien plus importantes que celles relatives aux essais monotones. Les tests en traction réalisés à une vitesse de déformation environ égale à 10^{-1} s^{-1} mènent à la rupture avant d'atteindre la contrainte à rupture obtenue à plus faible vitesse de déformation.

Des essais de fatigue interrompus ont également été réalisés sur des échantillons longitudinaux secs de PA66/GF30. Le changement de volume du matériau, évalué par corrélation d'images (DIC), est observé pendant la fatigue (Fig. 14). Sa première augmentation pourrait être principalement due à l'expansion du matériau par (visco)élasticité. Les vides et plus généralement l'endommagement apparaîtraient alors pendant une seconde phase, où un changement de volume constant est notable. Une diminution du volume est également observée, et bien qu'elle soit difficilement interprétable, les premiers postulats à ce sujet la relieraient à une augmentation du taux de cristallinité de la matrice.

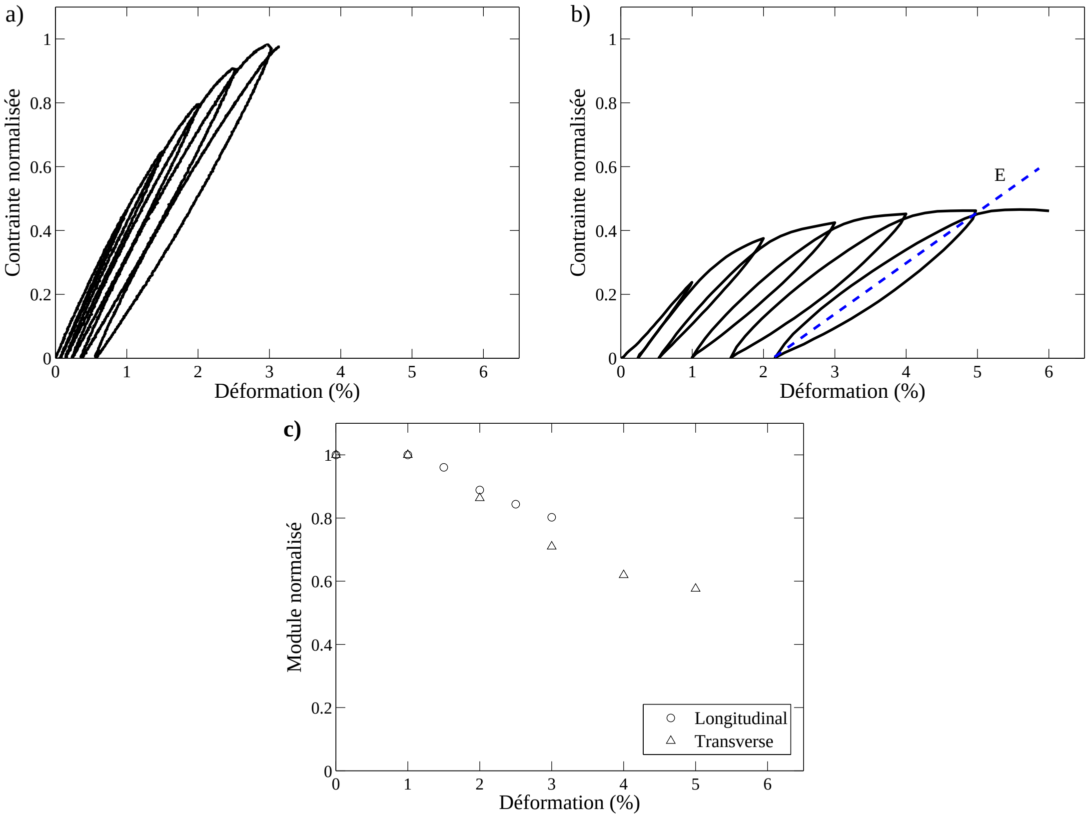

FIGURE 10: Courbes contrainte/déformation des échantillons a) longitudinaux et b) transverses, avec c) l'évolution du module normalisé en essai de traction avec décharges complètes.

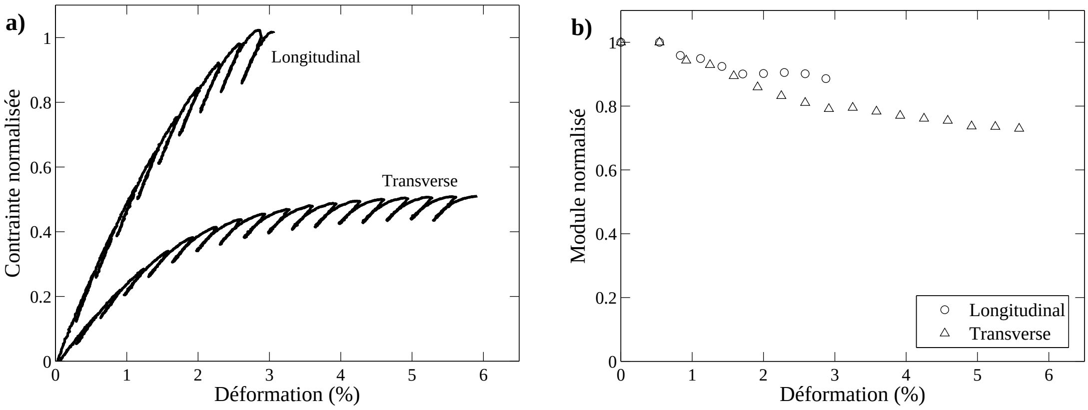

FIGURE 11: Courbe contrainte/déformation (a) et évolution du module normalisé (b) des échantillons longitudinaux et transverses en essai de traction avec décharges partielles.

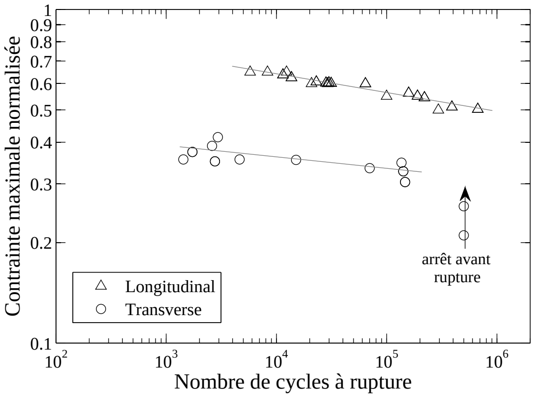

FIGURE 12: Le diagramme *S–N* des échantillons longitudinaux et transverses.

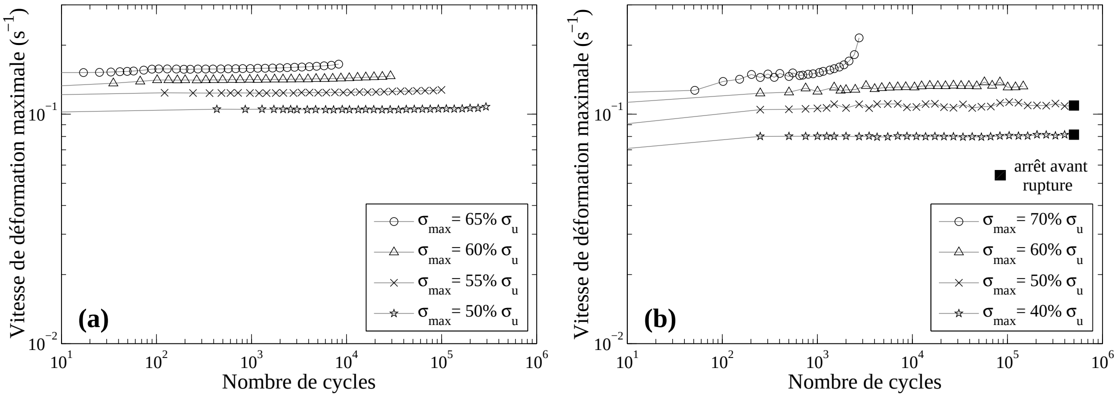

FIGURE 13: Evolution du maximum de la vitesse de déformation des échantillons de PA66/GF30 a) longitudinaux et b) transverses soumis à un essai de fatigue.

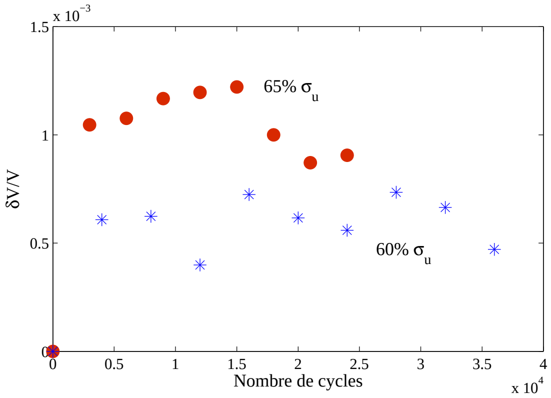

FIGURE 14: Evolution du volume pendant un essai de fatigue sur le PA66/GF30.

En résumé, le PA66/GF30 est un matériau hautement anisotrope dont la viscosité est très influente lors d'un chargement mécanique. Ce travail présente des approches phénoménologiques d'observation de l'endommagement du PA66/GF30 mais jusque-là, les résultats ne sont pas suffisants pour appréhender pleinement les mécanismes d'endommagements. Ainsi, une investigation plus avancée et aux échelles pertinentes a été menée dans le cadre de ce travail de thèse afin de saisir au mieux les mécanismes d'endommagement du PA66/GF30 en chargement monotone, en prenant notamment en compte l'influence de l'humidité relative. De plus, une caractérisation multiéchelles de l'endommagement en fatigue du PA66/GF30 est également étudiée.

Etude in-situ des mécanismes d'endommagement du PA66/GF30 sous chargement monotone quasi-statique : L'effet de l'humidité relative

Un des défis de la conception de composants en polyamide renforcé de fibres de verre courtes vient de la capacité de la matrice en polyamide à absorber l'humidité. La quantité d'eau absorbée dépend des conditions hygrothermiques et influence grandement les propriétés physique, thermique et mécanique du matériau composite.

Bien que l'influence des conditions environnementales sur ces propriétés aient été comprises, aucune étude n'a été réalisée sur l'effet de l'humidité relative (HR) sur les mécanismes endommagement et leurs effets sur le comportement mécanique globale du polyamide renforcé par des fibres de verre courtes. Ainsi, étudier les effets de l'humidité relative est considéré comme important de par son influence sur les propriétés de la matrice et de l'interface fibre/matrice du composite, et donc sur les mécanismes d'endommagement.

Dans ce chapitre, les mécanismes d'endommagement du PA66/GF30 sont analysés via des essais in-situ au MEB sous chargement monotone, avec un montage en flexion 3 points, sur des échantillons conditionnés à trois humidités relatives différentes (HR = 0%, 50% et 100%). Ces derniers ont été usinés à partir de plaques rectangulaires obtenues en moulage par injection, dans le sens longitudinal selon la direction d'écoulement. La zone d'observation correspond à la surface de l'épaisseur du composite, avec une attention particulière à la région en peau soumise à une contrainte de tension. Le chargement de flexion 3 points a pour effet de maximiser la contrainte de tension du côté extérieur de cette région, ce qui permet de réduire la zone d'observation là où l'endommagement maximum est attendu. La validité de ces analyses in-situ est confirmée par μCT sur des échantillons conditionnés à HR = 0% et 50%, après traction uniaxiale.

Les résultats montrent que les mécanismes d'endommagement dans le PA66/GF30 sont profondément affectés par la variation de la teneur en eau. La résistance en flexion diminue lorsque celle-ci augmente, ce qui proviendrait de la combinaison de l'endommagement et des effets de déformation plastique du polyamide (Fig. 15).

Une observation qualitative du nombre de zones où l'endommagement s'initie est également menée sur la surface du composite. Il peut en être conclu que plus l'humidité relative est élevée, plus l'endommagement est important, et ce à toutes les étapes du chargement. De plus, la Fig. 16 montre la comparaison des zones endommagées pour les trois échantillons pour différentes teneur en eau pour une contrainte en flexion proche de celle de la rupture. Il apparaît évident que la quantité de localisation de l'endommagement augmente avec l'humidité relative.

L'initiation de l'endommagement sous la forme d'une décohésion interfaciales fibre/matrice est observée en tête de fibre, ce qui confirme les observations de Sato et. al. [Sato 1984]. Cependant, cette décohésion aux extrémités de fibres n'est pas la seule initiation possible de l'endommagement En effet, l'endommagement s'initie également dans les zones où

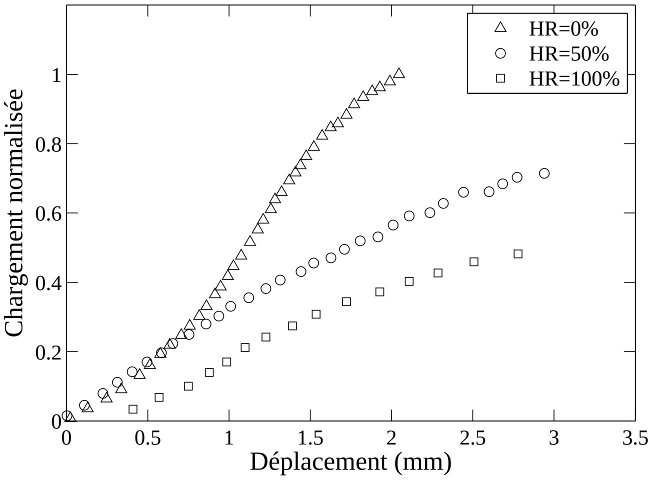

FIGURE 15: Valeurs normalisées du chargement en fonction du déplacement pour des éprouvettes en PA66/GF30 avec différentes humidités relatives (HR).

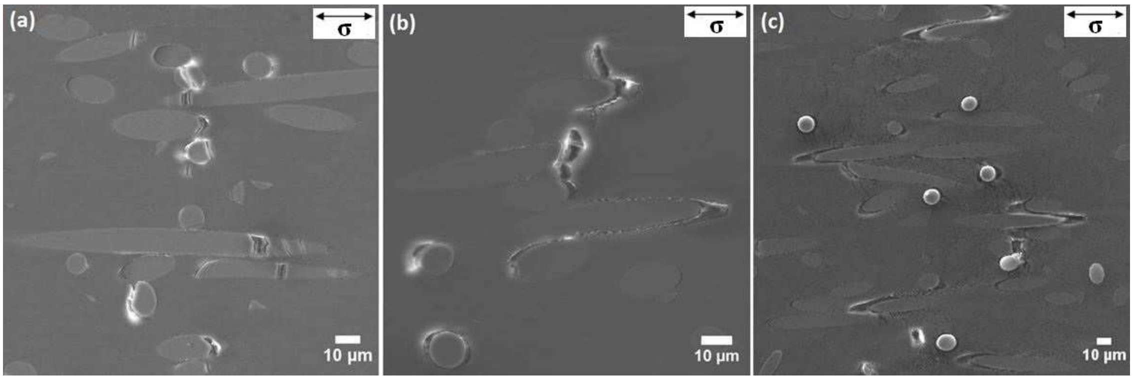

FIGURE 16: Mécanismes d'endommagement du PA66/GF30 pour différentes teneurs en eau, a) ruptures de fibres et microfissures matricielles à 95% de σ_f et à HR = 0%, b) microfissures matricielles à 98% de σ_f et à HR = 50%, c) microfissures et bandes de déformation matricielles à 98% de σ_f et à HR = 100%.

les fibres sont relativement proches les unes des autres. Ce mécanisme a été observé dans tous les échantillons quelle que soit leur teneur en eau. Ces configurations locales sont sources de concentration de contraintes ce qui provoque une apparition précoce de l'endommagement. Plusieurs scénarios de l'initiation de l'endommagement du PA66/GF30 sont alors proposés comme le montre la Fig. 17.

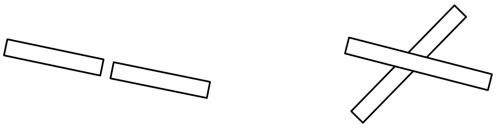

Bout à bout des fibres Corps à corps des fibres

Bout à corps des fibres Fibres parallèles

FIGURE 17: Eventail des scénarios de la localisation de l'endommagement pendant son initiation.

L'initiation de l'endommagement à HR = 0%, 50% et 100% commence à environ 30% de leur résistance en flexion respective. Si ces pourcentages relatifs sont convertis en contraintes normalisées (Fig. 15), on peut remarquer que l'initiation de l'endommagement pour HR = 0%, 50% et 100% commence respectivement à 0.33, 0.21 et 0.15 des valeurs de contraintes normalisées. Cela montre que l'endommagement de l'échantillon sec commence à se développer pour une valeur significativement plus importante du chargement par rapport à ceux conditionnées à HR = 50% et 100%.

Pour l'échantillon sec, l'endommagement reste confiné à certaines zones, et est relativement bas. Il se remarque principalement aux décohésions interfaciales fibre/matrice et aux ruptures de fibres (Fig. 18). Cela indique que l'échantillon sec possède de bonnes propriétés interfaciales comparé aux autres. C'est principalement dû à l'absence d'eau et à une décohésion interfaciales plus faible lors de l'augmentation du niveau de contrainte. Ces bonnes propriétés interfaciales assurent la répartition des contraintes dans les fibres lors du chargement. Cet aspect accentue la probabilité de rupture des fibres et rend alors possible leur observation à partir d'un endommagement correspondant à 33% de σ_f. Comme il ne s'agit que de l'initiation de l'endommagement, le nombre de fibres cassées reste faible. Ceci est courant pour les composites renforcés par des fibres courtes du fait du facteur de forme et de l'orientation des fibres, par rapport à la contrainte macroscopique appliquée et aux champs de contraintes locaux multiaxiaux. A un niveau de contrainte relative en flexion élevé, des microfissures de la matrice thermoplastique se développent dans les zones à forte concentration de fibres (Fig. 16a). Les ruptures de fibres provoquent une redistribution des contraintes dans la matrice ainsi que dans les fibres environnantes. Comme les fibres sont très proches, la concentration des contraintes peut provoquer la microfissuration de la matrice ainsi que la rupture de fibres adjacentes. Ces microfissures se propagent ensuite de manière fragile (Fig. 20).

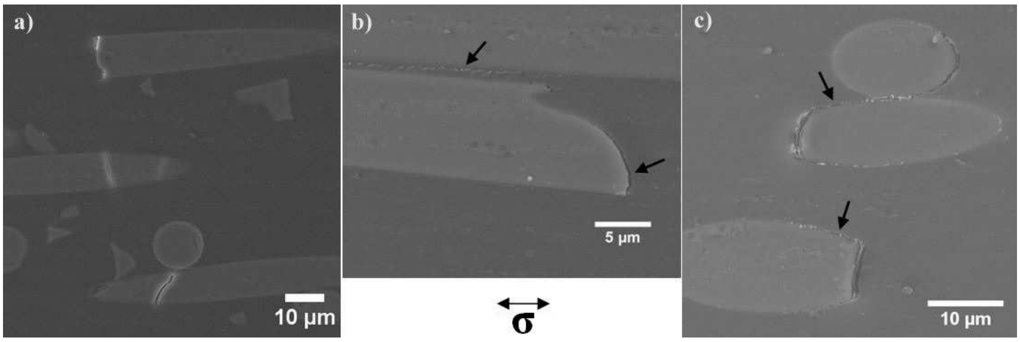

FIGURE 18: Echantillon sec de PA66/GF30, a) endommagement en tête de fibre et ruptures de fibres à 33% de σ_f, b) endommagement en tête de fibre et déformation plastique importante entre deux fibres adjacentes pour 48% de σ_f, c) propagation de l'endommagement le long de l'interface fibre/matrice à 85% de σ_f.

Les échantillons conditionnés à HR = 50% et 100% offrent de nombreuses décohésions interfaciales fibre/matrice, avec une déformation de la matrice localisée autour de ces zones de décohésion. La différence entre ces deux teneurs en eau réside dans un niveau d'endommagement plus faible pour l'échantillon à HR = 50% (Figs. 16b et 16c). Les microfissures matricielles se propagent préférentiellement de manière ductile dans les deux types d'échantillons. Des bandes de déformation matricielle sont également souvent présentes sur les échantillons conditionnés à HR = 100%, indiquant une grande déformation locale de la matrice (Figs. 19 and 16c). Cependant, leur occurrence n'est pas déterminante pour ceux conditionnés à HR = 50%. A noter qu'une forte teneur en eau provoque une forte plasticité, ce qui pourrait expliquer la présence d'une bande de déformation localisée dans l'échantillon conditionné à RH = 100%.

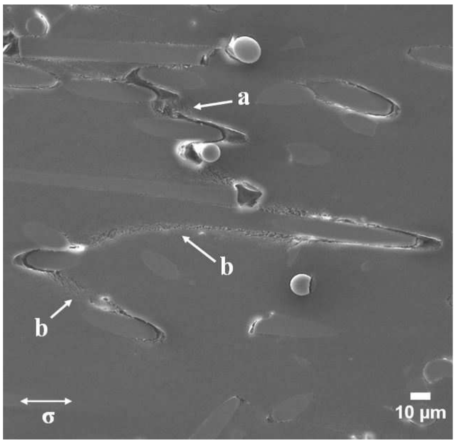

FIGURE 19: Echantillon de PA66/GF30 conditionné à HR = 100% à 98% de σ_f, a) microfissures matricielles et b) bandes de déformation matricielles.

Les résultats issus de μCT indique que les observations in-situ à la surface des échantillons correspondent de manière satisfaisante avec celles faites à l'intérieur des échantillons secs et humides (Figs. 20 et 21).

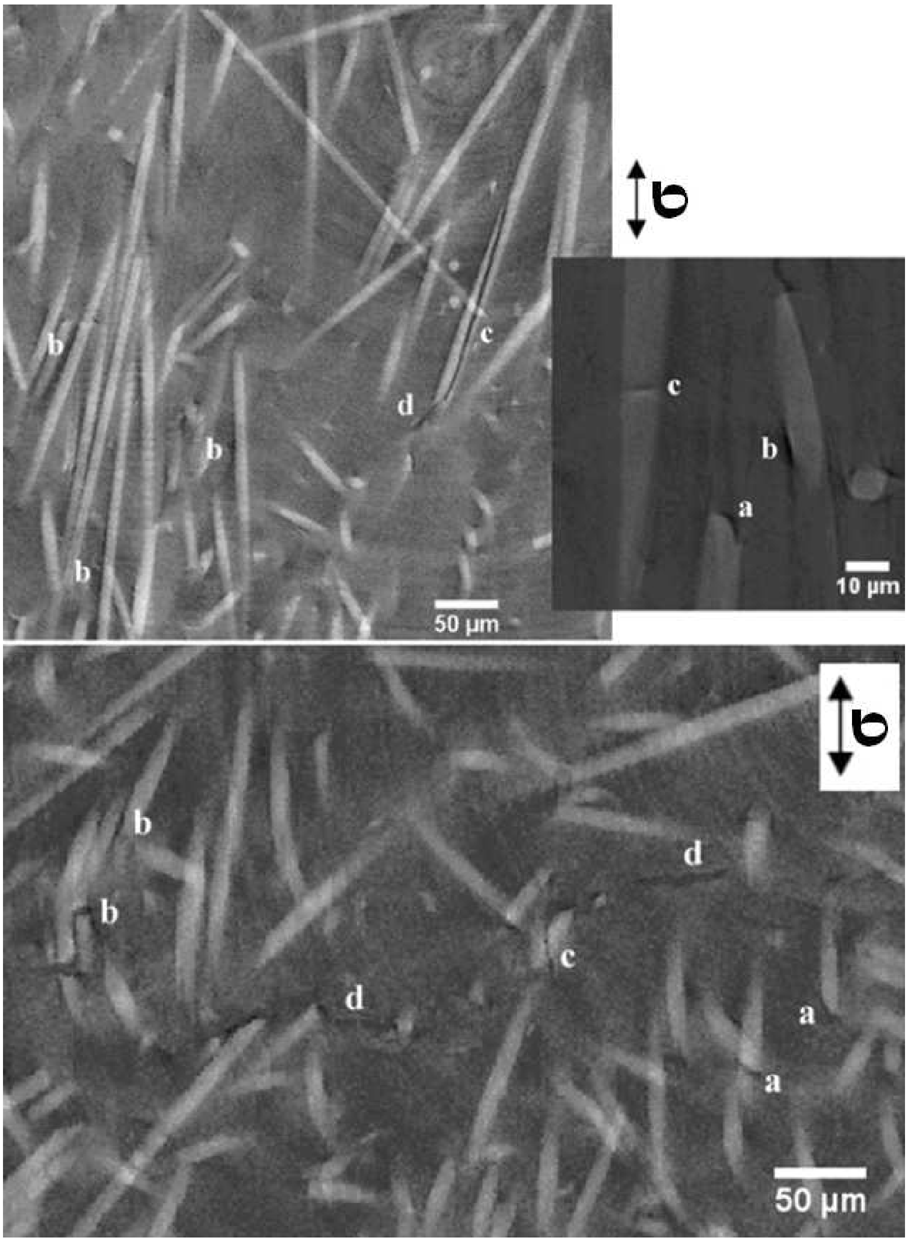

FIGURE 20: Mécanismes d'endommagement observées par μCT sur une éprouvette sèche de PA66/GF30 soumise à un essai de traction : a) décohésion de la matrice en tête de fibre, b) décohésion de l'interface fibre/matrice, c) ruptures de fibre et d) microfissures matricielles.

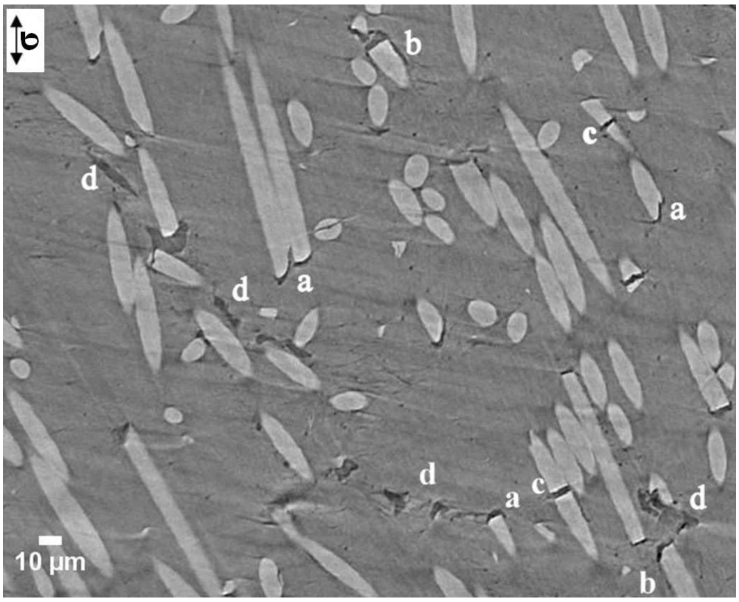

FIGURE 21: Mécanismes d'endommagement observés par μCT sur une éprouvette de PA66/GF30 conditionnée à HR = 50% et soumise à un essai de traction : a) décohésion de la matrice en tête de fibre, b) décohésion de l'interface fibre/matrice, c) ruptures de fibre et d) microfissures matricielles.

En se basant sur ces observations, une chronologie de l'endommagement tenant compte de l'humidité relative est proposée comme suit :

i. L'initiation de l'endommagement apparaît sous la forme de décohésion fibre/matrice aux extrémités de fibres et plus généralement là où les fibres sont proches les unes des autres, du fait d'une concentration de contrainte (pour les trois teneurs en eau étudiées). En ce qui concerne plus spécifiquement le matériau sec, l'initiation de l'endommagement peut également se manifester par quelques ruptures de fibres en plus du mécanisme précédent.

ii. Les décohésions interfaciales se propagent ensuite le long des interfaces fibre/matrice (pour toutes les humidités relatives étudiées), et vont de pair avec des zones localement déformées autour des fibres (pour RH = 50% et 100%). De nouvelles ruptures de fibres ont lieu dans le matériau sec

iii. A un niveau de contrainte élevée en flexion, des microfissures matricielles apparaissent et se propagent de manière fragile (pour RH = 0%) ou ductile (pour RH = 50% et 100%). Pour RH = 100%, ce phénomène s'accompagne de bandes de déformation matricielle.

iv. La propagation des microfissures matricielles provoque une accumulation de l'endommagement amenant à la ruine du matériau.

Caractérisation multiéchelles de l'endommagement en fatigue du PA66/GF30 sec

Lors de la fatigue du PA66/GF30, plusieurs phénomènes peuvent apparaître simultanément, comme des mécanismes d'endommagement ou du fluage cyclique couplée à une augmentation de la température. Tous ces processus peuvent contribuer à la résistance globale du matériau en fatigue. Une étude poussée de l'endommagement en fatigue est donc nécessairement une analyse couplée de tous les phénomènes concourants sous chargement cyclique.

Dans ce chapitre, l'accent est porté sur la caractérisation des mécanismes d'endommagement en fatigue du PA66/GF30 sec sous chargement uniaxial à amplitude constante. La combinaison des analyses du module dynamique, du fluage, de l'énergie dissipée et de l'évolution de la température, couplées à une observation post-mortem 3D microscopique de l'endommagement par μCT, permet de mieux comprendre les mécanismes d'endommagement associés.

Les essais de fatigue ont été réalisés sur des échantillons de PA66/GF30 secs (dry as molded), longitudinaux et transverses, à température ambiante. La consigne en contrainte consiste en un signal sinusoïdal d'amplitude constante avec un rapport de charge de 0.1 et une fréquence de 3Hz. L'acquisition continue de la température dans la zone utile de l'échantillon est réalisée par une caméra infrarouge CEDIP Jade III MWR. Les mécanismes d'endommagement et leur évolution ont été étudiés en utilisant des analyses par μCT réalisés sur des échantillons fatigués longitudinaux et transverses à plusieurs fractions de la durée de vie en fatigue. Pour cette étude, la μCT est configurée afin d'atteindre une résolution en voxel de 0.7 μm (pour les échantillons longitudinaux) et de 1.4 μm (pour ceux transverses). La dimension des échantillons ainsi étudiés est de $2 \times 2 \times 3.2$ mm^3, où 3.2 mm correspondent à l'épaisseur. Une étude par μCT sur des échantillons vierges a également été menée afin de servir de référence à l'analyse de l'endommagement sur ceux fatigués.

Evaluation de l'endommagement macroscopique Sous chargement en fatigue, la dissipation de l'énergie peut être associée à différents phénomènes tels que le développement de l'endommagement ou la dissipation intrinsèque au comportement visqueux. Une partie de l'énergie mécanique de déformation due à ces deux mécanismes est transformée en chaleur. Ainsi, un couplage thermo-viscoélastique endommageable est à envisager lors d'un chargement en fatigue. L'évolution du module dynamique peut être utilisée en tant qu'indicateur de l'endommagement selon une théorie continue de l'endommagement [Nouri 2009a, Ladeveze 1992]. Pour tous les chargements envisagés dans cette étude, le module dynamique normalisé est stable sur les 1000 premiers cycles et diminue ensuite à un taux dépendant du niveau de chargement (Fig. 22).

L'évolution de la température moyenne met en exergue deux régimes. Le premier correspond à un module normalisé stable, où la dissipation de chaleur semble être majoritairement liée à la dissipation d'énergie intrinsèque à la nature visqueuse du composite. Le second est associé à la chute du module dynamique normalisé et correspond à un point d'inflexion de l'évolution de la température moyenne. Ce changement de régime peut être associé au fait que l'énergie de déformation ne se dissipe pas seulement du fait de la nature visqueuse du matériau, mais aussi du fait de l'endommagement.

La déformation maximum augmente continuellement durant la fatigue. Il en va de même pour son minimum, de telle manière que l'amplitude de déformation est presque constante pendant la durée de vie en fatigue. Il en ressort que l'endommagement observé est associé à un couplage entre le fluage et le chargement cyclique. Cependant, étant donné que l'évolution de la déformation moyenne reste raisonnable pour la plupart des essais de fatigue ($< 1\%$), et que la diminution du module dynamique n'est pas lié à un changement de l'évolution de la déformation moyenne qui pourrait indiquer une accélération de l'endommagement en fluage, il est admis que la majorité de l'endommagement observé est relié à la composante cyclique du chargement et que l'endommagement en fluage est limité pour ces échantillons secs. La situation est différente pour les échantillons transverses sous chargement maximal en contraintes. Un adoucissement thermique a alors lieu, comme montré par l'augmentation significative de la déformation maximale à la fin de la durée de vie en fatigue.

Ainsi, il peut être affirmé que la diminution du module dynamique est profondément liée à l'évolution de l'endommagement, sauf dans le cas des plus hauts niveaux de chargement d'échantillons transverses ($\sigma_{max} = 70\% \ \sigma_u$), où un adoucissement thermique peut alors avoir lieu et mènerait à la rupture. L'évolution du module dynamique est importante malgré le fait qu'il soit difficile d'appréhender complètement le comportement endommageable en fatigue sans s'intéresser aux évolutions de la déformation, de la température et de l'énergie dissipée.

Evaluation de l'endommagement à l'échelle microscopique La technique de μCT est utilisée pour étudier l'endommagement en fatigue à l'échelle microscopique. L'endommagement est quasiment inexistant sur les échantillons vierges. Sur les échantillons fatigués, une décohésion interfaciales fibre/matrix est fréquemment observée, comme montré sur la Fig. 23. Quelques ruptures de fibres sont également observées mais il semble que ce mécanisme d'endommagement ne soit pas dominant. Dans certains cas, des microfissures de la matrice peuvent apparaitre, comme celles observées au cœur des échantillons transverses (Fig. 24). Le cœur, relativement mince, est supposé supporter un niveau de contraintes plus élevée du fait de son orientation longitudinale par rapport à la direction de chargement. Les microfissures matricielles se développent et coalescent plus rapidement dans cette région, préférentiellement transversalement à la direction de chargement ou à la direction locale des fibres.

Afin de proposer une première quantification de l'endommagement et ainsi construire une analyse plus consistante des mécanismes d'endommagement du PA66/GF30, le facteur de forme des vides a été analysé en fonction de leur orientation. Pour établir une com-

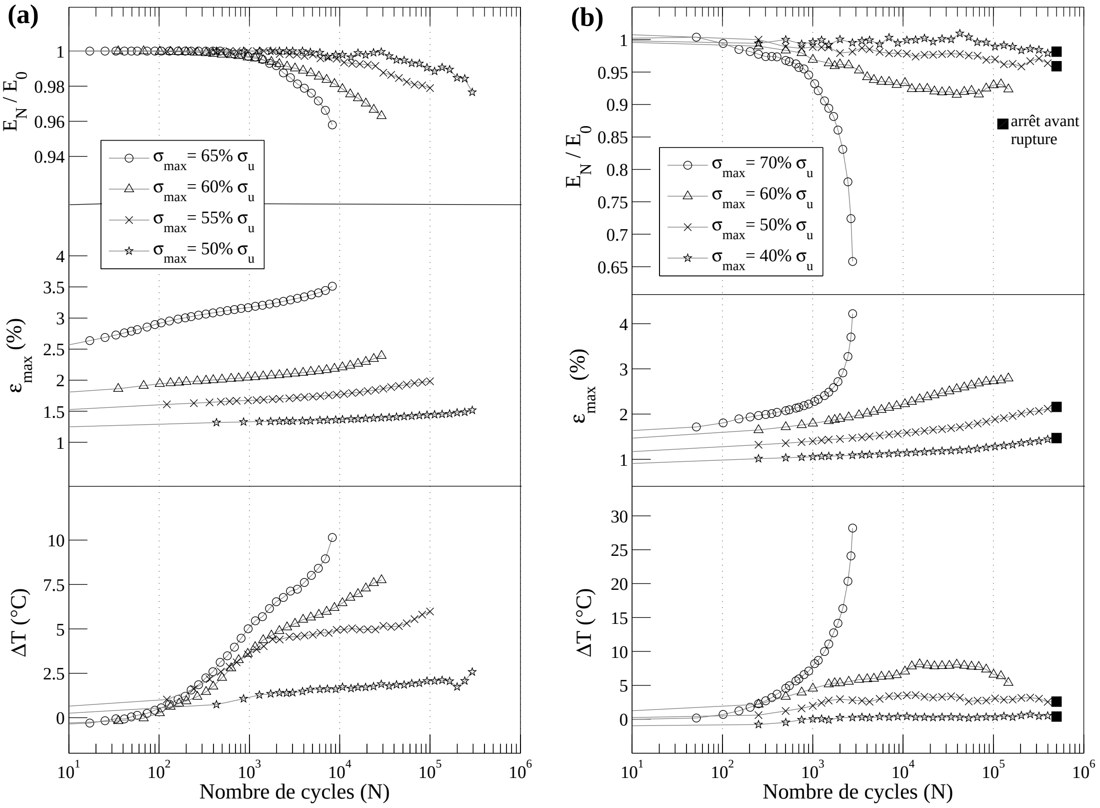

FIGURE 22: Evolution du module dynamique normalisé (E_N/E_0), de la déformation maximale (ε_{max}) et de la température moyenne des échantillons (ΔT) longitudinaux (a) et transversaux (b) de PA66/GF30 pendant un essai de fatigue. (σ_u représente la charge limite de rupture relative à l'orientation associée)

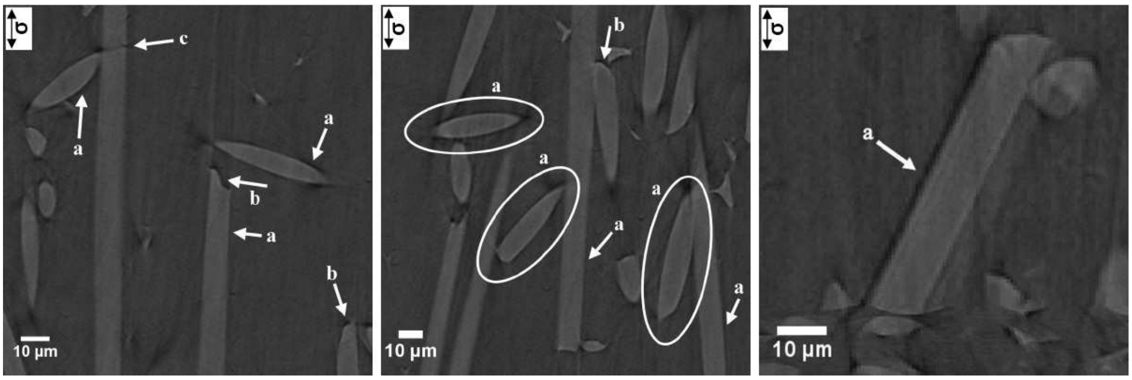

FIGURE 23: Mécanismes d'endommagement observées en peau sur une éprouvette longitudinale fatiguée jusqu'à rupture pour une contrainte maximale égale à 60% σ_u ; a) décohésion interfaciales fibre/matrice, b) vides aux extrémités de fibres, et c) rupture de fibres.

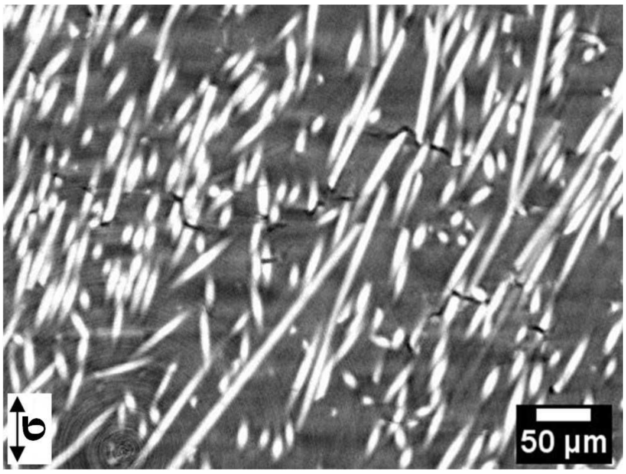

FIGURE 24: Microfissures matricielles observées à coeur sur une éprouvette transverse fatiguée jusqu'à la rupture avec une contrainte maximale égale à 60% σ_u.

paraison pertinente entre les caractéristiques de l'endommagement au niveau du cœur et de la peau, cette évaluation est réalisée dans un volume de 50 μm issu de l'échantillon de μCT, soit en cœur soit en peau (Fig. 25). Pour les échantillons vierges, les vides observés en peau présentent un facteur de forme faible. Ceux-ci pourraient être dus d'une part à l'endommagement initial, et d'autre part à l'artéfact inhérent à la méthode d'identification par fluctuation des niveaux de gris avec utilisation de seuil. Il est à remarquer que cette technique de seuil est définie et optimisée à partir de l'observation des vides sue des échantillons obtenus après essais de fatigue. Le seuil ainsi déterminé est unique et alors appliqué à tous les échantillons, ceux vierges compris. En utilisant cette méthode, toute déviation du facteur de forme ou du volume des vides des échantillons fatigués ne peut pas être imputée à la méthode de seuillage mais est majoritairement liée au développement de l'endommagement.

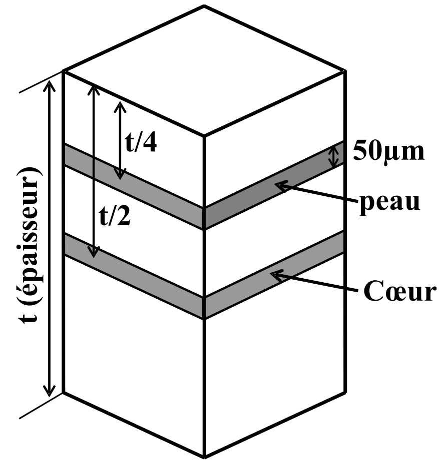

FIGURE 25: Schéma des volumes analysés par μCT en cœur et en peau du composite.

Figs. 27 et 28 illustrent le point précédent sur les échantillons longitudinaux et transversaux, respectivement. Ces derniers ont subi un essai de fatigue jusqu'à rupture à un niveau de contrainte maximum de 60% σ_u. Un endommagement significatif est observé par rapport à l'état du matériau vierge (Fig. 26). Sur les échantillons longitudinaux, les vides à cœur et en peau sont respectivement orientés majoritairement à 0^o et 90^o (Fig. 27). Il est important de noter que ces orientation sont les mêmes que celles des fibres en cœur et en peau. Ainsi, les vides sont principalement situés le long des fibres sous la forme de décohésion interfaciales. En ce qui concerne les échantillons transverses, les vides en cœur et en peau sont tous orientés à 90^o, comme montré sur la Fig. 28. Cela montre qu'en peau a lieu une décohésion interfaciale, mais qu'à cœur, des microfissures matricielles se développent transversalement à la direction de chargement ou à la direction des fibres. En surface des échantillons où l'orientation est aléatoire, le comportement est le même qu'en peau, que ce soit pour les échantillons longitudinaux ou transverses. Les fibres de cette couche ne possèdent pas un degré d'orientation aléatoire élevé et elles tendent à s'orienter suivant la direction de l'écoulement, qui est celle des fibres en peau.

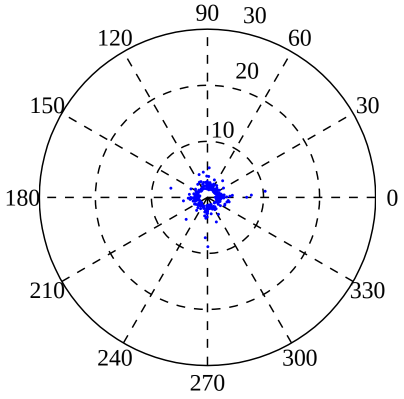

FIGURE 26: Graphe représentant le facteur de forme des vides en fonction de leur angle d'orientation, dans la couche de peau d'un échantillon vierge.

En plus de l'étude de l'endommagement lors de la rupture, des analyses similaires par μCT ont été réalisées sur des échantillons longitudinaux fatigués à différents pourcents de leur durée de vie en fatigue. La Fig. 29 illustre l'évolution du volume de vide en peau en fonction de leur orientation et du nombre de cycles. Cette analyse montre clairement que le volume de vide augmente pendant l'essai de fatigue. Il est important de noter que des vides de faible volume sont également observés sur les échantillons vierges, du fait d'un endommagement initial ou de la fluctuation du niveau de gris. La majorité des vides les plus grands en peau sont orientés à 0^o et ont une orientation parallèle à celle des fibres, qui est également celle de la direction de chargement. Cela signifie que les vides, notamment ceux au volume plus important, sont situés le long des interfaces fibres/matrice et constituent donc une décohésion interfaciale. Ces résultats sont cohérents avec l'ana-

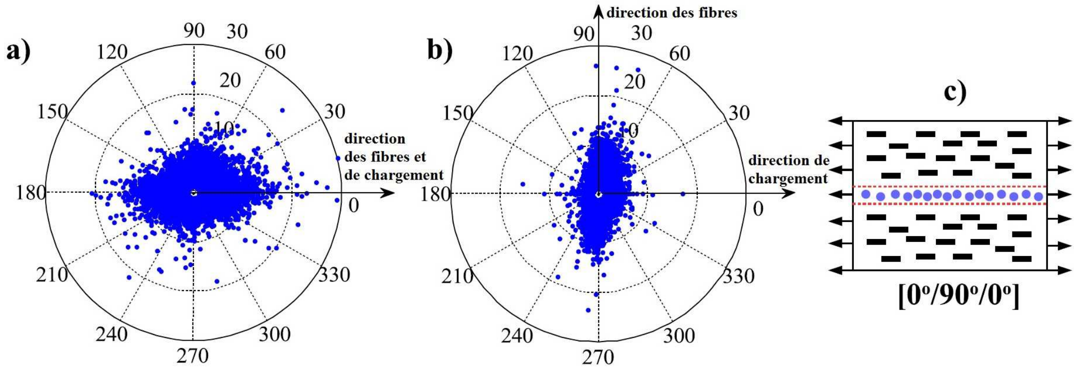

FIGURE 27: Graphe représentant le facteur de forme des vides en fonction de leur angle d'orientation, dans la couche a) de peau et b) à cœur d'une éprouvette longitudinale fatiguée. L'analogie avec une éprouvette longitudinale stratifiée est présentée en c) et constitue une ligne directrice pour l'interprétation des valeurs des angles d'orientation des vides.

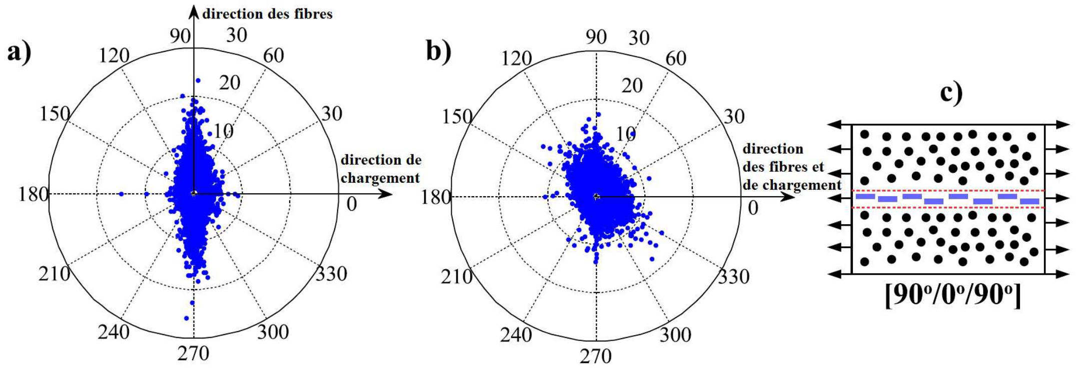

FIGURE 28: Graphe représentant le facteur de forme des vides en fonction de leur angle d'orientation, dans la couche a) de peau et b) à cœur d'une éprouvette transverse fatiguée. L'analogie avec une éprouvette transverse stratifiée est présentée en c) et constitue une ligne directrice pour l'interprétation des valeurs des angles d'orientation des vides.

lyse des facteurs de forme réalisée précédemment. L'endommagement n'augmente que relativement peu de 0% à 50%. Cependant, il évolue plus significativement dans la seconde moitié de la durée de vie en fatigue. Il est important de noter que ce changement correspond à l'évolution du module dynamique donné sur la Fig. 22. Si l'on considère le changement du volume total de vide ΔV relativement à son volume initial, on peut obtenir que $\Delta V_{50\%N_f} < 0.5\%$, $\Delta V_{75\%N_f} = 1.3\%$ et $\Delta V_{100\%N_f} = 2.5\%$. Cette évolution est cohérente avec celle du module dynamique en fin de vie. Les analyses par μCT n'ont néanmoins pas été capables de capturer l'évolution de l'endommagement au début de la vie en fatigue. Cela est probablement dû au fait que l'ouverture des interfaces se situe au-delà de la limite de résolution des analyses par μCT.

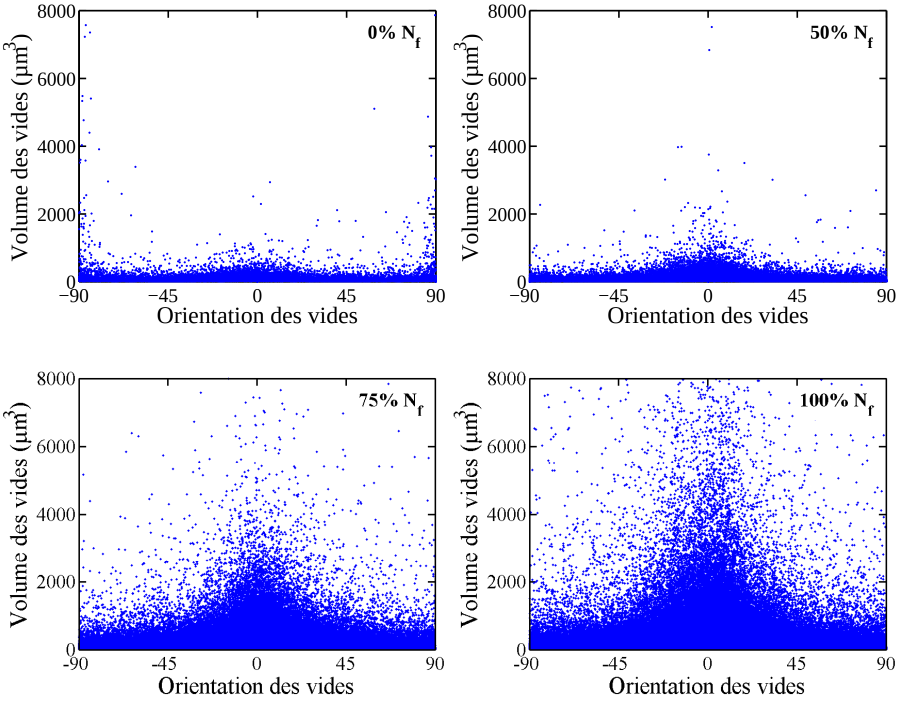

FIGURE 29: Graphe représentant l'orientation des vides en fonction de leur volume, au niveau de la peau d'une éprouvette longitudinale fatiguée jusqu'à plusieurs pourcents de sa durée de vie en fatigue (N_f) avec une contrainte maximale égale à 60% σ_u.

Conclusions générales et perspectives

Le présent travail de thèse s'appuie sur une approche expérimentale étendue afin d'identifier les mécanismes d'endommagement du PA66/GF30 en chargement monotone et en fatigue. Préalablement à une étude approfondie de l'endommagement, le comportement général du matériau et sa microstructure ont été étudiés.

Il en résulte que le PA66/GF30 a un comportement anisotrope du fait de sa microstructure cœur-peau-surface le long de son épaisseur. De plus, les propriétés mécaniques du PA66/GF30 sont particulièrement dépendantes de la vitesse de déformation, de la température et de l'humidité relative (HR). La matrice en polyamide-66 et le PA66/GF30 ont également un comportement très visqueux. Pendant un test de traction ou un essai en fatigue, ce comportement visqueux se couple à l'endommagement. Il a néanmoins été difficile de séparer leur contribution respective, malgré les techniques de changement de volume et de thermographie utilisées ou encore les tests de traction avec décharges complètes. Des essais en traction avec décharges partielles ont tout de même donné des résultats fiables sur le niveau d'endommagement, du fait que les effets visqueux sont intrinsèquement atténués par ces tests. Cependant, la réalite de l'endommagement dans le matériau reste inaccessible par ces essais.

Une étude in-situ au MEB du PA66/GF30 en chargement monotone a été réalisée afin d'appréhender l'endommagement réel du PA66/GF30. Des échantillons avec différentes teneurs en eau ont été étudiés. Les résultats expérimentaux montrent que l'endommagement est développé à l'intérieur du matériau. L'humidité relative influence grandement les mécanismes d'endommagement, à la fois quantitativement et qualitativement. L'endommagement des échantillons secs s'initie pour des chargements significativement plus élevés que celui des échantillons dont l'humidité relative est de 50% ou 100%. L'endommagement augmente également avec le taux d'humidité.

Il a été conclu que pour les échantillons secs, les mécanismes d'endommagement prédominants sont la décohésion interfaciale fibre/matrice, les ruptures de fibres et la propagation fragile de fissures matricielles. Les échantillons à HR = 50% et HR = 100% manifestent quasiment les mêmes mécanismes d'endommagement prédominants, à savoir la décohésion interfaciale fibre/matrice accompagnée de bandes locales de déformations matricielles, ainsi que des microfissures matricielles ductiles. Le niveau d'endommagement diffère selon la teneur en eau. Les bandes de déformation matricielles sont plus fréquemment observées chez les échantillons conditionnés à HR = 100% que ceux à HR = 50%. Les résultats issus de la μCT étendent la validité de ces observations en surface au volume des matériaux secs et humides.

En se basant sur ces observations, des chronologies d'endommagement ont été établies. Celui-ci s'initie en pointe de fibre ou plus généralement là où les fibres sont proches les unes des autres. Ces décohésions se propagent ensuite le long des interfaces fibre/matrice. A un niveau de contrainte relative en flexion élevé, des microfissures matricielles peuvent apparaître et se propager, menant à la ruine du matériau. En plus des mécanismes précédents, l'endommagement peut également s'initier par rupture de fibres (notamment à HR

= 0%). En raison de la bonne ductilité de la matrice humide, les décohésions interfaciales chez les échantillons conditionnés à HR = 50 % et 100% s'accompagnent localement de zones de déformation matricielle autour des fibres. De plus, les microfissures matricielles à HR = 0% ont tendances à se propager de manière fragile, contrairement à celles à HR = 50% et 100% qui se propagent de manière ductile, avec des bandes de déformations matricielles à HR = 100%.

L'étude a été étendue à l'endommagement en fatigue du PA66/GF30 sec, à la fois au niveau macroscopique et microscopique. Il est ainsi montré que les résultats expérimentaux relatifs à l'évolution du module dynamique, de la déformation, de la température et de l'énergie dissipée sont importants afin d'évaluer l'évolution de l'endommagement. Le module dynamique peut être utilisé en tant qu'indicateur de l'endommagement, bien qu'il puisse exagérer les prévisions d'endommagement pour des contraintes élevées, du fait de la viscosité du matériau composite.

Une analyse thermographique de la surface du PA66/GF30 révèle que l'endommagement est diffus dans l'intégralité de l'échantillon. Cependant, les observations microscopiques par μCT montrent que l'endommagement est certes diffus mais que son niveau n'est pas le même selon les emplacements à l'intérieur de l'échantillon.

L'analyse par μCT établit que l'endommagement est principalement développé le long de l'interface fibre/matrice, sauf dans la couche à cœur des échantillons transverses où dominent des microfissures matricielles orientées préférentiellement transversalement à la direction de chargement, du fait de la concentration locale de contraintes.

Les résultats issus de μCT montrent également que l'endommagement augmente continuellement durant la fatigue. Cette évolution est plus marquée pendant la seconde moitié de la durée de vie en fatigue. Malgré la haute résolution utilisée dans le cadre de ces travaux, la détection des décohésions interfaciales fibre/matrice s'est avérée ardue au début de la durée de vie en fatigue. Une meilleure résolution pourrait offrir une analyse plus poussée de cette première étape en fatigue.

En conclusion des résultats ainsi présentés, les chargements monotones et en fatigue manifestent les même mécanismes d'endommagement, dont principalement la décohésion interfaciale. Quelques ruptures de fibres sont également à noter dans les deux cas bien que ce mécanisme ne soit pas prépondérant dans le comportement mécanique du composite. En outre, pour une contrainte élevée, des microfissures matricielles ont été observées dans les deux cas de chargements, avec une orientation préférentielle perpendiculaire à la direction de chargement.

Etant donné que pour les mécanismes d'endommagement en chargement monotone et en fatigue sont identiques pour les échantillons secs, une extrapolation à ceux humides est proposée. Ceci est confirmé par les travaux encore non référencés d'H. Rolland, doctorante dans le cadre du projet DURAFIP. Elle montre ainsi que les scénarios d'endommagement sont similaires en fatigue et en chargement monotone, et ce quelle que soit la teneur en eau.

Les résultats de ces travaux sur l'aspect physique de l'endommagement, ainsi que ceux à venir de la thèse en cours d'H. Rolland (à propos de l'endommagement en fatigue du PA66/GF30 humide sous chargements d'amplitude constante et variable), sont actuellement implémentées dans un modèle micromécanique prédictif incluant la modélisation en fatigue. Cet aspect est pris en charge par N. Despringre, doctorant dans le cadre du projet DURAFIP.

Le modèle micromécanique actuel [Desrumaux 2000, Jendli 2009] va être étendu afin de prendre en compte l'évolution de l'endommagement, dont la cinétique de décohésion interfaciale couplée à la rhéologie visqueuse de la matrice en polyamide, le tout en accord avec la microstructure du PA66/GF30. Une attention particulière est accordée à l'influence de la teneur en eau sur les propriétés mécaniques de la matrice ainsi que sur les caractéristiques de l'interface, afin de prédire au mieux l'apparition et le développement de l'endommagement dans le PA66/GF30.

Part II

Damage mechanisms in short glass fiber reinforced polyamide-66

CHAPTER 1

General introduction

Contents

1.1 Industrial context

Fiber reinforced plastic composites (FRP) gain ever increasing attention in the automotive industry. Progressively, parts made of metals such as steel and aluminum are replaced by FRPs. Previously, FRPs were only used for components bearing small loads such as bumpers or dashboards. Nowadays, it has also been used for the components carrying high static or cyclic loadings such as parts near the engine.

There are two major drivers for the use of FRPs; cost and weight savings. In terms of cost, FRPs have long been considered in high priority in material selection processes since their molding technologies are able to fabricate parts with complex geometries. This allows integration of many functions into one piece, resulting in parts savings. Consequently, it will reduce the manufacturing and assembly times and costs.

Weight reduction is also possible due to the low density of the composites, while the strength and modulus are still comparable to those of metals due to the high specific strength and modulus of the composites. The reason for weight reduction is related to the environmental concern. Reducing vehicle weight improves fuel efficiency and thus reducing the environmental burden of the automotive. This is also triggered by the strict legislation to limit CO_2 emission for the new car sales. For example, the European Union (EU) has a stringent target for the average new passenger cars to emit less than 130 and 95 grams of carbon dioxide per kilometer (g CO_2/km) by 2015 and 2020, respectively. So far, all car manufacturers in EU are on track to meet the 2015 and 2020 targets since their average CO_2 emission decreases constantly, as shown in Fig. 1.1. However, if one considers the emission level data of individual car manufacturers in EU, it can be seen that only three carmakers, i.e. Fiat, Toyota and Peugeot-Citroen that have fulfilled the 2015 target, as shown in Fig. 1.2. The rest of manufacturers still need significant efforts to meet the targets to avoid EU fines.

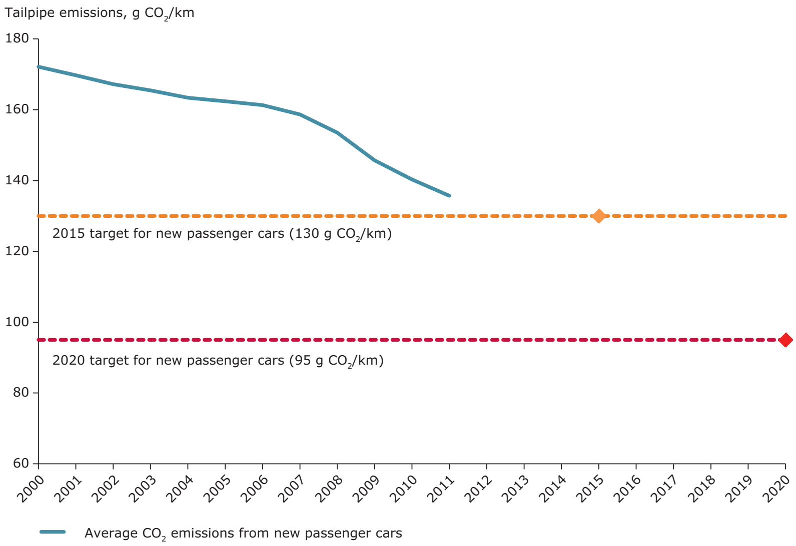

FIGURE 1.1: The progress of average CO_2 emission for new cars versus 2015 and 2020 targets [European Environment Agency 2012].

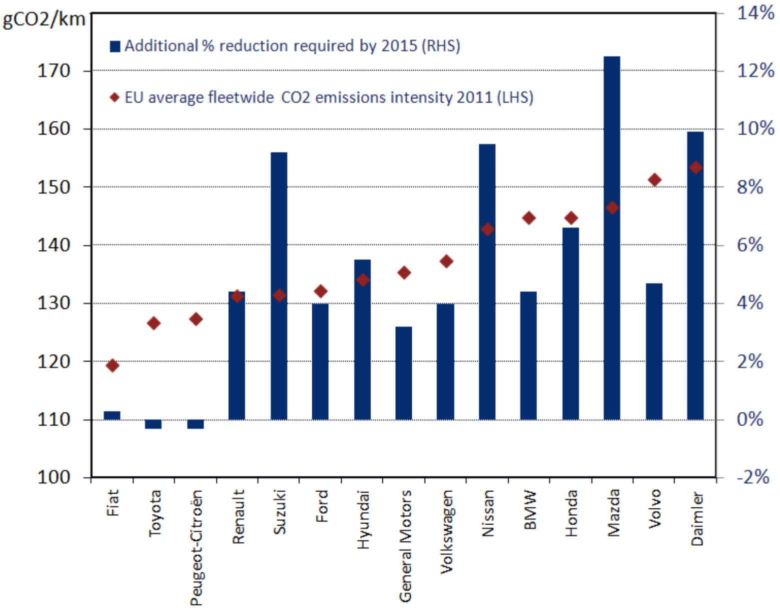

FIGURE 1.2: EU vehicle emission intensity by 2011 and required improvement to meet the 2015 emission target of EU main car manufacturers [European Environment Agency 2012, MSCI 2013].

The material of interest in this work is the injection molded short glass fiber reinforced polyamide-66 composite. Polyamide matrix composites are one of the most valuable materials in engineering plastics, particularly for applications requiring high mechanical properties along with chemical and temperature resistance, in addition to the excellent finish. These composites are often the perfect answer for structural designers seeking weight savings, function integration and design freedom.

The advanced extrusion compounding techniques and injection molding technologies to produce structural parts with complex geometry in short glass fiber-reinforced polyamides exhibit great potential in terms of lower cost and weight saving. Due to its well-balanced performance, the use of polyamide matrix composites in automotive have grown consistently over the past 20 years and have allowed to replace metals or thermoset matrix composites in many automotive components. Some examples of automotive parts made of short glass fiber reinforced polyamide-66 composites can be seen in Fig. 1.3.

1.2 Thesis scope and objectives

The current work is under the context of DURAFIP, FUI-DGCIS project. The project is led by Solvay Engineering Plastics and it assembles 14 partners consist in a well balanced of members from both industry and academia. The final goal of this project is to achieve a multiscale computation towards high cycle fatigue modeling in order to reach predictive design of reinforced thermoplastic components, particularly parts made of short glass fiber reinforced polyamide-66. A reliable component design towards fatigue loading is important as many automotive parts are subjected to repeated loading combined with temperature variation, such as parts near the engine which experience engine vibration and structural components that support the vibrations of the chassis. Such multiscale fatigue modeling requires a large experimental campaign that encompasses the characterization of both the composites behavior and the interactions between their phases or constituents. It is worth noting that the properties of the injection molded short glass fiber reinforced polyamides depend on several aspects such as fiber orientation, viscoelastic-viscoplastic behavior of the polyamide matrix, damage initiation and propagation behavior, loading rate and environmental conditions (i.e. temperature and relative humidity).

The current work is considered as the first phase of the DURAFIP project undertaken by the research group of Arts et Métiers ParisTech. The work focuses on extensive experimental approaches to identify fatigue damage behavior of injection molded 30 wt% short glass fiber reinforced polyamide-66 (PA66/GF30), considering various effects such as relative humidity and injection process induced microstructure. The damage mechanisms under quasi-static monotonic loading of PA66/GF30 is also studied in order to build a strong understanding on the damage behavior of PA66/GF30. In this work, several experimental techniques are employed to study the damage behavior of PA66/GF30, i.e. by exploiting the data extracting from mechanical tests, thermography and X-Ray micro-computed tomography (μCT).

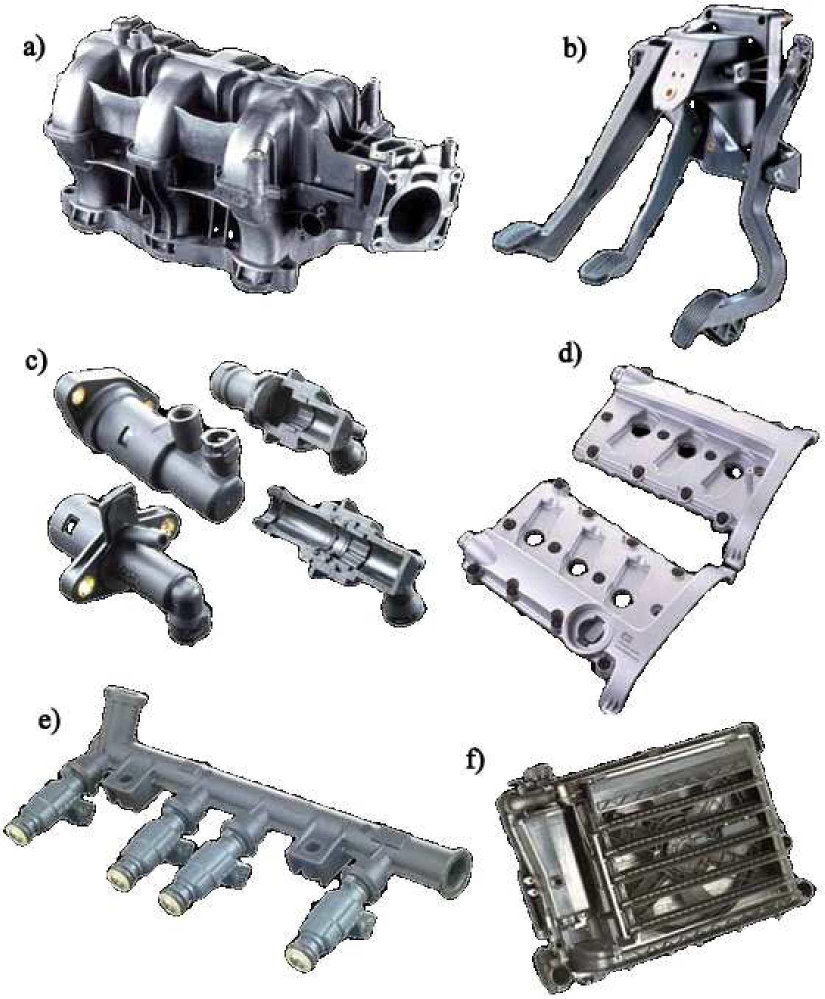

FIGURE 1.3: Example of automotive components made of short glass fiber reinforced polyamide-66 composites : a) air intake manifold, b) pedals and pedal box, c) clutch master cylinder d) cylinder head cover, e) fuel rail, and f) cooling module [Solvay Engineering Plastics 2009].

The current experimental findings on the physical aspect of damage, together with the prospective results of the ongoing work by H. Rolland (PhD student) which focuses on the fatigue damage behavior of humid PA66/GF30 under constant and variable amplitude loading conditions, will be implemented into a predictive micromechanical model towards fatigue loading. The modeling task is currently undertaken by N. Despringre (PhD student). The developed model should consider the fiber/matrix interface damage kinetic coupled with the viscous rheology of the polyamide matrix in relation with the PA66/GF30 microstructure.

1.3 Organization of manuscript

The current work is organized as follows:

In Chapter 2, the material used for the current work, the injection molded 30 wt% short glass fiber reinforced polyamide-66 (PA66/GF30) is introduced. The characteristics, advantages and limitations of this material are discussed. Qualitative and quantitative investigation on PA66/GF30 microstructure are discussed. To consider the anisotropy effect of PA66/GF30, the locations of specimen's extraction for mechanical and damage characterizations in this work are detailed.

The mechanical behavior and properties, as well as the general idea on damage behavior of PA66/GF30 are then studied in Chapter 3. The study covers the effect of process induced anisotropy, strain rate, temperature and relative humidity conditions on the tensile properties of PA66/GF30. The fatigue properties of dry PA66/GF30 are also studied by analyzing the *S–N* curves, fatigue strain rate and anisotropy effect. Particular attention is given to the contribution of viscous effect and damage on the tensile and fatigue behavior of PA66/GF30.

Afterwards, in Chapter 4, damage mechanisms of PA66/GF30 are analyzed using in situ SEM mechanical tests on specimens conditioned under three relative humidity contents (RH = 0%, 50% and 100%). The validity of these in situ analyses are confirmed by X-ray micro-computed tomography (μCT).

Subsequently, The damage behavior of injection molded 30 wt% short glass fiber reinforced polyamide-66 composite PA66/GF30 under fatigue loading is studied in Chapter 5. The evolution of dynamic modulus, hysteresis area, cyclic creep and temperature during fatigue tests are analyzed and discussed. Fatigue damage analyses by μCT technique on interrupted fatigue tests at several percentages of total fatigue life are performed to further understand the damage mechanisms and evolution during fatigue loading.

Finally, the current work is summarized by discussion on general conclusions and further works. The conclusion emphasizes notably about discussion on overall damage mechanisms in PA66/GF30 in terms of its initiation and chronology. In the further work, the idea on extending the current experimental findings towards a multiscale micromechanics modeling are overviewed.

CHAPTER 2

Material and process induced microstructure description

Contents

In this chapter, the material employed in the current work, the injection molded 30 wt% short glass fiber reinforced polyamide-66 (PA66/GF30) is introduced. The characteristics, advantages and limitations of this material are discussed. Brief review on processing of short glass fiber reinforced composites and its effect on the microstructure are then presented, followed by the brief theoretical explanation on quantitative description of fiber orientation. Afterwards, qualitative and quantitative investigation on PA66/GF30 microstructure are discussed. Finally, to consider the anisotropy effect of PA66/GF30, the locations of specimen's extraction for mechanical characterizations in this work are detailed.

2.1 Material

The material studied in this work is the PA66/GF30. Considering the role of its constituents, the polyamide-66 represents as the matrix and the short glass fiber as the reinforcing element. The properties of individual components are crucial to determine the final properties of the composites. Therefore, general properties and characteristics of both constituents will be discussed in order to acquire a good comprehension on the overall behavior on the studied material.

2.1.1 Glass fibers

Glass fibers are the most widely used reinforcement agent for composite materials, despite the presence of higher performance and higher cost fibers, i.e. carbon and aramid fibers. The glass-fiber reinforced plastic markets are predominately based on E-type glass fiber. The major advantages of glass fiber reinforced system are: good corrosion resistance, lightweight, good toughness, very good electrical insulation properties, high absolute and specific strength, high process freedom and ability to manufacture a wide range of shapes [Sims 2000]. The main properties of E-glass fiber typically used in short fiber reinforced polymers are shown in Table 2.1.

Short glass fibers are produced by chopping or cutting continuous glass fiber strands or rovings. The fiber aspect ratio (fiber length to diameter ratio) after the cutting process is estimated to be between 10 and 100. The shorter chopped strands are used for injection molding compounds, whereas the longer chopped strands are used for compression molding compounds [Mallick 2000].

	E-glass fiber
Filament diameter (μm)	10
Density (g cm^{-3})	2.54
Tensile modulus (GPa)	72.4
Tensile strength (MPa)	1725[a]
Poisson ratio	0.22
Coefficient of thermal expansion (10^{-6} °C^{-1})	5
Thermal conductivity (W/m.°C)	1.04
Electrical resistivity (ohm.cm)	0.1

[a] Virgin E-glass fiber strength is 3450 MPa.

Table 2.1: Typical properties of E-glass fiber applied in short fiber reinforced polymers [Mallick 2000, Dwight 2000].

2.1.2 Polyamide matrix

While the reinforcing fibers play an important role in determining the stiffness and strength of the composite, the ability of the matrix to support the fibers and transfer the applied stress to them is also crucial. Polyamides are ones of the commonly used thermoplastics as the matrix materials. Polyamides, or nylons are characterized by the presence of amide linkages (–CONH–) on the polymer main chain. The commercial use of polyamides is centered into two main products: polyamide-66 and polyamide-6. In addition to the two aforementioned polyamides, polyamide-68, polyamide-610, polyamide-612, polyamide-11, polyamide-12 and polyamide-46 are also available commercially. The numerals in the names refer to the number of carbon atoms in the monomer(s). The principal structural difference between the various types of polyamide is in the length of aliphatic chain segments (the $-(CH_2)_n-$ segments) separating the adjacent amide groups. The molecular structures of polyamide-66, the matrix material used in this study, is shown in Figure 2.1.

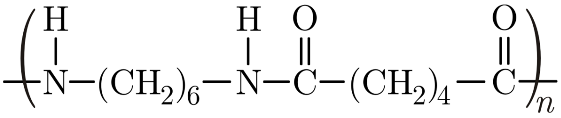

$$\left(\overset{H}{\overset{|}{N}}-(CH_2)_6-\overset{H}{\overset{|}{N}}-\overset{O}{\overset{\|}{C}}-(CH_2)_4-\overset{O}{\overset{\|}{C}}\right)_n$$

FIGURE 2.1: The molecular repeat unit of polyamide-66.

Polyamide is a semicrystalline polymer. When a molten polyamide solidifies, the crystals grow from individual nuclei and radiate out to form spherulites, as illustrated in Fig. 2.2. These spherulites exhibit a characteristic diameter from 1 to 500 μm, depending on the chemical nature of the polymer, concentration of the nucleation sites and processing parameters. Inside the spherulite, a two-phase system consisting of amorphous and crystalline regions is developed (Fig. 2.3). The crystalline zone is presented by the lamellar crystals and the amorphous portion is the one outside the lamellar crystals.

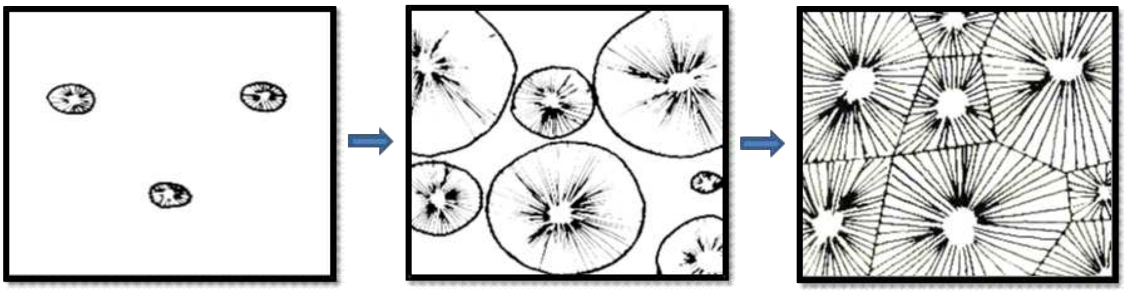

FIGURE 2.2: Growth of spherulites during solidifying process of a molten polymer.

Polyamide-66 is widely used because it offers a good balance between price and properties (mechanical, physical, chemical, etc.). The polar amide groups give rise to high interchain attraction in the crystalline zones, and the aliphatic segments control the chain flexibility in the amorphous zones. This combination of properties yields polymers which are tough above their glass transition temperatures. The high intermolecular

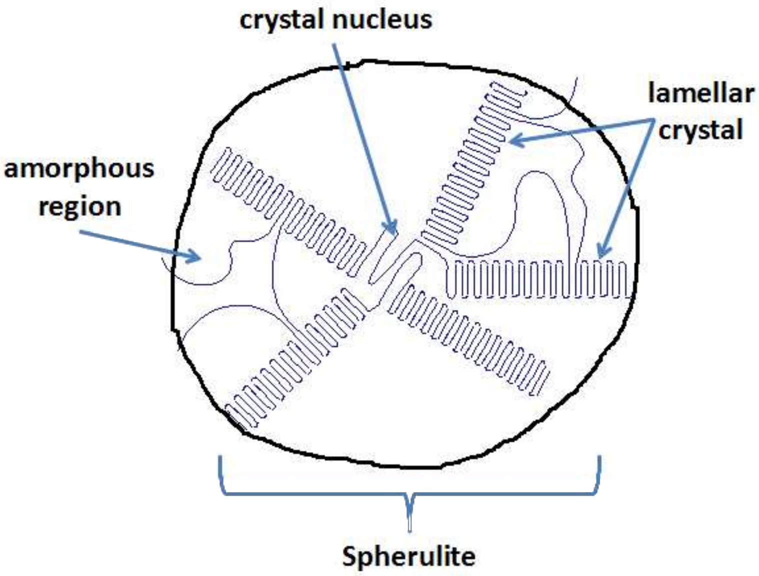

FIGURE 2.3: Semicrystalline polymer structure.

attraction also accounts for high melting points of polyamides. Because of the high cohesive energy and their crystalline state, the polyamides are resistant to most solvents. Shortly, polyamide-66 is a superior thermoplastic material as it exhibits high stiffness with good resistance to abrasion, fatigue and impact, as well as excellent performance when exposed to elevated temperatures. The main properties of polyamide-66 can be seen in Table 2.2.

However, it is worth noting that the mechanical properties of the polyamide is significantly influenced by the amount of crystallization in the test piece. Therefore, proper process conditioning is crucial to acquire an optimum mechanical properties. For example, in a molding process of polyamide, slowly cooled molten polyamide would result in a higher crystallinity level compared to the fastly cooled polyamide melt. Slowly cooled melts may form bigger spherulites, but rapidly cooled surface layers may be quite different from that of the more slowly cooled center zones [Chanda 2007].

Moreover, the drawback of polyamides comes from the ability of these thermoplastics to absorb water as the water molecules can interact with the polar amide groups of the polyamides. The water absorption behavior of this material has to be taken in consideration as it reduces the mechanical properties of the polyamides, as shown in Table 2.2. The water absorption behavior of polyamides and its composites will be discussed in detail in Chapter 4.

	RH = 0% - 23°C	RH = 50% - 23°C
Density (g cm^{-3})	1.14	-
Tensile modulus (GPa)	3	1.5
Yield stress (MPa)	90	60
Yield strain (%)	6	30
Melting temperature (°C)	263	-

Table 2.2: Properties of Technyl® A218, unfilled polyamide-66 produced by Solvay Engineering Plastics, at two different relative humidity content.

2.1.3 Short glass fiber reinforced polyamide-66

Short glass fiber reinforced polyamides are widely used for automotive components. Through an established technology and high productivity of injection molding process, short glass fibers integration into polyamide-66 is proved to be beneficial in terms of mechanical properties enhancement. By reinforcing with 30 wt% short glass fibers, the mechanical and physical properties of polyamide-66 improve significantly, as shown in Table 2.3. As compared with the properties of unfilled polyamide-66 presented in Table 2.2, reinforcing polyamide-66 with 30 wt% glass fiber results in increases of tensile modulus and strength higher than 200% and 100%, respectively. Moreover, the reinforced polyamide-66 offers high temperature stability of up to 200 ^{o}C. In brief, short glass fiber reinforced polyamide-66 exhibits excellent mechanical properties, such as stiffness and strength, along with high temperature resistance. However, water absorption behavior of the polyamide matrix remains a challenge to acquire an optimum use of this composite. Therefore, it is important to gain a proficient knowledge on the actual application of this material, especially the effect of environmental conditions on the corresponding mechanical properties. Proper design of the short glass fibers reinforced polyamide-66 would lead to high possibility of further development of this material to be applied in various automotive applications. The end result is a contribution towards reducing vehicle weight, leading to improved fuel consumption and reduction of CO_2 pollution.

	RH = 0% - 23°C	RH = 50% - 23°C
Density (g cm^{-3})	1.37	-
Tensile modulus (GPa)	10	7
Yield stress (MPa)	190	135
Elongation at break (%)	3	4
Melting temperature (°C)	263	-

Table 2.3: Properties of Technyl® A218V30, polyamide-66 reinforced with 30 wt% short glass fiber produced by Solvay Engineering Plastics, at two different relative humidity content.

2.2 Processing of short fiber reinforced thermoplastic composites

Injection molding is a conventional technique for fast manufacturing of thermoplastics. Nowadays, injection molding is also extensively employed in the production of short fiber reinforced thermoplastic composites. These materials are widely applied for various applications as they are commercially attractive. Though they do not have as high level of stiffness and strength as their continuous fiber reinforced counterparts, they have advantages of low cost and better surface quality. In addition, injection molding process allows complex geometry parts to be easily manufactured in large series and short cycle-time production.

Prior injection molding process, the composite's constituents, which consists of an adjusted content of the thermoplastic matrix and short fibers, as well as the required additives or processing aids, must be prepared. The composite's compound is usually prepared in a twin-screw extruder to obtain a good mixing between all the constituents. After pre-drying process, the compound is prepared by feeding the constituents in separate feeders. The fibers are normally fed into the extruder at the secondary feeder to reduce the abrasion in the extrusion barrel. Each feeder has ability to feed the constituent in a specific flow rate so that the final weight or volume ratio of the compound can be adjusted precisely. As the constituents are inserted into the heated extrusion barrel, the plasticization and mixing processes are commenced. Since the melt compound may emit vapors or gases, degassing process through a venting channel prior finishing the extrusion process is important to remove them to prevent porosity in the product. In polyamide processing, the venting channel can also be used to adjust the water content and viscosity index of the material. After being extruded, the compound is then cooled and cut in the form of pellets or granules. The schematic of the extrusion process can be seen in Fig. 2.4.

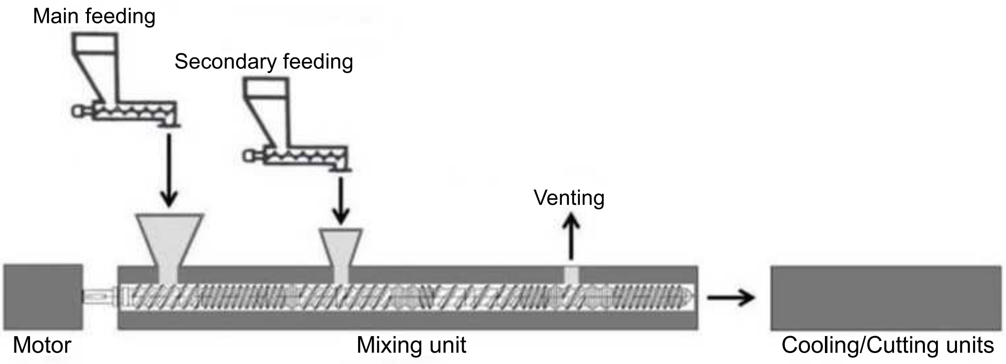

FIGURE 2.4: The schematic of extrusion compounding process [SPE].

The composite granules are then introduced into a heated cylindrical barrel of the injection molding machine. The plasticization process starts as the granules are heated up to above the melting temperature of the thermoplastic matrix. The process then continues with injection process of the composite melt into a closed mold. Packing process is then required in order to maintain the injected material inside the mold under pressure for a specific time to prevent back-flow and to compensate volume decrease of the composite melt during the solidification process. The subsequent step involves cooling of the thermoplastic molded part inside the mold until it is sufficiently rigid and ready to be ejected. The illustration of the operating cycle of an injection molding machine is described in Figure 2.5.

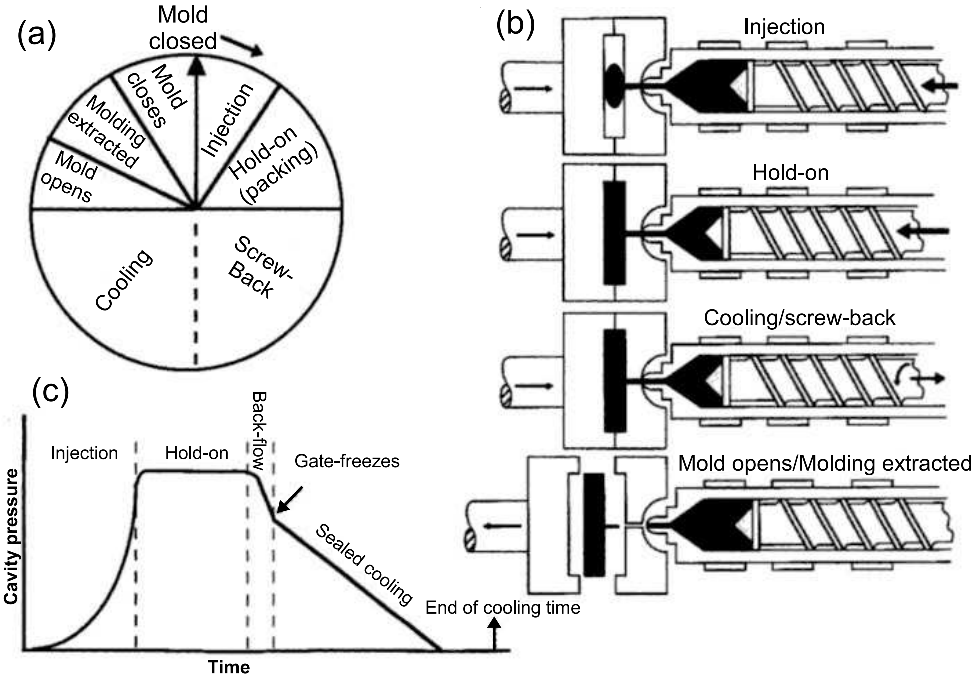

FIGURE 2.5: The operating cycle of an injection molding machine illustrated in a 'clock' format (a) and in a schematic machine function (b). Schematic cavity pressure vs. time profile (c) shows the variation of pressure within the mold cavity in response to molding cycles. [Wilkinson 1998]

2.3 Injection molding induced microstructure

The injection process of short fiber reinforced thermoplastics can induce a complex anisotropic microstructure in terms of its spatial fiber orientation and distribution. The fibers are suspended in the polymer matrix, and orient themselves in response to the interactions among kinematics of the flow, other neighboring fibers and mold cavity. There are many factors influencing the anisotropic degree of the microstructure such as the rheological behavior of the fiber suspension, fiber content and processing variables (i.e. the position and number of injection gates, temperature of the molten mass, mold temperature, filling time, injection pressure, gating system, cavity geometry, etc.) [De Monte 2010b].

In case of a simple mold geometry, such as a composite compound injected into a thin parallel cavity, a layered structure consisting of skin-shell-core formation through the thickness of the injected sample can be developed [Horst 1997a, Bernasconi 2007, Nouri 2009b, Seignobos 2009, De Monte 2010b, Klimkeit 2011]. In fact, for a system where polymer melt flows through a small cavity between two parallel walls, shear flow has maximum value near to the mold wall whereas it vanishes at the core zone, as illustrated in Fig. 2.6. This leads the fibers to be oriented parallel (and perpendicular) to MFD at the shell (and core) layers. Moreover, a thin random skin layer can be formed due to the polymer melt that is in direct contact with a relatively cold mold wall temperature. Usually the injection molding variables are set in such a way to minimize the width of the core layer, thus obtaining a pronounced fiber alignment in flow direction. For a detailed review on the physical phenomena and thermomechanical environment during injection molding, one can refer to [Agassant 1991, Wilkinson 1998, Cunha 2000].

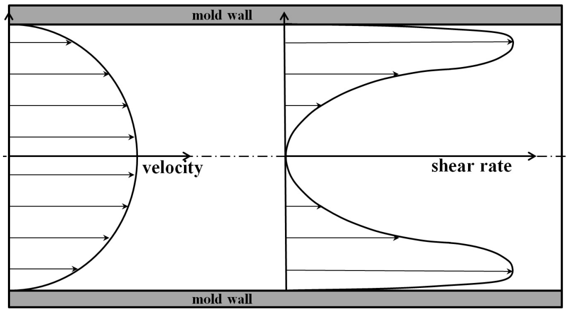

FIGURE 2.6: Illustration of the velocity and shear rate profiles inside a mold cavity. The relative magnitude of the profiles along the thickness can be different depending on the processing parameters.

2.4 Description of fiber orientation state

Since fiber orientation state in the composite governs its final properties, developing a characterization technique to determine the fiber orientation is important. Many different quantification methods have been applied to measure the local fiber orientation and its distribution. The classical approach to characterize the fiber orientation is achieved by optical or electron microscope 2D images of the specimen cut surfaces. The quantification of the fiber orientation is performed by measuring the Euler angles of the elliptic cut of the 2D image fibers [Clarke 1995, Eberhardt 2001, Lee 2002, Dray 2006]. This method is time consuming and not all fibers can be accounted for. An efficient and precise method to characterize the fiber orientation is by using three-dimensional X-Ray tomography (μCT) measurement. This enables the identification of almost all fibers inside the material and evaluate the orientation tensors in any arbitrary space.

The quantification analysis of fiber orientation during the injection process involves numbers of rheological phenomena. The work on this subject was initiated by Jeffery [Jeffery 1922] who studied the motion of ellipsoidal particles immersed in a viscous fluid. The concept of orientation tensor was then introduced by Hand [Hand 1961] and further reviewed by Advani and Tucker [Advani 1987]. Nowadays, the orientation tensor is widely adapted to describe the fiber orientation state due to their compact representation of the fiber orientation state and their independence on the coordinate system. This advantage has made the orientation tensor to be extensively applied in fiber orientation evaluation [Eberhardt 2001, Chung 2002, Lee 2002, Megally 2005, Redjeb 2007]. Also, this concept has been established for a material property prediction in short fiber composites due to its easy implementation into a micromechanical modeling [Laspalas 2008, Launay 2013a].

A complete description of the fiber orientation can be started by considering a single fiber. Generally, orientations of a single fiber are represented by Euler angles of θ and ϕ, as shown in Fig. 2.7. In Cartesian coordinates, it can be represented as a unit vector $\vec{p}$ parallel to the fiber (Eq. 2.1).

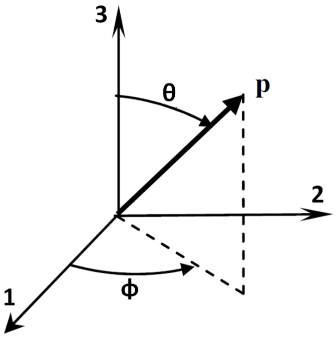

FIGURE 2.7: The definition of orientation of a single fiber.

$$\vec{p} = \begin{pmatrix} \sin\theta\cos\phi \\ \sin\theta\sin\phi \\ \cos\theta \end{pmatrix} \tag{2.1}$$

Describing the orientation of individual fibers is ineffective since the composites contain numerous short fibers. Therefore, the concept of probability distribution function [Advani 1987], also known as the orientation distribution function, was introduced to fully describe the fiber orientation distribution in three dimensions. The probability distribution function $\psi(\theta,\phi)$ is defined as the probability of fiber lying between angles θ and $\theta + d\theta$, ϕ and $\phi + d\phi$. The probability distribution function must fulfill two conditions. First, a fiber oriented at any angle (θ,ϕ) is indistinguishable from a fiber oriented at any angle $(\pi-\theta,\phi+\pi)$, and thus

$$\psi(\theta,\phi) = \psi(\pi-\theta,\phi+\pi) \quad \text{or} \quad \psi(\vec{p}) = \psi(-\vec{p}) \tag{2.2}$$

Second, the integral over all possible orientations must be equal to unity:

$$\int_0^{2\pi}\int_0^{\pi}\psi(\theta,\phi)\sin\theta\,\mathrm{d}\theta\,\mathrm{d}\phi=\oint\psi(\vec{p})\mathrm{d}\vec{p}=1 \tag{2.3}$$

Although the computation of probability distribution function can be done using any numerical techniques, it requires tremendous computational efforts. Therefore, for a more efficient method of numerically simulating the orientation state of fiber, Advani and Tucker [Advani 1987] adopted orientation tensors. Such tensors are defined as the moments of the function ψ. The second and fourth order orientation tensors can be defined as:

$$a_{ij}=\oint p_ip_j\psi(\vec{p})\mathrm{d}\vec{p}=\langle p_ip_j\rangle \tag{2.4}$$

$$a_{ijkl}=\oint p_ip_jp_kp_l\psi(\vec{p})\mathrm{d}\vec{p}=\langle p_ip_jp_kp_l\rangle \tag{2.5}$$

where $\vec{p}$ is the unit vector parallel to the fiber, $p_ip_jp_kp_l$ are the tensor components and the brackets $\langle\rangle$ represent the averaging over all orientations of a finite population of fibers.

These tensors are by definition symmetric (i.e. $a_{ij}=a_{ji}$) and normalized (i.e. $a_{ii}=1$). If one considers the second-order tensor, it has nine components but only five of these are independent because of the symmetry and normalization conditions. If a single fiber k orientation (θ^k,ϕ^k) is considered, the second-order tensor components $\left[a_{ij}^k\right]$ of Eq. 2.4 can be expressed as follows:

$$\left[a_{ij}^k\right]=\begin{bmatrix}\sin^2\theta^k\cos^2\phi^k & \sin^2\theta^k\cos\phi^k\sin\phi^k & \sin\theta^k\cos\theta^k\cos\phi^k\\ \sin^2\theta^k\cos\phi^k\sin\phi^k & \sin^2\theta^k\sin^2\phi^k & \sin\theta^k\cos\theta^k\sin\phi^k\\ \sin\theta^k\cos\theta^k\cos\phi^k & \sin\theta^k\cos\theta^k\sin\phi^k & \cos^2\theta^k\end{bmatrix} \tag{2.6}$$

If n number of fibers are considered, the orientation tensor can be obtained by averaging the contributions of each fiber. Hence, the second-order tensor components of Eq. 2.4 can be evaluated by the following discrete approach:

$$a_{ij}=\frac{1}{n}\sum_{k=1}^{n}a_{ij}^k=\frac{1}{n}\sum_{k=1}^{n}p_i^kp_j^k \tag{2.7}$$

The examples of physical interpretation of the second-order tensor in some particular states of *in-plane* fiber orientation can be seen in Fig. 2.8. According to Fig. 2.8a and b, if the principal axis of fiber orientation distribution is aligned with the axis of coordinate system, the orientation tensor is diagonalized. Indeed, the diagonal components indicate the magnitude of fiber alignment in the respective direction. For the randomly oriented fiber of Fig. 2.8b, the principal axes are aligned in both axis-1 and axis-2 equally and thus the diagonal components share the same magnitude. If the principal axis is not aligned with the coordinate system (Fig. 2.8c), the off-diagonal components of the orientation tensor are non-zero. In this case, the off-diagonal components show rotation of the principal axis with respect to the coordinate system.

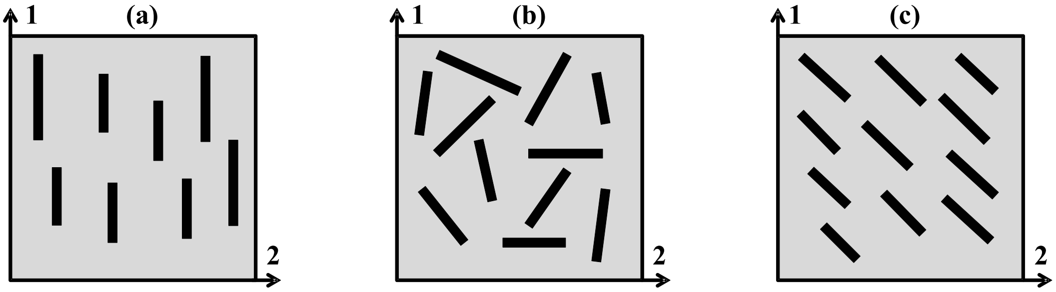

$$a_{ij} = \begin{bmatrix} 1 & 0 \\ 0 & 0 \end{bmatrix} \qquad a_{ij} = \begin{bmatrix} 0.5 & 0 \\ 0 & 0.5 \end{bmatrix} \qquad a_{ij} = \begin{bmatrix} 0.5 & 0.5 \\ 0.5 & 0.5 \end{bmatrix}$$

FIGURE 2.8: Examples of different *in-plane* fiber orientation states and its corresponding 2^{nd} order orientation tensors.

2.5 X-Ray microtomography

The X-ray micro-computed tomography (μCT) is a non-destructive technique which allows to visualize an object in 3D. Thanks to its capacity, μCT has been widely used in materials science [Maire 2001b, Stock 2008, Laiarinandrasana 2010, Withers 2012]. This technique was also proved to be effective to study the microstructure (fiber orientation) in various composites [Eberhardt 2002, Shen 2004, Bernasconi 2008, De Monte 2010b, Bernasconi 2012, Miettinen 2012, Suuronen 2012, Müller 2013, Arif 2014b].

This technique comprises an X-Ray source, a rotating table and an X-ray detector (Fig. 2.9). The studied sample is placed between the X-ray beam and the CCD camera detector. The μCT technique follows Beer-Lambert law (Eq. 2.8) which shows logarithmic dependence between the initial intensity of photons I_0 and the intensity of transmitted photons I across a traveled distance x.

$$I = I_0 e^{-\mu x} \tag{2.8}$$

The attenuation coefficient μ describes the fraction of an X-ray beam that is absorbed or scattered per unit thickness of the sample. In case of a heterogeneous sample, different μ yields to a different intensity of the transmitted photons (Fig. 2.10). The radiograph is obtained by a projection of the attenuation data along the path of the photons. An important use of the attenuation coefficient is for selecting a radiation energy that can produce the most contrast between particular materials in a radiograph.

For three-dimensional visualization of the material, μCT combines information provided by a large number of radiographs, each being made from a different angle of the sample with respect to the X-rays source and detector that remain fixed. If the incremental acquisition angle between radiographs is small enough, it is possible to reconstruct the three-dimensional information of the material from a complete set of radiographs by using filtered back projection algorithm (Fig. 2.11), resulting in high number of two-dimensional sections, as described in Fig. 2.12. The volume of the material is then reconstructed slice by slice.

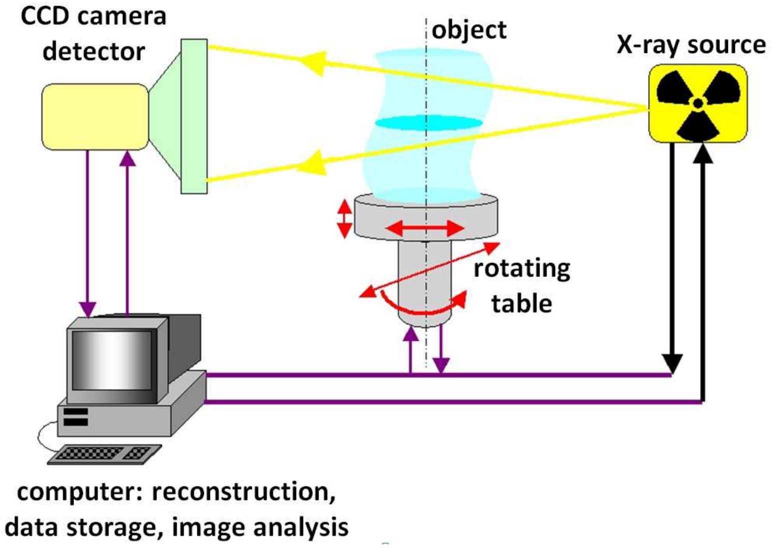

FIGURE 2.9: Schematic of X-Ray micro-tomography experimental setup [Madi 2006].

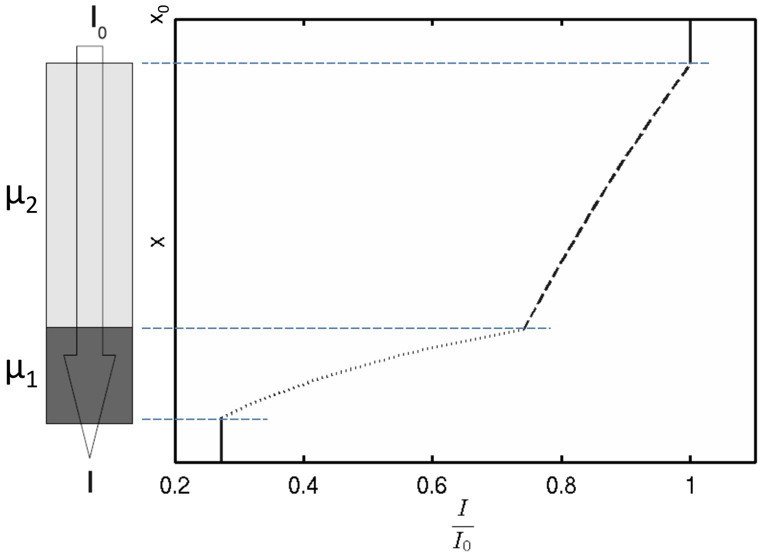

FIGURE 2.10: Beam attenuation along a bi-material specimen ($\mu_1 < \mu_2$) [Carmona 2009].

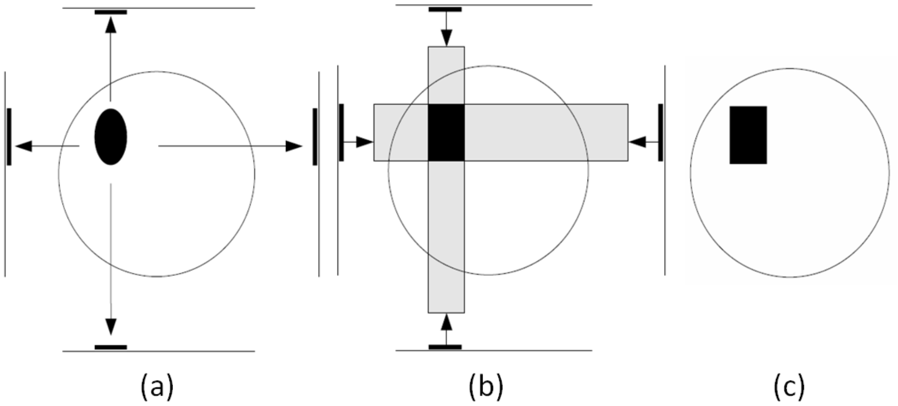

FIGURE 2.11: Principle of filtered back-projection: (a) projection, (b) back-projection, (c) filter. A large number of projections is necessary to define correctly the 3D object [Carmona 2009].

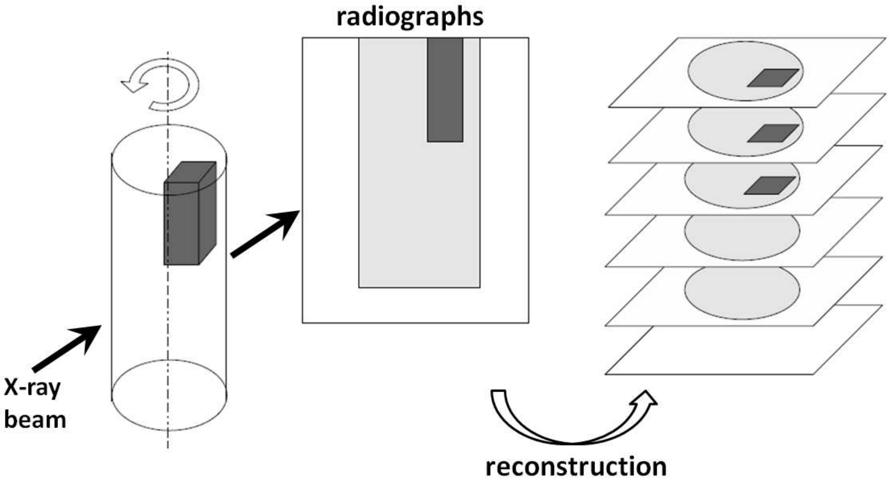

FIGURE 2.12: Principle of tomography [Carmona 2009].

2.6 Microstructure description of the studied PA66/GF30

The material used in this work is Technyl® A218V30, a commercial grade of PA66/GF30 supplied by Solvay Engineering Plastics-France. The material was prepared by compounding the polyamide-66 pellets and 30 wt% of chopped short glass fibers in a twin-screw extruder. Subsequently, the PA66/GF30 compound was transferred into an injection molding machine, resulting in $360 \times 100 \times 3.2$ mm^3 of rectangular plate.

X-ray micro-computed tomography (μCT) technique was employed to study the microstructure heterogeneity of PA66/GF30 in terms of its fiber orientation. The μCT experiment was carried out at ID19 beam line of the European Synchrotron Radiation Facility (ESRF) Grenoble, France [ID19 ESRF]. For this microstructure investigation, the experimental setup was conditioned to reach a voxel resolution of 1.4 μm. Two samples for μCT experiments were extracted from the injection molding plate at two positions along mold flow direction (MFD) axis, A and B, as shown in Fig. 2.13. The selected positions were significantly far from the complex flow zones of the material at the initial and final filling stages. Indeed, nonuniform microstructure is usually found at these complex flow zones. Moreover, the selected positions were also used as a guideline for specimens extraction for the tensile and fatigue tests that will be discussed in Section 2.7. The dimensions of the μCT samples were $2 \times 2 \times 3.2$ mm^3, where 3.2 mm corresponds to the sample thickness. The μCT scanning was not carried out through all the sample thickness but it always covered more than half of the thickness so that the skin-shell-core structure can always be captured. As a qualitative confirmation, scanning electron microscope (SEM) was employed to observe the polished surfaces at the position B of the injection molding rectangular plate.

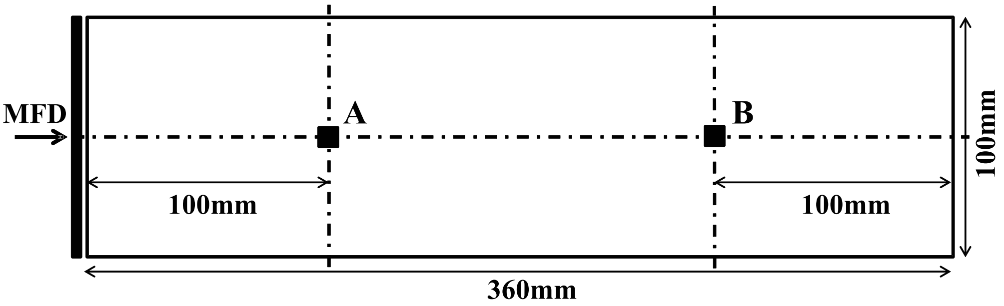

FIGURE 2.13: The locations of injection molding induced microstructure investigation (A and B).

The microstructure of PA66/GF30 obtained from the μCT sample extracted from the location A of Fig. 2.13 is shown in Fig. 2.14. It can be seen from Fig. 2.14, PA66/GF30 has a specific injection process induced microstructure characterized by a skin-shell-core structure. Moreover, transition layer between shell and core is also observed. The microstructure of PA66/GF30 extracted from the location B of Fig. 2.13 exhibits the same trend as the one extracted from the location A. An assessment by SEM method from the location B of the injection plate with the whole through-thickness representation demonstrates similar trend, as presented in Fig. 2.15. It is worth noting that this microscopic condition was achieved by an optimal set up of injection molding parameters (barrel and mold temperatures, injection speed, etc.) to ensure a high compaction degree of the composite and to reduce the core layer thickness.

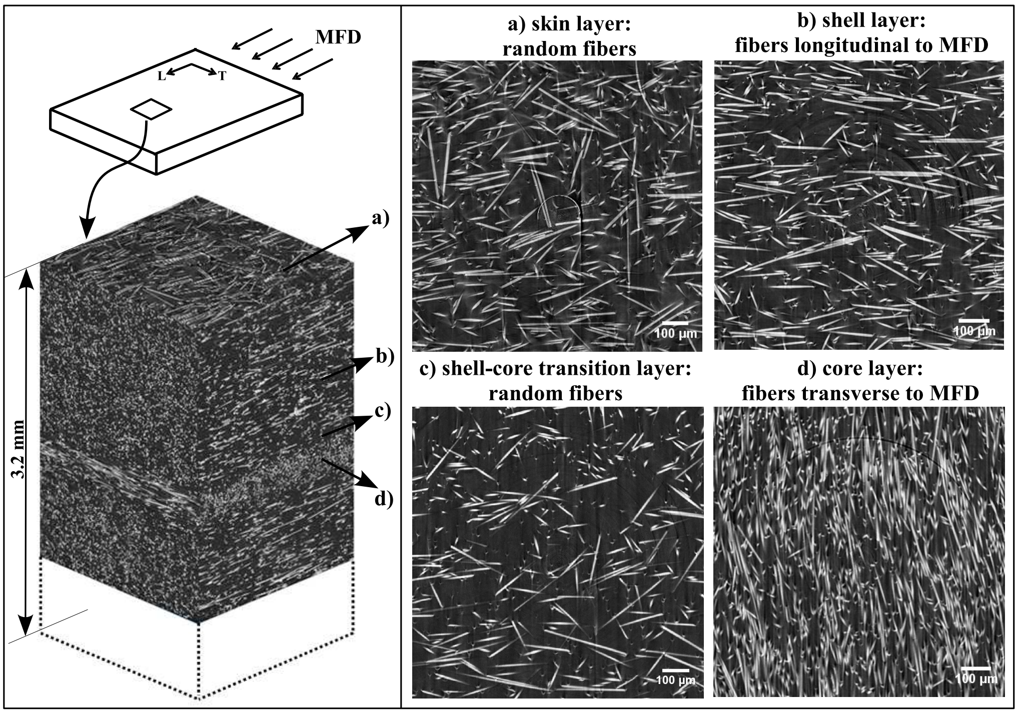

FIGURE 2.14: The skin-shell-core microstructure formation of PA66/GF30 observed by μCT.

To acquire the real tendency of fiber orientation throughout the sample, fiber orientation tensors were computed based on the results of the μCT measurements. A strategic method of μCT 3D image segmentation of the fibers via gray level thresholding has been developed to capture efficiently the Euler orientation angles of the fibers. Avizo and Visilog softwares were used for this purpose. The second-order fiber orientation tensors have been computed based on the data of fibers' Euler angles. After the thresholding process is achieved, the 3D reconstructed image of fibers along with the fiber features such as the Euler orientation angles can be extracted. An example of the 3D reconstructed image of the fibers in a small portion of μCT volume can be seen in Fig. 2.16. It is worth noting that the numerical treatments to obtain the fiber orientation tensors were performed in collaboration with the industrial partner. Therefore, all the procedures are considered confidential and the results are presented in normalized axes.

The second-order fiber orientation tensors have been computed based on Eq. 2.4. The normalized tensor components of the two studied μCT volumes are shown in Fig. 2.17. The tensor components of a_{11}, a_{22} and a_{33} represent the degree of fibers to be oriented in

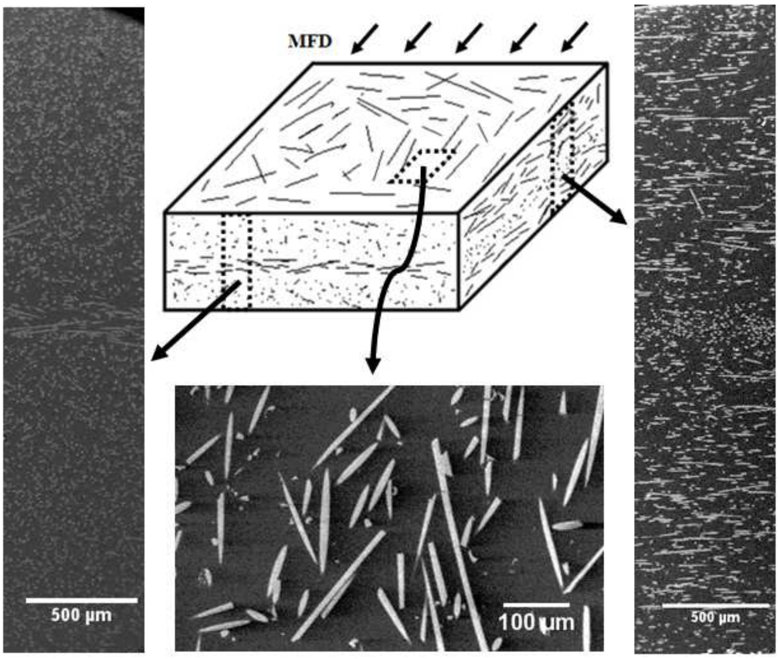

FIGURE 2.15: The skin-shell-core microstructure formation of PA66/GF30 observed by SEM.

longitudinal, transverse and short transverse (through-thickness) directions with respect to the MFD, respectively. The higher value of the normalized tensor component constitutes higher tendency of fibers to be oriented to the associated direction. It can be seen from Fig. 2.17 that the skin-shell-core layers of the two μCT volumes are well-defined. In addition, small transition regions between the shell and core layers are also observed. It is worth noting that the fiber orientation tensor in the short transverse direction (a_{33}) is constant and thus the fiber orientation varies only along longitudinal and transverse directions ($1-2$ plane).

Based on the qualitative observations by μCT and SEM and the quantitative analysis of fiber orientation tensors, it can be seen that the skin layers, the upper and lower specimen surfaces, are slightly random in fiber orientation. However, the orientation tensor a_{11} in both location A and B shows that the principal fiber orientation in the skin layer tend to follow the MFD. The shell layers are the most dominant ones with preferential fiber orientation longitudinal with respect to MFD. Thin core layer is developed and mostly fibers in this layer are oriented transversely to the MFD. It is worth noting that instead of purely oriented in transverse direction to the MFD, it has been frequently observed that the fibers in the core layer are slightly tilted around 5^o to 20^o from the transverse direction, such as the one shown in Fig. 2.14d. This can also be seen from the non zero tensor component of a_{12} at the core region, as shown in Fig. 2.18. In addition to the skin, shell and core microstructures, transition layers between shell and core are also observed, as shown in Figs. 2.14c and 2.17.

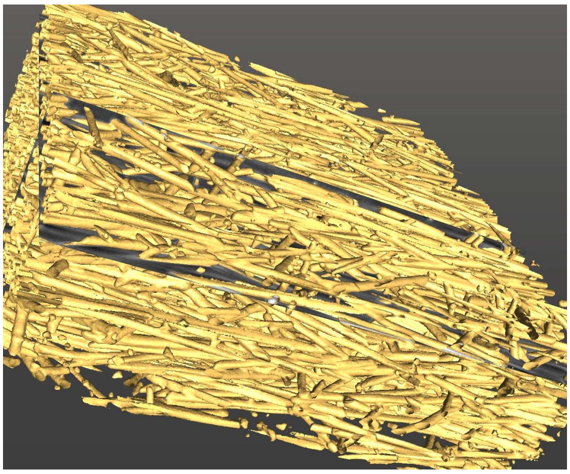

FIGURE 2.16: The 3D image of fibers after the thresholding process.

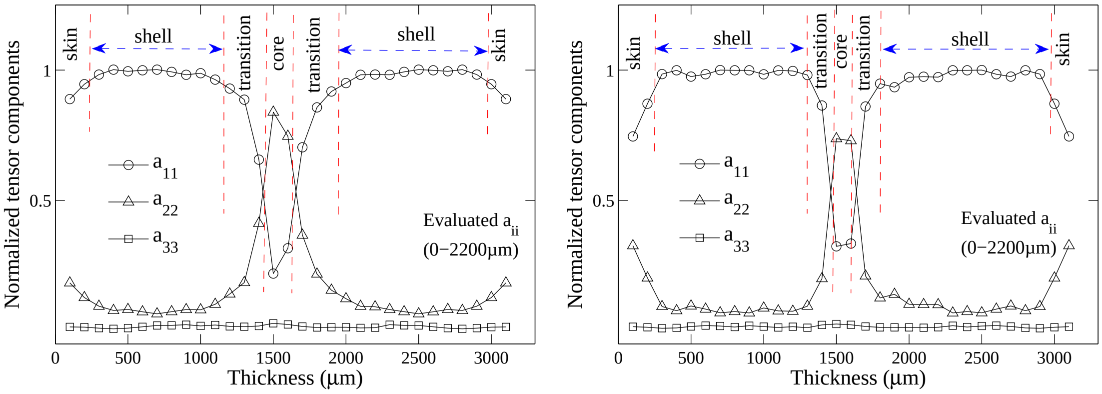

(a) Sample extracted from location A of Fig. 2.13 (b) Sample extracted from location B of Fig. 2.13

FIGURE 2.17: Normalized tensor components of a_{11}, a_{22} and a_{33} along the thickness of the two studied samples. The tensor components are evaluated from 0 to 2200 μm thickness. The ones above 2200 μm are assumed to be symmetric with another half of the thickness. The tensors are normalized with the maximum value of a_{11}.

The normalized orientation tensors of the two studied samples show that both positions exhibit almost the same state of fiber orientations. Only small differences on the width of the shell-core transition zones and the orientation state of the skin layers are observed between the two studied samples. It can be inferred from the results that the microstructures developed along the MFD axis of the injection molding plate are generally homogeneous.

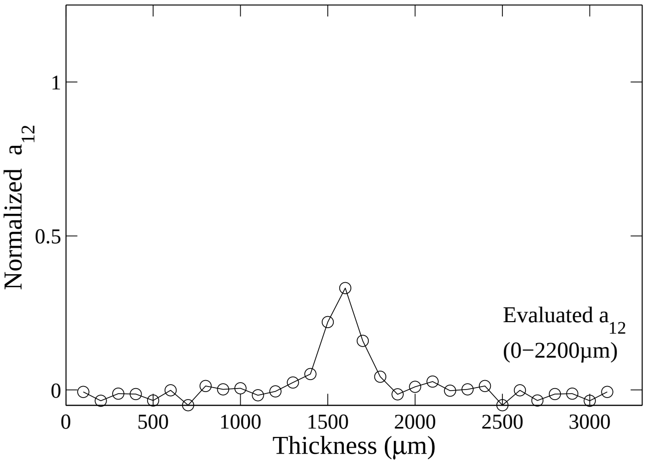

FIGURE 2.18: The normalized tensor component of a_{12} at location A of the rectangular plate. The a_{12} is evaluated from 0 to 2200 μm thickness. The one above 2200 μm is assumed to be symmetric with another half of the thickness. The tensors are normalized with the maximum value of a_{11}

2.7 Specimens for mechanical testings

In this thesis work, specimens used for tensile and fatigue tests were machined from the rectangular plate produced by injection molding process. As discussed earlier, PA66/GF30 exhibits an anisotropic behavior due to the skin-shell-transition-core microstructures. Moreover, the microstructures developed along the MFD axis of the injection molding plate are generally homogeneous. The specimens extraction locations are selected basically based on these considerations.

To consider the anisotropy effect of the composite, the specimens were machined in longitudinal and transverse directions with respect to the MFD, defined hereafter as *the longitudinal and transverse specimens*. To ensure microstructure homogeneity between all specimens, the gauge-length zones were assured to be along the MFD axis. Moreover, the locations of the specimen extraction were chosen far from the injection gate and end-filling zones to anticipate the nonuniform microstructure that may develop at these complex flow regions. The machining positions of longitudinal and transverse specimens, as well as the specimen main dimensions are illustrated in Fig. 2.19. During mechanical tests, the longitudinal and transverse specimens were selected randomly from these locations.

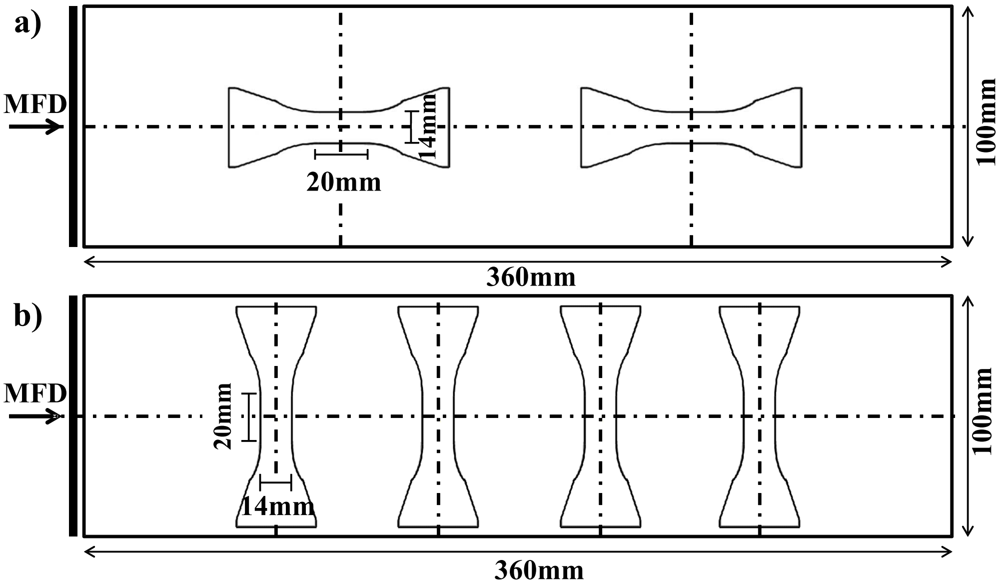

FIGURE 2.19: Machining locations of a) longitudinal and b) transverse specimens, as well as the main specimen dimensions of PA66/GF30.

2.8 Concluding remarks

The characteristics, advantages and limitations of using PA66/GF30 have been discussed. PA66/GF30 exhibits excellent mechanical properties along with high temperature resistance. However, water absorption properties of PA66/GF30 need to be considered as it influences the mechanical properties of the composite. Due to its lightweight characteristic, a contribution towards reducing vehicle weight, leading to the improved fuel consumption is expected.

The microstructure of PA66/GF30 has been evaluated. Based on qualitative observations by μCT and SEM, and quantitative analysis of fiber orientation tensors by μCT, a skin-shell-transition-core formation was observed. The shell layers are the most dominant ones with preferential fiber orientation longitudinal with respect to MFD. The skin layers, the upper and lower specimen surfaces, are slightly random in fiber orientation. Thin core layer is developed and mostly fibers in this layer are oriented transversely to the MFD. It is worth noting that slightly tilted fibers around 5^o to 20^o from the transverse direction were frequently observed in this core layer.

Based on the analyzed tensor components, it was observed that the fiber orientation varies only along longitudinal and transverse directions ($1-2$ plane). The normalized orientation tensors of the two studied samples showed that both positions exhibit almost the same state of fiber orientations. Therefore, it can be inferred that the microstructures developed along the MFD axis of the injection molding plate are generally homogeneous.

To consider the anisotropy effect of PA66/GF30, the locations of specimens' extraction for mechanical characterizations have been detailed. The specimens are extracted into two directions, longitudinal and transverse with respect to the MFD, defined hereafter as *the longitudinal and transverse specimens*.

CHAPTER 3

Overall mechanical and damage behavior of PA66/GF30

Contents

In this chapter, the mechanical behavior and properties, as well as the general idea on damage behavior of PA66/GF30 are studied. The anisotropy effects induced by the injection molding process is studied from the stress-strain curves, the Wohler curve and the evolution of $\varepsilon_{11}, \varepsilon_{22}$ and ε_{33} in longitudinal and transverse specimens. The effect of strain rate, temperature and relative humidity conditions on the mechanical properties of PA66/GF30 are also discussed. Moreover, the viscoelastic behavior of polyamide-66 matrix is analyzed by dynamic mechanical analysis (DMA) technique. Particular attention is given to the contribution of viscous effect and damage on the mechanical behavior of PA66/GF30 by volume change method, thermography and tensile tests with load releases.

3.1 Tensile behavior and properties

3.1.1 Stress-strain curve

Quasi-static tensile tests on dry as molded, longitudinal and transverse specimens of PA66/GF30 were performed at room temperature and crosshead speed of 1 mm/min, which corresponds to the strain rate of 3×10^{-4} s^{-1}. The results of the tensile tests are described in Fig. 3.1. This figure illustrates the strong anisotropy effect induced by the injection molding process. The Young modulus and ultimate stress of the longitudinal specimens are around twice higher than the ones of the transverse specimens. Nevertheless, strain to failure characterizing the material ductility of the longitudinal specimens is around half than that of the transverse specimens. As discussed earlier in Section 2.6, the fiber orientations through the thickness of the specimens are predominantly occupied by the shell layer where the fibers are longitudinally oriented to the MFD. This yields the shell layer to dominantly govern the tensile behavior of PA66/GF30.

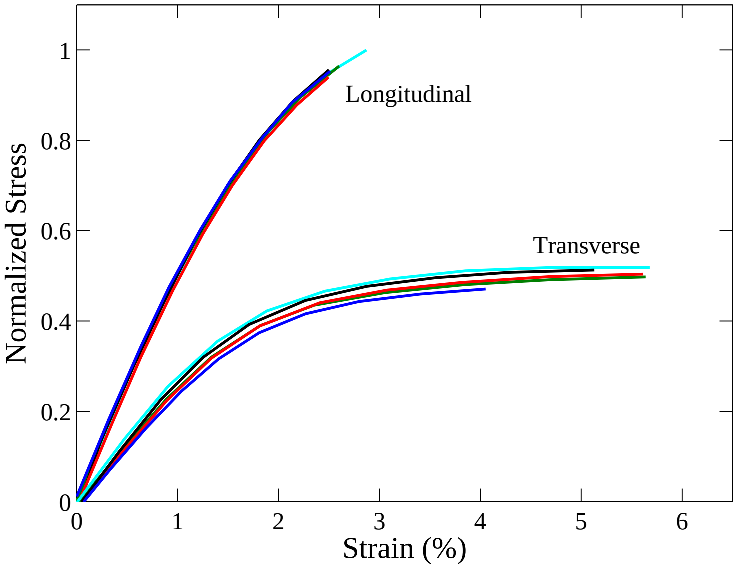

FIGURE 3.1: Tensile properties of longitudinal and transverse specimens of PA66/GF30. The stress is normalized with the ultimate tensile stress of longitudinal specimen.

Moreover, Fig. 3.1 illustrates different data scatter between longitudinal and transverse specimens. Transverse specimens demonstrate a much larger data dispersion than that in longitudinal specimens. This is probably due to the fiber orientation variability in the core layer. As previously discussed in Section 2.6, instead of exclusively oriented transversely to the MFD, tilted fibers around 5^o to 20^o are frequently observed. Since the core layer in the transverse specimens is responsible for the load transfer mechanism due to its parallel orientation to the applied load direction, the variability of the fiber orientation in the core layer may lead to a data scatter in the mechanical properties of the transverse specimens.

3.1.2 Planar anisotropy behavior

By the digital image correlation (DIC) technique applied onto the width and thickness surfaces of the specimen during tensile loading, one can measure the strain values in three principal directions, i.e. $\varepsilon_{11},\varepsilon_{22}$ and ε_{33}, which correspond respectively to the strain along the direction of the applied load (1), width (2) and thickness (3). The review on DIC technique employed in this work can be seen in Appendix A.

Fig. 3.2 shows different planar anisotropy behavior between longitudinal and transverse specimens. The negative values of ε_{22} and ε_{33} signify that the width and thickness of the specimen decreases during tensile loading. It can be seen that for longitudinal specimens, $\mid \varepsilon_{22} \mid$ is larger than $\mid \varepsilon_{33} \mid$. In contrast, the transverse specimens demonstrate the opposite behavior as $\mid \varepsilon_{33} \mid$ is larger than $\mid \varepsilon_{22} \mid$.

For longitudinal specimen, the fiber density (notably in the shell layer) along the thickness of the specimen is higher than that along the width, which leads to a lower strain in the thickness direction. In case of transverse specimen, the presence of important amount of fibers oriented transversely to the loading direction prevents the strain through the width direction to evolve and thus $\mid \varepsilon_{22} \mid$ is lower than $\mid \varepsilon_{33} \mid$. The current results is in accordance with the data of Solvay Engineering Plastics for injection molded polyamide-66 reinforced with 20 wt% short glass fibers conditioned at 50% relative humidity [Kammoun 2011a].

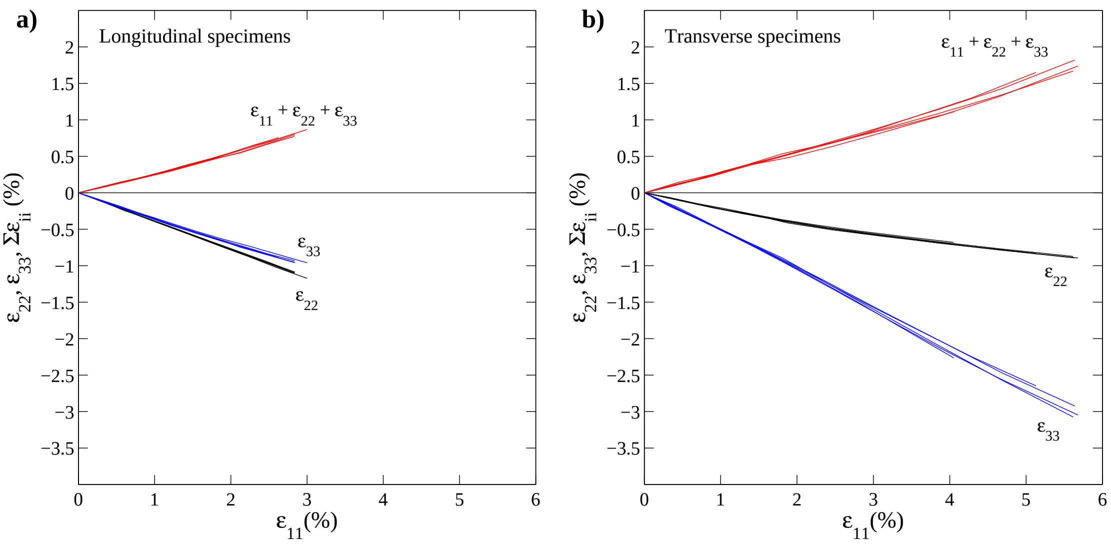

FIGURE 3.2: Planar anisotropy behavior of a) longitudinal and b) transverse specimens of PA66/GF30 observed during tensile tests along axis-1 direction. Axis-2 and -3 are the direction along the width (transverse) and thickness (short-transverse), respectively. For an easier interpretation, both graphs use the same axes scale.

3.1.3 Volume change during tensile loading

By the DIC technique applied onto the width and thickness surfaces of the specimen, one can measure the volume change during tensile loading, by evaluating $\delta V/V = \varepsilon_{11} + \varepsilon_{22} + \varepsilon_{33}$ (see Appendix A for the experimental detail of DIC). Fig. 3.2 shows that the volume of the sample increases continuously during tensile loading. In fact, the volume change inside thermoplastic materials or their reinforced composites can be due to several factors [Arieby 2007]:

- Elastic expansion $\Delta V > 0$
- Damage, voids $\Delta V > 0$
- Crystalline order destruction $\Delta V > 0$
- Amorphous chain compaction $\Delta V < 0$

The volume increases during tensile tests of PA66/GF30 could be dominantly due to the elastic expansion of the material. However, since the damage is also developed during tensile loading, as reported by [Sato 1991, Mouhmid 2006, Arif 2014a], the damage should also contribute to the volume increase of the material. If the stress-strain and volume increase-strain diagrams are presented in one graph, as shown in Fig. 3.3, one can observe two regions in both longitudinal and transverse specimens. The first region corresponds to the elastic response of the material where the volume increase is only due to the elastic expansion of the material. The second region corresponds to the non-linear response of the material where the formation of defects or voids are expected to develop.

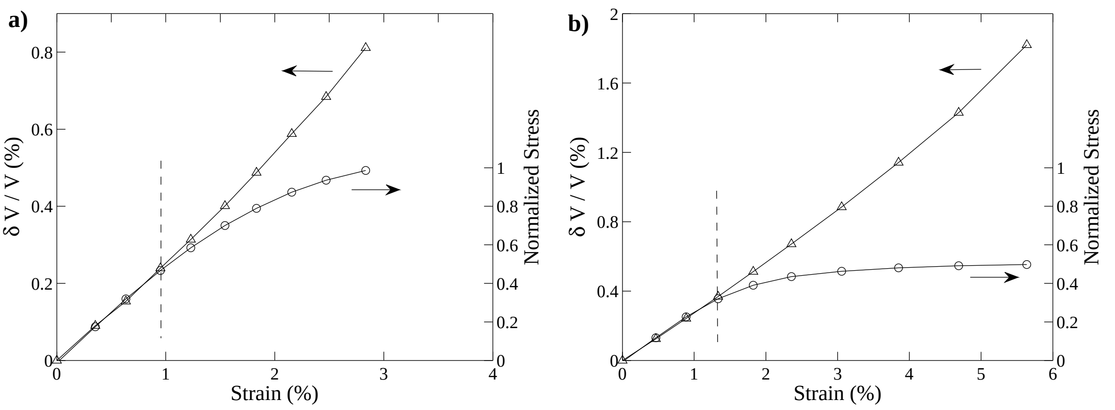

FIGURE 3.3: Stress-strain and volume increase-strain curves of a) longitudinal and b) transverse specimens of PA66/GF30 during tensile loading.

3.1.4 Effect of strain rate and temperature

Tensile tests on dry as molded longitudinal specimens of PA66/GF30 were performed with variation of strain rates and temperatures. The experiments with strain rate of 5×10^{-5} s^{-1} were carried out in five specimens, while the tests with strain rate of 5×10^{-4} and 5×10^{-3} s^{-1} employed only two or three specimens.

Fig. 3.4 shows the general trend of the effect of strain rate and temperature on the mechanical properties of PA66/GF30. In this figure, only one representative stress-strain curve for each temperature and strain rate variable is presented. The effect of strain rate and temperature on the Young modulus, ultimate tensile stress and strain to failure can be seen in Fig. 3.5. In this figure, the mean value and its standard deviation are presented for the tests with strain rate of 5×10^{-5} s^{-1}, while all the data points are presented for the test with strain rate of 5×10^{-4} and 5×10^{-3} s^{-1}.

It can be seen that the strain rate and temperature highly influence the mechanical properties of PA66/GF30. The higher strain rate results in higher ultimate stress and modulus. The temperature contributes to the reverse effect as the higher temperature yields to ultimate stress and modulus reduction. For the strain to failure, it is expected that higher strain rate would reduce the strain to failure while temperature generates the reverse effect. However, one cannot see clearly the trend in the current work. This could be due to the limited results for the tests with strain rate of 5×10^{-4} and 5×10^{-3} s^{-1}.

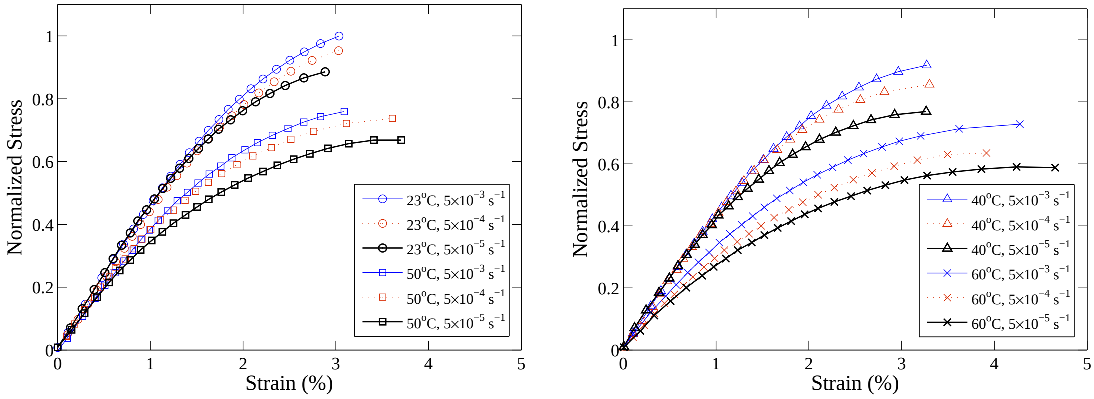

FIGURE 3.4: Effect of strain rate and temperature on the mechanical properties of longitudinal PA66/GF30. Two figure representation is used for a better clarity.

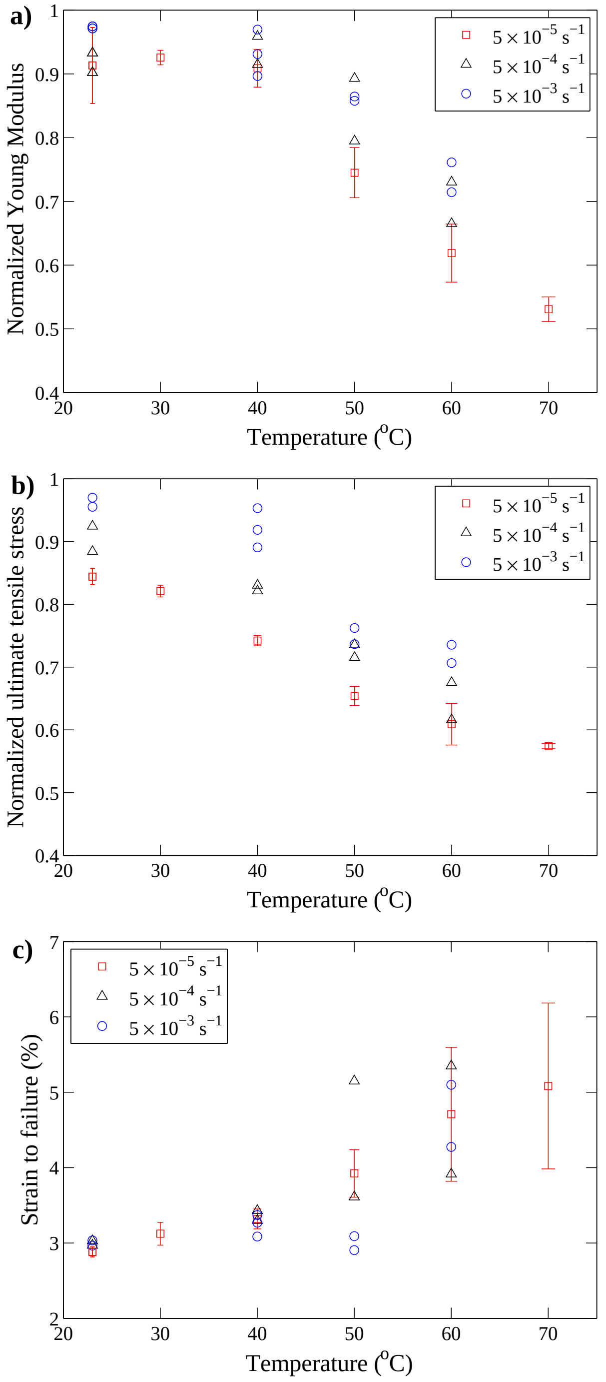

FIGURE 3.5: Effect of strain rate and temperature on a)Young modulus, b) ultimate tensile stress and c) strain to failure of longitudinal PA66/GF30.

3.1.5 Temperature profile

During tensile tests, temperature profiles on the gauge length surface of the specimen have been recorded by an infrared-camera system. It can be seen from Fig. 3.6 that mean temperature decrease is observed during the first loading phase, both in longitudinal and transverse specimens. In fact, this follows general behavior of an elastic solid material under tensile load where the temperature is in opposite phase with respect to the loading.

While the load increases, the damage starts to develop progressively and the mean temperature becomes constant (for both longitudinal and transverse specimens) and then increases (for the transverse specimen). At this region, coupling between the rheology (viscous properties) of PA66/GF30 and the damage starts to take effect. This coupling occurs by the temperature increase inherent to the heat dissipation.

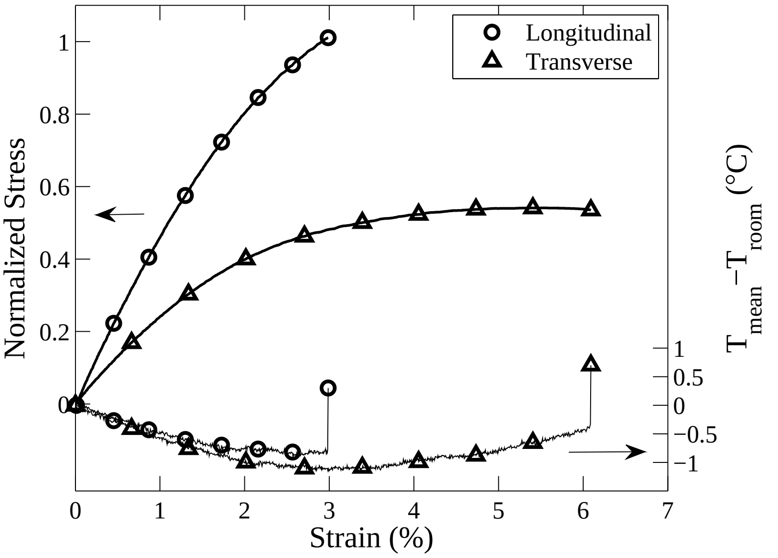

FIGURE 3.6: Mean temperature and stress-strain curves of longitudinal and transverse specimens of PA66/GF30 during tensile loading.

3.1.6 Damage assessment by thermography technique

In a material discontinuity such as damage, heat transfer is hindered since there is only partial or no contact between the internal surfaces of the damage zone. This could result in a local increase of temperature in the damaged zone. If one records the mean and maximum temperature on the active zone area of the specimen, it is expected that the temporal increase of the maximum temperature will be higher than that of the mean temperature when a localized damage is detected. However, the nature of this technique suggests that the level of localized damage should be high enough so that the heat generated in the damage zones can reach the surface and thus can be captured by the infrared thermography camera.

This experimental approach has been examined in dry PA66/GF30 specimens under quasi-static tensile loading. As described in Fig. 3.7, the maximum temperature evolution is approximately the offset of that of mean temperature. This result indicates that during tensile loading, there is no macroscopic damage induced strain localization. It can then be inferred that the damage is preferably diffused over the entire specimen. An increase of maximum temperature is only observed when the loading reaches 99% of the ultimate stress. This is due to the sudden crack propagation leading to the final fracture of the sample.

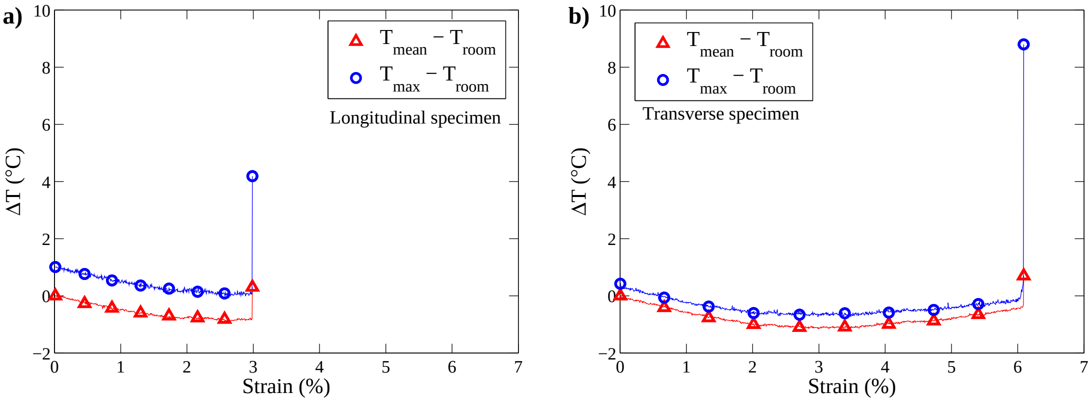

FIGURE 3.7: Evolution of mean and maximum temperature of a) longitudinal and b) transverse specimens during tensile loading of PA66/GF30.

3.1.7 Tensile tests with load releases

Tensile test with full load releases Tensile tests on dry as molded longitudinal and transverse specimens of PA66/GF30 were performed at room temperature and strain rate of 3×10^{-4} s^{-1}. Full load releases up to zero force were carried out at several strain levels with the same strain rate as the one during tensile loading or reloading.

The results of this experiment can be seen in Fig. 3.8. It shows that the hysteresis curve at each unloading-reloading cycle is developed in both longitudinal and transverse specimens. Moreover, the higher load level results in the increase of the hysteresis area, together with the reduction of the hysteresis curve' slope. This change of characteristic is due to the visco(elasto-plastic) behavior of the material and the occurring of damage.

This type of test can also be used to study the damage evolution according to the strain level, by evaluating the hysteresis curve's slope. However, for the present case, the modulus decrease is not exclusively due to the damage as the viscous component of the material also contributes to the modulus reduction.

Nevertheless, it is worth noting that the evolution of the slope of hysteresis curve is usually used for damage evaluation during fatigue loading, as reported by many researchers [Ben Cheikh Larbi 2006, Seignobos 2009, Nouri 2009a, Meraghni 2011, Nouri 2013].

Due to the high strain rate employed in fatigue tests, the viscous component-induced modulus reduction is therefore can be minimized.

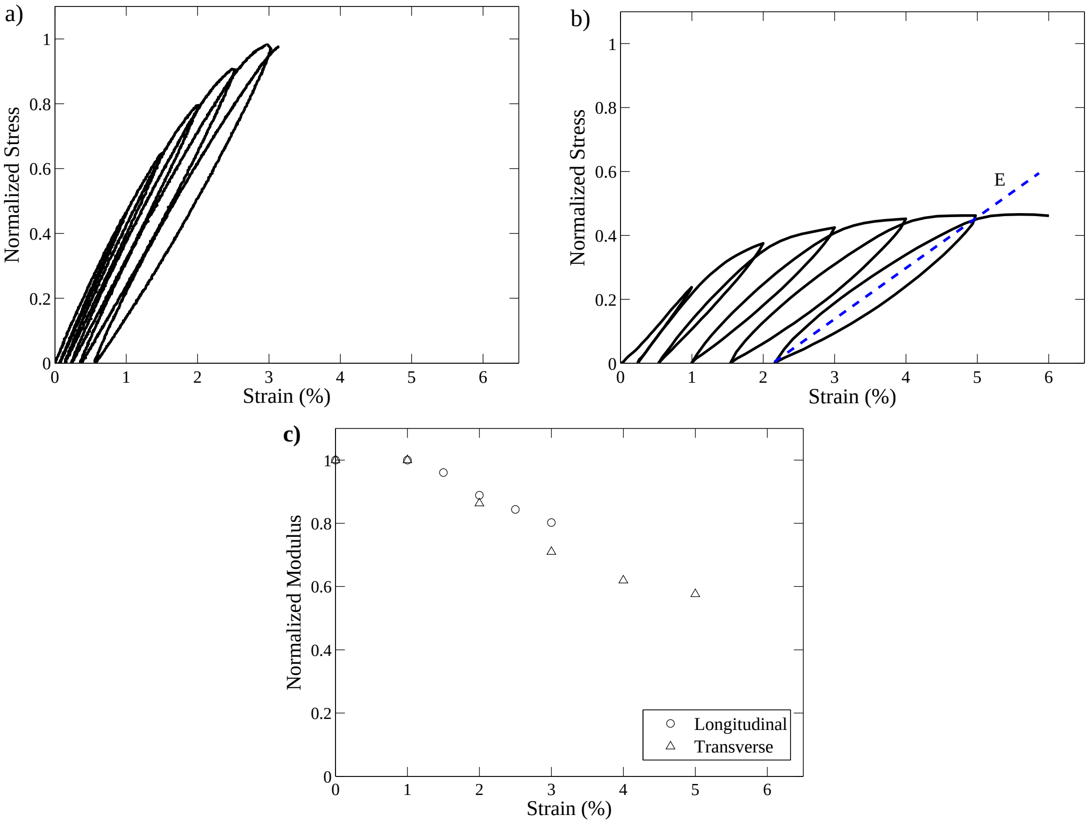

FIGURE 3.8: Stress-strain curves of a) longitudinal and b) transverse specimens, and c) the normalized modulus evolution during tensile tests with full load releases.

Tensile test with partial load releases In order to focus the investigation on the phenomena related to the damage and minimize the viscous properties of the composite, tensile test with partial load releases is commonly adopted as the experimental protocol [Nouri 2009b]. Tensile tests on dry as molded longitudinal and transverse specimens of PA66/GF30 were performed at room temperature and strain rate of 3×10^{-4} s^{-1}. Partial load releases were carried out at several strain levels. To avoid the viscous effects, the load releases were limited and the strain rate during load releases was ten times faster than the one during tensile loading or reloading. The results of this experiment can be seen in Fig. 3.9a. The tangential slopes during load releases were computed to obtain the modulus evolution during tensile loading. It can be seen from Fig. 3.9b that modulus reduction is observed in both longitudinal and transverse specimens. If the modulus reduction is compared with the results of the tensile tests with full load releases (Fig. 3.8c), it can be seen that the modulus reductions in tensile tests with partial load releases are around half than the ones in tensile tests with partial load releases. It can be inferred that the modulus reduction in tensile tests with partial load releases is dominantly due to the damage development.

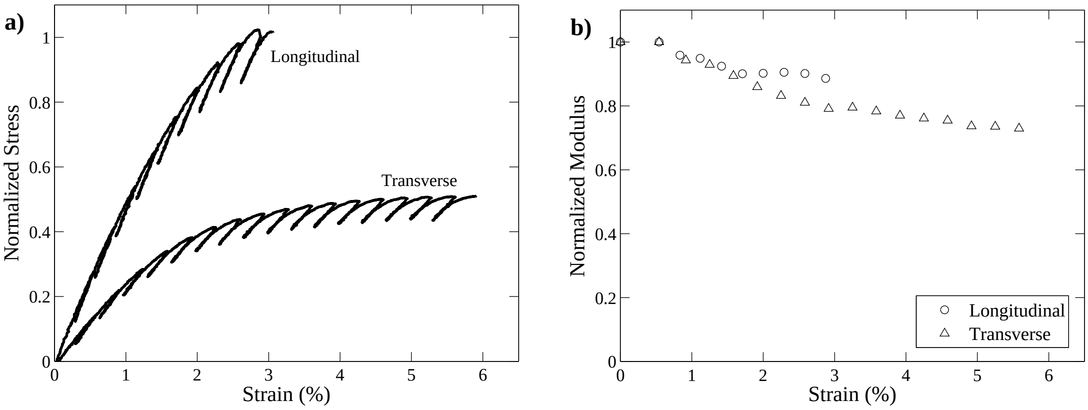

FIGURE 3.9: Stress-strain curve (a) and normalized modulus evolution (b) of longitudinal and transverse specimens during tensile tests with partial load releases.

3.1.8 Effect of relative humidity

One of the challenges of designing components made of short glass fiber reinforced polyamides arises from the ability of polyamide matrix to absorb water. The amount of absorbed water, depending on the environmental conditions such as temperature and relative humidity, highly influences the physical, thermal and mechanical properties of the composite. This is due to the water molecules that can interact with the amide groups in the amorphous phase of the polyamide matrix which consequently weaken the chain's bonds. Eventually, this can increase the chains mobility of the polyamide, or commonly called as plasticization effect. As shown in Table 2.3 of Chapter 2, the presence of water molecules inside the material reduces the yield stress and tensile modulus of PA66/GF30 while increases its strain to failure. Since the relative humidity highly impacts the mechanical properties, and possibly the damage mechanisms of PA66/GF30, the study will be extended in Chapter 4 by investigating the effect of relative humidity on the damage mechanisms of PA66/GF30.

3.2 Fatigue behavior and properties

Fatigue tests were performed on dry as molded PA66/GF30 by applying 3 Hz of sinusoidal wave under constant amplitude load controlled mode. The frequency of 3 Hz was chosen in order to avoid a global heat of the sample reaching the glass transition of dry PA66/GF30 ($\approx 65-70\ ^oC$) during fatigue loading. To prevent specimens from buckling, the tests were conducted under tension-tension mode, with a stress ratio of $R=\sigma_{min}/\sigma_{max}=0.1$. Continuous temperature monitoring of the active zone of the specimen was assured by the CEDIP Jade III MWR infrared camera.

3.2.1 Wohler curve

Fatigue life *(S–N)* curve of PA66/GF30 is reported in Fig. 3.10. In line with the results of quasi-static tensile tests, the fatigue strength of longitudinal specimens are about twice higher than that of transverse specimens. It is also shown that the *S–N* curves are linear in terms of maximum stress vs. number of cycles in a log-log representation. The current result is consistent with the previously published work in short glass fiber reinforced polyamides [Zhou 2006, Bernasconi 2007, De Monte 2010a]. It is worth noting that for the low stress levels of transverse specimens, the fatigue tests were stopped if the specimens did not reach final failure at 5×10^5 cycles. Stopping the fatigue tests at 5×10^5 cycles was a compromise that allow the tests to be performed in a reasonable time with significant evolution of the observable variables. However it does not mean that a fatigue endurance limit has been reached at those stress levels and that no damage occurs below the corresponding stress levels. According to the published works on fatigue behavior of short glass fiber reinforced polyamides, one cannot reach a distinctive endurance limit stress up to 10^6 cycles [Horst 1996, Mallick 2004, Zhou 2006], or even up to 10^7 cycles [Sonsino 2008, De Monte 2010a].

3.2.2 Strain rate during fatigue loading

The strain rate during fatigue loading can be estimated using the derivative of the strain equation. If one considers that the strain response of the composite follows a sinusoidal wave equation $\varepsilon(t)=\Delta\varepsilon\sin(\omega t)+\bar{\varepsilon}$, the strain rate will be $\dot{\varepsilon}(t)=\Delta\varepsilon\omega\cos(\omega t)$, where ε and $\dot{\varepsilon}$ are respectively the strain and strain rate (s^{-1}), $\Delta\varepsilon$ and $\bar{\varepsilon}$ are respectively the strain amplitude and mean strain, $\omega=2\pi/T$ is the angular frequency (rad/s), T is the period (s) and t is the time (s). The description of these variables is given in Fig. 3.11.

According to the above-mentioned strain rate equation, the composite experiences a continuous change of strain rate during cyclic loading. The maximum strain rate during a cycle is given by $\dot{\varepsilon}_{max}=\Delta\varepsilon\omega$. Evaluating only the maximum value, one can see from Fig. 3.12 that the strain rate in longitudinal and transverse specimens are ranging from 7×10^{-2} to 2×10^{-1} s^{-1} even though the maximum stress levels of both specimens are very different. The strain rates in all specimens are nearly constant during fatigue loading

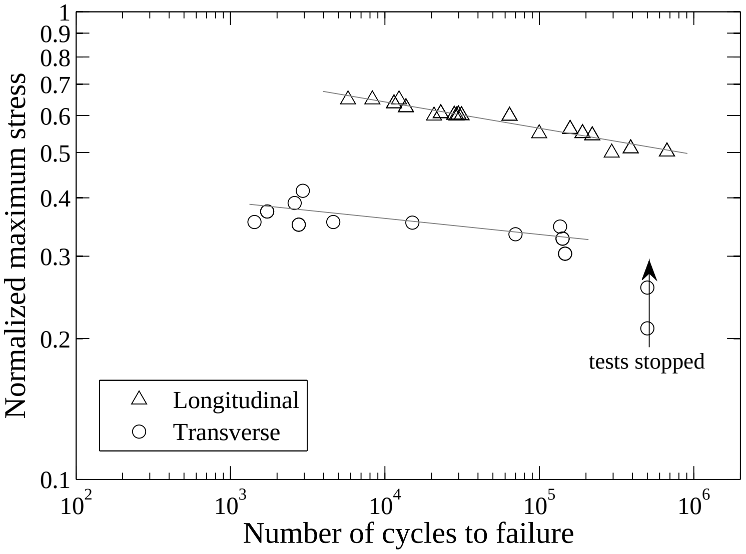

FIGURE 3.10: The *S–N* diagram of longitudinal and transverse specimens. Maximum stresses are normalized with the ultimate tensile strength of longitudinal specimen.

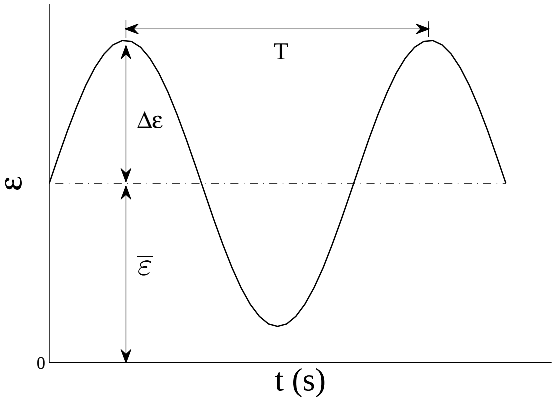

FIGURE 3.11: Schematic of sinusoidal wave form of strain response of material under fatigue loading.

except the one in the transverse specimen at the highest stress level, which could be due to the high heat generation and thus higher viscous properties of PA66/GF30. It has to be noted that the range of the strain rate in the fatigue test of PA66/GF30 is significantly higher than that in the quasi-static tensile test. Tensile tests performed at a strain rate of about 10^{-1} s^{-1} led to a fracture before reaching the ultimate stress commonly achieved in quasi-static strain rates.

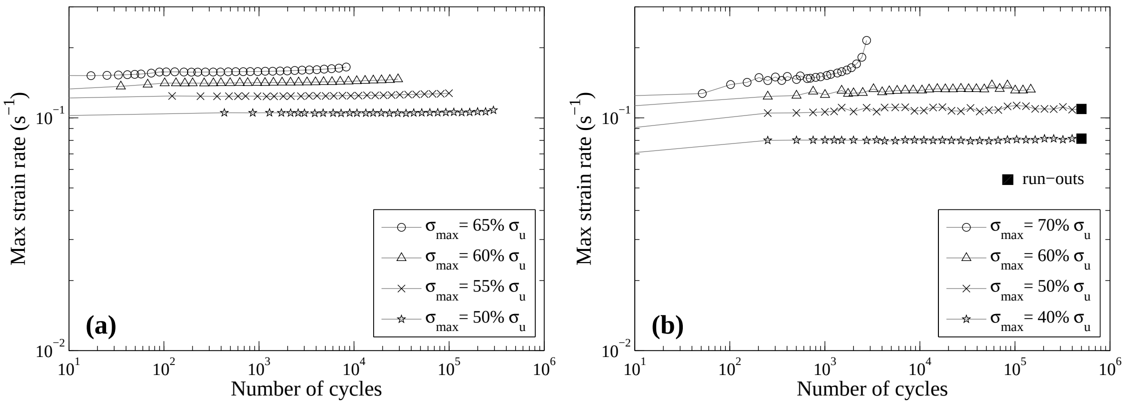

FIGURE 3.12: Evolution of maximum strain rate of (a) longitudinal and (b) transverse specimens during fatigue loading of PA66/GF30. (σ_u represents the ultimate tensile strength of its respective orientation angles)

3.2.3 Interrupted fatigue tests

Fatigue tests on dry as molded, longitudinal PA66/GF30 specimens have been carried out under frequency of 3 Hz, load controlled tension-tension mode, with a stress ratio of 0.1. During fatigue tests, interruptions have been conducted on several fatigue life percentages by releasing (unloading) the specimens up to zero force, maintaining 2 s for DIC image acquisitions and then reloading to continue the fatigue tests. The strain rate of unloading and reloading during interruptions was 3×10^{-4} s^{-1}. The experiment protocol of the interrupted fatigue test can be seen in Fig. 3.13. Since the DIC image acquisitions were performed onto the specimen's width and thickness surfaces, the volume change can be evaluated by computing $\delta V/V = \varepsilon_{11} + \varepsilon_{22} + \varepsilon_{33}$. The DIC image correlation was carried out during the zero force, referred correspondingly to the points $1, 2, 3\cdots$ of Fig. 3.13. The schematic response of the material during the interrupted fatigue test is shown in Fig. 3.14. In a load controlled tension-tension mode of PA66/GF30, creep effect can happen due to the viscous properties of the material or due to the damage. In fact, the DIC was carried out by correlating the residual strain during each interruption, corresponding respectively to the points $1, 2, 3\cdots$ of Fig. 3.14. By performing the image correlation at the zero force, a consistent comparison between different level of fatigue life can be achieved and thus the volume change during fatigue loading can be evaluated.

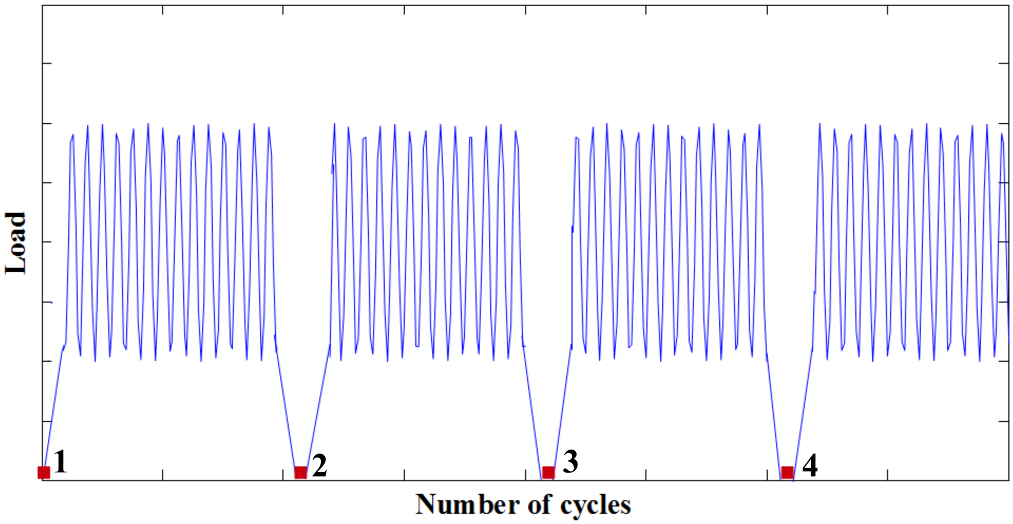

FIGURE 3.13: Experiment protocol of interrupted fatigue test.

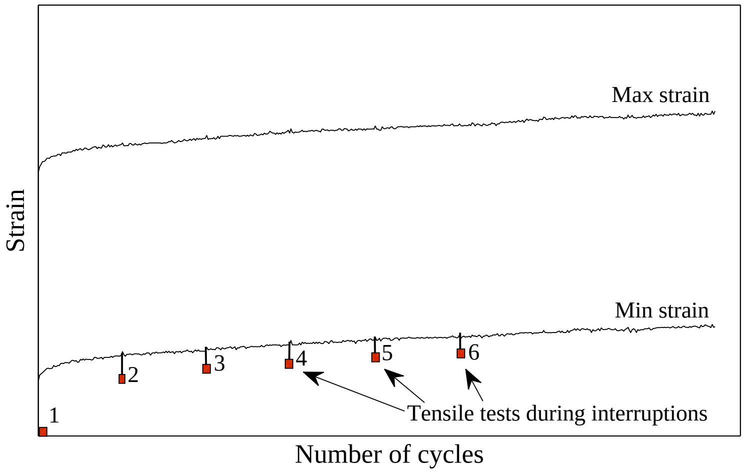

FIGURE 3.14: Schematic of material response during interrupted fatigue test.

The experimental results are shown in Fig. 3.15. It can be seen that volume changes during fatigue loading are observed. The specimens fatigue loaded at maximum stress level of $\sigma_{max} = 65\%\sigma_u$ exhibit higher volume changes than the one loaded at maximum stress level of $\sigma_{max} = 60\%\sigma_u$. The first increase of volume change could be dominantly due the (visco)elastic volume expansion. The void or damage could be developed during the 2nd region of the volume change where a steady change of volume is noticed. A volume change decrease is also observed. It remains difficult to explain this effect though early postulation states that it could be related to the increase of matrix crystallinity.

Despite the potentialities offered by this method, it possess challenges as the longitudinal specimen of PA66/GF30 exhibit low strain evolution during fatigue loading so that any micro deviations due to the experimental setup, such as misalignment and inhomogeneous clamping force of the sample, even in microscopic scale, would influence the strain field analysis.

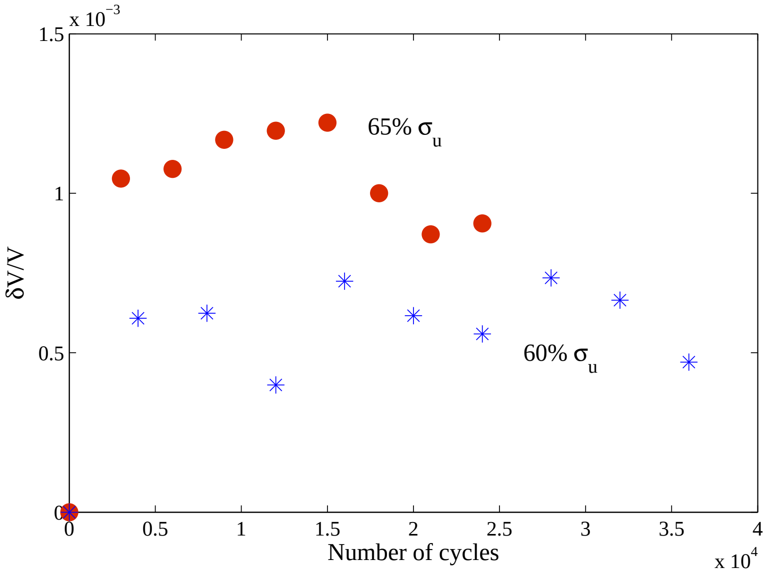

FIGURE 3.15: The volume change during fatigue loading of PA66/GF30.

3.3 Transition temperatures and viscoelastic behavior of polyamide-66

The dynamic mechanical analysis (DMA) data of dry as molded polyamide-66 matrix has been provided by Solvay Engineering Plastics. The data was collected from a temperature scan test of the polyamide-66 sample subjected to three-point bending mode with heating rate of 1 ^{o}C/min and 1 Hz of oscillation frequency.

By the DMA technique, the transition regime of the material, i.e. the region where the modulus decreases significantly, can be obtained. As shown in Fig. 3.16a, two transition regions as indicated by two damping maximums, are recorded. T_α and T_β are the temperatures at the maximum value of $\tan\delta$ in α-transition (at higher temperature) and β-transition (at lower temperature), respectively. The α-transition temperature is commonly known as the glass transition temperature, T_g. The T_g or T_α is associated to the gradual chain movements, whereas T_β is assigned to the side chain group movements of the polyamide-66.

Moreover, by DMA technique, the dynamic viscoelastic response of the material, namely complex modulus (E^*), elastic or storage modulus (E') and imaginary or loss

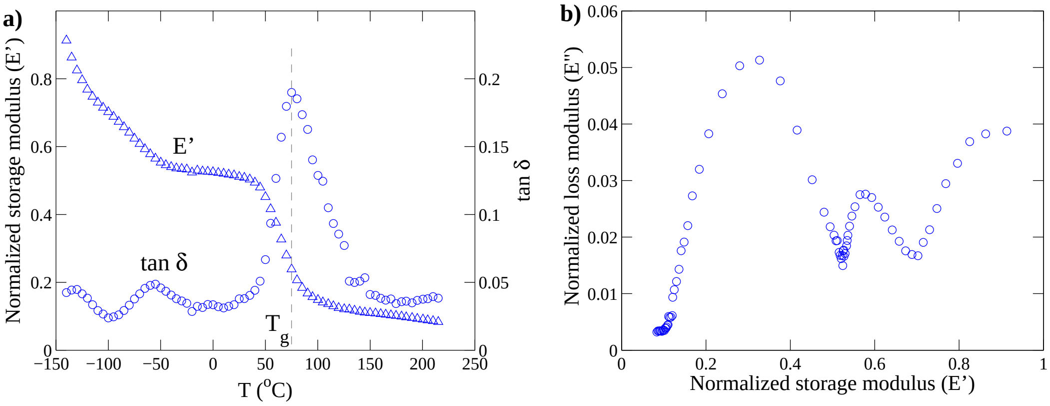

FIGURE 3.16: The temperature vs. storage modulus (a) and the Cole-Cole diagram (b) of dry as molded polyamide-66.

modulus (E'') can be evaluated from the material response to the sinusoidal oscillating load, as expressed in Eq. 3.1. The storage modulus E' is the measure of the sample's elastic behavior. The ratio of the loss to the storage is $\tan\delta$ and is often called as *damping*. It is a measure of the energy dissipation of a material. Plot of dynamic viscoelastic functions can be presented in a variety of forms, such as the plot of dynamic properties vs. frequency or dynamic properties vs. temperature (Fig. 3.16a). Also, one may plot the real (E') vs. imaginary part (E'') of the polymer response, or commonly called *Cole-Cole* diagram (Fig. 3.16b). Based on the DMA data, one can also conduct an optimization procedure to obtain material parameters of various viscoelastic functions. These functions can be described by the generalized Maxwell model, generalized Kelvin–Voigt model, generalized Zener model,$\cdots$. An example of works related to parameters identification and modeling of viscoelastic behavior of a polymer based on DMA data can be seen in [Szabo 2002, Alcoutlabi 2003].

$$\begin{aligned} E^* &= E' + E'' \\ \tan\delta &= E''/E' \end{aligned} \tag{3.1}$$

For humid conditions, the curve in Fig. 3.16a is shifted to the left due to the plasticization effect [Hassan 2011, Hassan 2012, Launay 2011, Launay 2013b]. Consequently, the T_g reduces to a value around or lower than the room temperature, depending on the relative humidity level. This will influence the mechanical properties of the polymer during service life. In case of reinforced polyamide, it will also influence the damage mechanisms. The effect of relative humidity on the damage mechanisms of PA66/GF30 will be discussed in Chapter 4.

3.4 Concluding remarks

The mechanical behavior and properties, as well as the general idea on damage behavior of PA66/GF30 have been discussed in this chapter. The stress-strain curves, the Wohler curve and the evolution of $\varepsilon_{11}, \varepsilon_{22}$ and ε_{33} in longitudinal and transverse specimens demonstrate the strong anisotropy effect induced by the injection molding process. It also shows that strain rate, temperature and relative humidity content highly influence the mechanical properties of PA66/GF30.

The polyamide-66 matrix and PA66/GF30 exhibit highly viscous behavior. During tensile and fatigue loading, this viscous behavior is coupled with the occurrence of damage. By the volume change and thermography techniques, it is difficult to separate the viscous and damage contributions. By the tensile test with full load releases, the hysteresis area increases while the hysteresis curve' slope decreases. This change of characteristic is due to the combination effect of the viscous behavior of the material and the occurring of damage.

The tensile test with partial load releases produces more reliable result related to the damage level as the viscous effect is suppressed in this test. However, since this is a phenomenological approach, the damage behavior of PA66/GF30 related to its initiation and accumulation needs to be investigated further. Therefore, the damage mechanisms in quasi-static monotonic loading of PA66/GF30, taking into account different relative humidity conditions will be further studied in Chapter. 4. Moreover, multiscale fatigue damage characterization of PA66/GF30 will be studied in Chapter. 5.

CHAPTER 4

In situ damage mechanisms investigation of PA66/GF30 under quasi-static monotonic loading: Effect of relative humidity

---

Contents

One of the issues of designing components made of polyamides reinforced with short glass fibers arises from the ability of polyamide matrix to absorb water. The water molecules interact with the polyamide matrix which leads to an increased mobility of the polymer chains. The amount of absorbed water, depending on the environmental conditions such as temperature and relative humidity, highly influences the physical, thermal and mechanical properties of the polyamide matrix and its composite.

Although the influence of environmental conditions (mainly the water uptake) on the physical and mechanical properties have been understood, no studies were analyzing the effect of relative humidity on the damage mechanisms and their effects on the overall mechanical behavior of the short glass fibers reinforced polyamides. Therefore, investigating the effects of relative humidity can be considered important since it can change the matrix and interfacial properties of the composite and accordingly it may influence their damage mechanisms.

In this chapter, damage mechanisms of injection molded polyamide-66/short glass fiber 30%wt composite (PA66/GF30) are analyzed using in situ SEM three-point bending tests on *longitudinal specimens* conditioned under three relative humidity contents (RH = 0%, 50% and 100%). The validity of these in situ analyses is confirmed by X-ray micro-computed tomography (μCT) observations on tensile loaded specimens.

For the sake of completeness of the damage analysis in PA66/GF30, the in situ test has been extended to study the microstructure effect. For this purpose, *the transverse and longitudinal specimens* are compared. Only specimens conditioned at RH = 50% are analyzed in this microstructure study. Moreover, the damage behavior of PA66/GF30 in the compressive zone of the three-point bending sample is also investigated.

For a comprehensive data analysis and discussion, literature review on water absorption behavior and damage characterization in reinforced polyamides are overviewed prior to analyzing the experimental results.

4.1 Review on water absorption behavior and damage characterization of reinforced polyamides

4.1.1 Water absorption of polyamides

In polyamide thermoplastics, the polar amide groups generate strong interactions in the crystalline and amorphous phases, with hydrogen bonds being established between neighboring molecules (Fig. 4.1). Despite their strong interactions, these hydrogen bonds exhibit a disadvantage as they can lead to water absorption (Fig. 4.2). In the amorphous phase, the water molecules can interact with the amide groups of the polyamides due to the less densely packed molecular chains compared to those in the crystalline phase. This will consequently weaken the preexisting inter-chain hydrogen bonds and thus increase the chains mobility of the polyamide. This physical process is commonly known as plasticization [Bergeret 2001, Carrascal 2005, Bergeret 2009].

Water absorption can be regarded as a diffusion process since the moisture content of the polyamide tends to reach an equilibrium state corresponding to the environmental conditions such as temperature and relative humidity. The effect of relative humidity on the equilibrium water absorption of different polyamides at room temperature, and the effect of environmental conditions on the moisture absorption rate of polyamide-66 can be seen in Figs. 4.3 and 4.4, respectively. In addition, the diffusion process involves water absorption from the specimen's surface towards the specimen's center. Therefore, prior reaching the equilibrium water absorption, water absorption distribution across the specimen's thickness is commonly observed (Fig. 4.5). It should be noted that the process of water absorption, as well as the corresponding change in macroscopic properties, is reversible as long as no hydrolysis or aging due to additional diffusion of oxygen takes place [Chanda 2007].

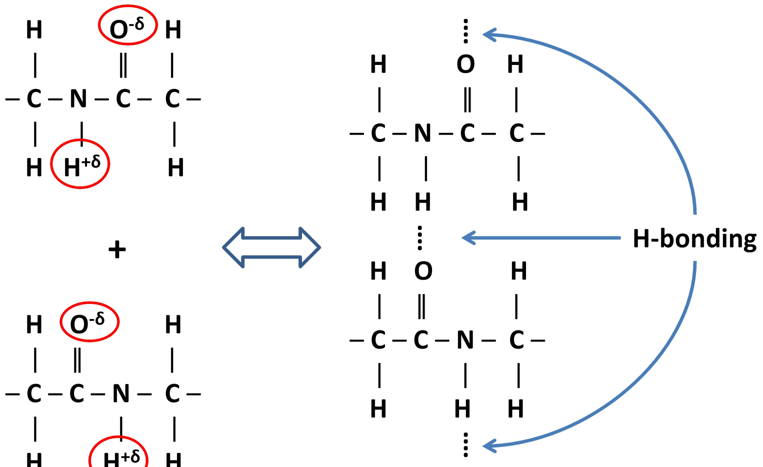

FIGURE 4.1: Hydrogen bonding between amide groups of the polyamides

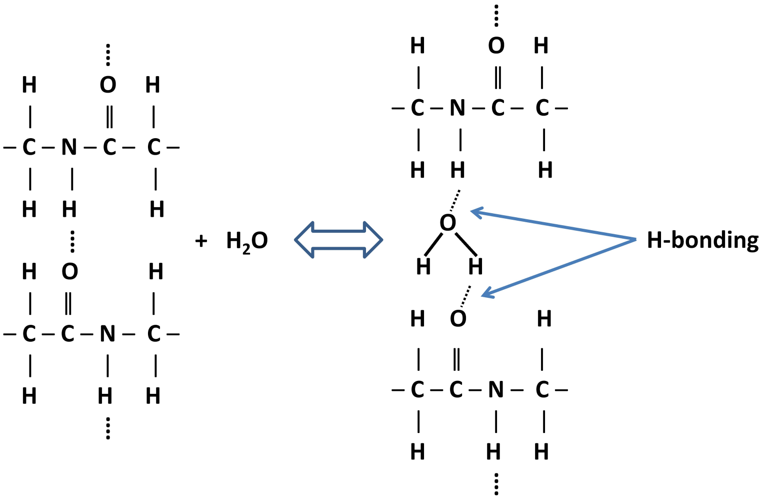

FIGURE 4.2: Water absorption in polyamides

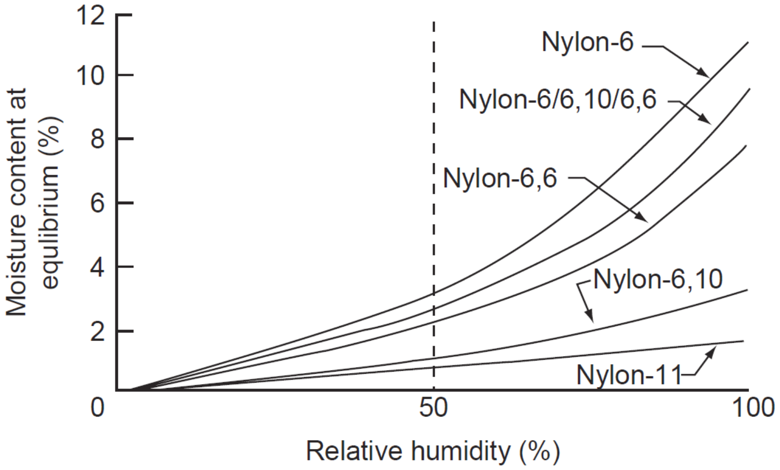

FIGURE 4.3: Effect of relative humidity on the equilibrium moisture absorption of various polyamides [Chanda 2007].

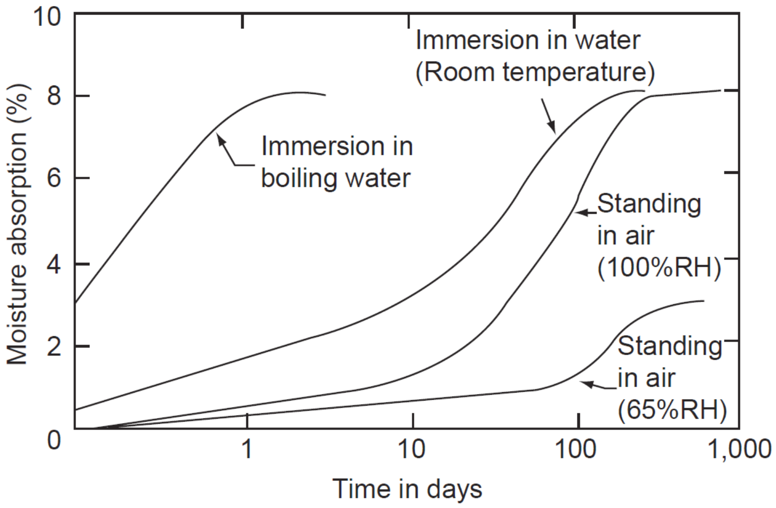

FIGURE 4.4: Effect of environmental conditions on the moisture absorption rate of polyamide-66 (3.175 mm specimen's thickness) [Chanda 2007].

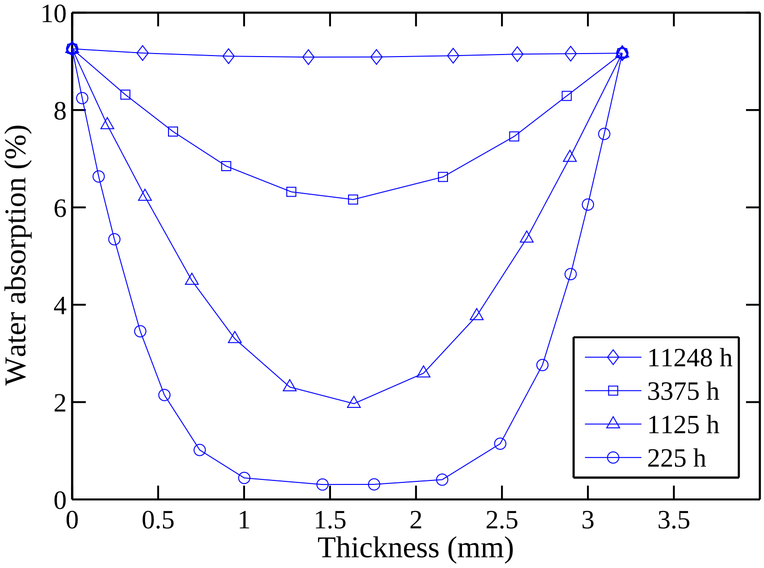

FIGURE 4.5: Through-thickness water absorption distribution over different exposure time of polyamide-66 at 23 ^{o}C, RH = 100%, adapted from the data of Solvay Engineering Plastics.

The plasticization highly impacts the mechanical properties of the polyamide. The water content results in a reduction of the strength and modulus while increasing the ductility, as shown in Fig. 4.6. Moreover, the presence of water molecules reduces the glass transition temperature T_g of the polyamide, as shown in Fig. 4.7 and Table 4.1. In the mean time, swelling effect can also occur since a certain amount of water is absorbed by the polyamide [Monson 2008].

RH (%)	T_g (°C)
0	65-70
25	50
50	18-26
68	8-17
80	0
100	0

Table 4.1: Influence of relative humidity (RH) on the glass transition temperature (T_g) of polyamide-66 (courtesy of Solvay Engineering Plastics).

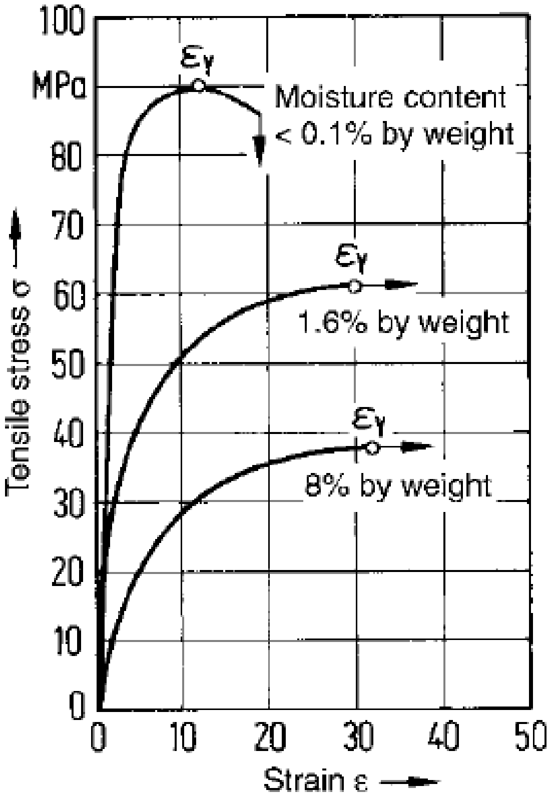

FIGURE 4.6: Stress-strain curves for polyamide-66 with variation of moisture content, evaluated at cross head speed of 50 mm/min, testing condition at 23 ^{o}C and RH = 50% [Erhard 2006].

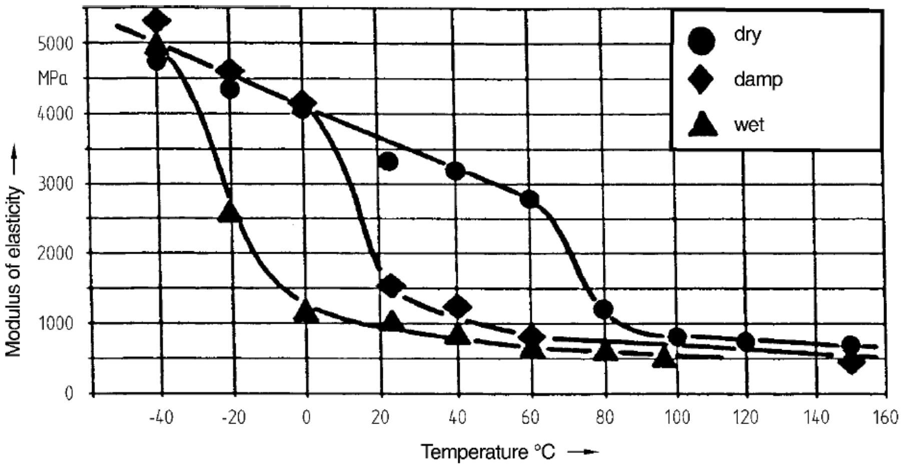

FIGURE 4.7: Elastic modulus vs. temperature for polyamide-66; The T_g is identified by the steep drop of the elastic modulus [Erhard 2006].

In its reinforced composites, such as in polyamides reinforced with short glass fibers, water content also reduces the mechanical properties (Fig. 4.8). Since glass fiber doesn't absorb water, for the same volume of the material, reinforcing polyamides with glass fibers bears advantages as it increases the mechanical properties while reduces the total amount of equilibrium water absorption of the material. As the environmental conditions mainly impacts the polyamide matrix, the incorporation of glass fibers in the polyamides doesn't significantly influence the T_g of the material [Hassan 2011]. In reinforced polyamides, the swelling effect of the polyamide matrix can induce a mismatched fiber/matrix volume expansion and thus creating a residual stress which in turn can reduce the fiber/matrix interfacial properties [Bradley 1995, Gautier 1999].

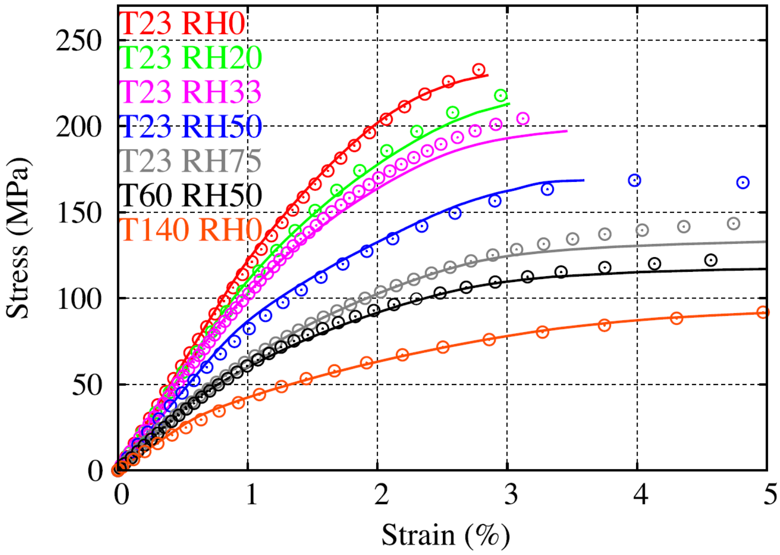

FIGURE 4.8: Effect of relative humidity and temperature on the stress-strain response of polyamides-66 reinforced with 35 wt% short glass fibers [Launay 2013b].

4.1.2 Damage characterization in reinforced polyamides

In situ SEM examination In situ damage investigation by scanning electron microscopy (SEM) has been favored by many researchers to study the damage in various composite materials due to its possibility to reveal the damage mechanisms and chronology [Lindhagen 1998, Schoß ig 2011, Bourmaud 2013]. In short glass fibers reinforced polyamide-66, the work on in situ damage mechanisms characterization under quasi-static monotonic loading were carried by Sato et al. [Sato 1991]. They proposed damage mechanisms scenario as presented in Fig. 4.9. They reported that the damage starts from fiber ends and further propagates along fiber/matrix interface. Afterwards, plastic deformation band occurs in the matrix followed by crack opening and slow crack propagation, leading to a ductile fracture mode. Finally, when the crack grows to a critical size, a fast crack propagation occurs through the composites in a brittle manner.

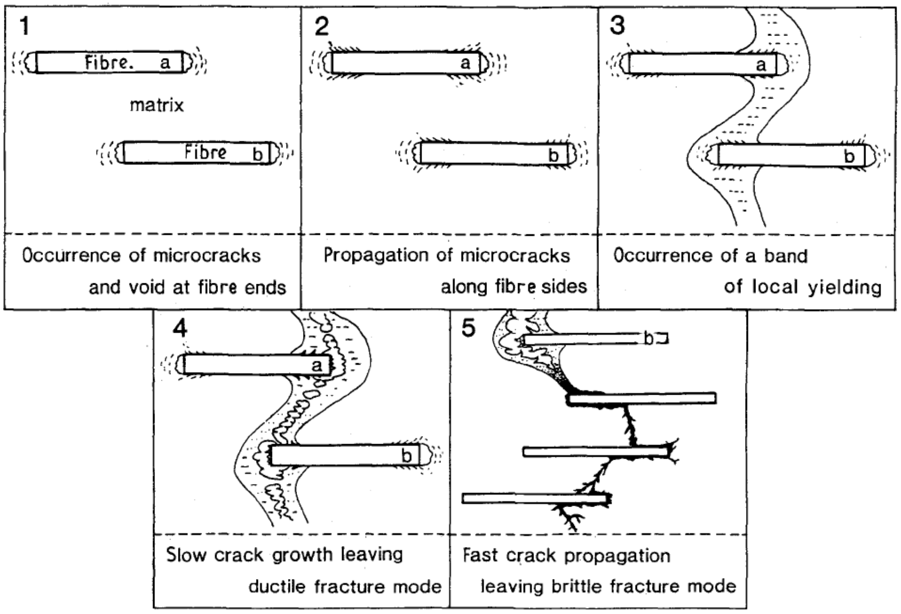

FIGURE 4.9: Damage mechanisms scenario of short glass fibers reinforced polyamide-66 proposed by Sato et al. [Sato 1991].

Acoustic Emission technique Damage investigation by acoustic emission technique has been employed by many researchers to evaluate the damage mechanisms in various types of composites [Barré 1994, Bohse 2000, Meraghni 2002, Ramirez-Jimenez 2004]. In short glass fibers reinforced polyamide-66, acoustic emission technique has been used by Mouhmid et al. [Mouhmid 2006] to investigate different mechanisms of damage. They reported that the global damage mechanisms of the material can be characterized based on the number of acoustic emission events and it is possible to correlate each range of amplitude to a certain damage mechanism type. They proposed three main damage process stages of the composite as follows:

i. An elastic zone with an insignificant acoustic activity.
ii. A nonlinear behavior controlled by matrix plasticity and microcracks.
iii. A significant damage represented by consequent acoustic emission activity followed by final failure.

SEM fractography Post-mortem SEM investigation on fracture surface of composites has also been used to investigate the final stage of failure mechanisms. Sato et al. analyzed the fracture surface of polyamide-66 reinforced with short glass fibers by SEM [Sato 1991]. It was observed that the fiber surface is covered by a thin film of the matrix, which indicates that a cohesive type of failure is favored in this composite.

Zhou and Mallick [Zhou 2005] employed SEM analysis on the fracture surface of short glass fibers reinforced polyamide-66. They observed that, according to the surface appearance of the polyamide matrix, the composite is fractured in ductile mode at the normal zone and in brittle mode at the weldline zone. In the normal zone, a thin film of matrix material adheres to the pulled-out fibers, indicating a good fiber/matrix interfacial properties, which confirms the work of Sato et al. [Sato 1991]. In the weldline zone, the fiber surfaces do not have much matrix material adhering to them, which indicate an inferior fiber/matrix interfacial properties compared with that in the normal zone.

Mouhmid et al. [Mouhmid 2006] applied SEM analysis on the fracture surface of neat and short glass fibers reinforced polyamide-66. From their study, fiber fracture, matrix microcracks and interfacial debonding are frequently observed.

Hassan et al. [Hassan 2011] reported that the absorbed moisture in short glass fibers reinforced polyamide-66 significantly changed the fracture mode of the composite from brittle (for dry specimen) to ductile fracture (for wet specimen).

Crack growth Gunzel et al. [Günzel 2012] studied the grack growth behavior of injection molded polyamide-6 reinforced with 30 wt% short glass fibers considering several effects as follows:

- matrix type: black and natural colored polyamide-6 matrix
- fiber orientation: specimens extracted longitudinally and transversely with respect to the mold flow direction (MFD)
- moisture content: dry and conditioned (equilibrium water content at T = 23 ^{o}C, RH = 50%)

In terms of mechanical properties, it was reported that the composite exhibits higher stiffness and strength when the load is applied parallel to the global fiber direction, while the strain at break does not depend on the fiber orientation. The moisture content reduces the strength and stiffness while increases the plasticity. Regarding the matrix type, the strength of composite with naturally colored matrix is around 5% higher compared to the black configurations while no effect observed on the stiffness and strain at break.

The tension-tension fatigue crack growth experiments were done according to ISO 15850. The analysis involves the evaluation of the stress-intensity factor $K_I = \sigma\sqrt{\pi a}Y(a/W)$ under mode I loading and the stable crack propagation behavior following the Paris model $(dA/dN) = C_p(\Delta K_I)^{m_p}$. The K_I analysis considers the nominal stress σ, the crack length a and the geometry function, while the Paris model evaluation involves two material's parameters C_P and m_p.

They reported that, as shown in Fig. 4.10, the resistance to crack propagation increases when more fibers are oriented perpendicular to the propagation direction. A comparison between dry and conditioned materials leads to a high crack propagation resistance for dry configurations. In contrast, a variation of the matrix material leads to an increased crack growth resistance for the black matrix material. The impact due to moisture is around half of the effect due to fiber orientation. The variation of the studied variables shifts the crack growth behavior to different stress-intensity ranges without influencing the Paris slope.

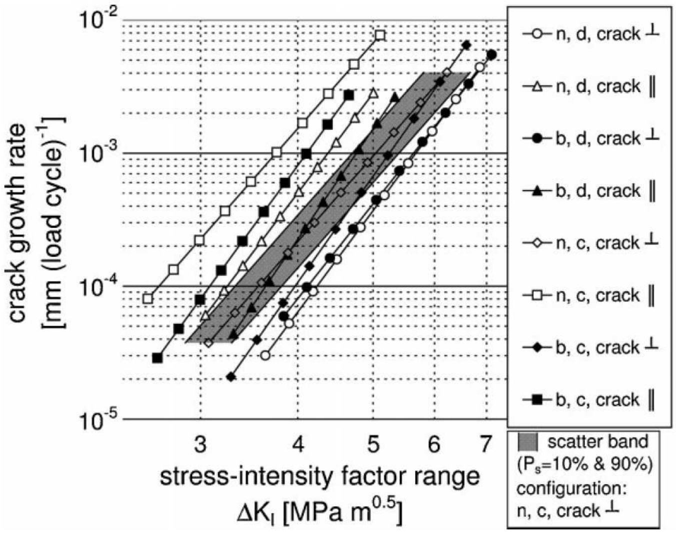

FIGURE 4.10: Stable crack growth behavior of reinforced polyamide (solid symbols–matrix black (b), hollow symbols–matrix natural (n); circles–matrix dry (d) and fibers ⊥ to crack, triangles–matrix dry and fibers || to crack, diamonds–matrix conditioned (c) and fibers ⊥ to crack, squares–matrix conditioned and fibers || to crack) [Günzel 2012].

They also reported that the fracture surfaces exhibit uniform characteristics, which do not depend on global fiber orientation, moisture content or matrix type. In the area of stable crack growth, matrix is deformed in microductile mode and pulled out fibers are free of matrix. In contrast, in the residual fracture surfaces (the final failure areas), matrix fractures in microbrittle mode and pulled out fibers are covered with a thin matrix layer. The changing of mechanisms between both zones happens suddenly. This transition infers that the final failure is due to macrocracks. An example of the fracture surfaces' configuration can be seen in Fig. 4.11.

Microtomography technique Besides its capability to study the microstructure, as previously discussed in Section 2.6, the X-ray micro-computed tomography (μCT) technique was also proved to be effective to characterize the damage mechanisms in various materials. Numerous damage studies have been dedicated to laminate composites [Schilling 2005, Moffat 2008, Wright 2010, Sket 2012, Lambert 2012, Hufenbach 2012, Scott 2012, Fidan 2012, McCombe 2012, Little 2012]. The μCT has also been employed to study the damage in metal matrix composites [Buffière 1999, Maire 2001a, Babout 2001], carbon fiber composites [Awaja 2011, Bull 2013], woven composite [Seltzer 2013], stitched composite [Tan 2011], SiC/SiC minicomposite [Chateau 2011] and natural fiber composites [Rask 2012].

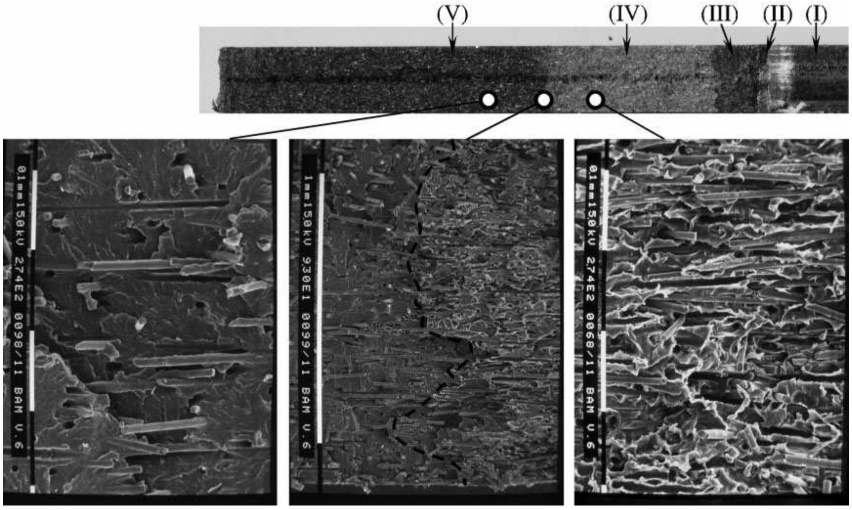

FIGURE 4.11: Fracture surfaces of dry, black matrix composite with crack || to fibers; Milled notch (I), fine notch (II), fatigue notch (III), stable crack growth (IV) and residual fracture surface (V). [Günzel 2012].

For the damage analysis in short fiber reinforced thermoplastics, the work of Jegou [Jegou 2012] and Cosmi and Bernasconi [Cosmi 2013] on fatigue damage investigation of these composites can be found in open literature. These two works will be reviewed in the next chapter dedicated to characterize the fatigue damage behavior in PA66/GF30. In addition, the μCT technique for damage investigation in PA66/GF30 has also been employed in our recently published works [Arif 2014a, Arif 2014b]. The contents the two publications are covered in the current manuscript.

4.2 Preparation of specimens

Specimens for in situ characterization were machined in longitudinal and transverse directions to the MFD from the rectangular plate produced by injection molding, defined hereafter as *the longitudinal and transverse specimens*, respectively. The specimen's description and the testing device can be seen in Fig. 4.12. The specimens were 45 mm long with 10 mm width and a thickness of 3.2 mm. The conditioning of the specimens have led to equilibrium moisture content corresponding to three different relative humidity conditions, i.e. RH = 0%, 50% and 100%.

RH = 0% specimen The sample conditioned under RH = 0% was first polished then conditioned under vacuum oven at 80 ^{o}C for 15 *h* to repel the water and ensure zero moisture content in the whole sample. Afterwards, the specimen was sputtered with a thin layer of gold prior to in situ SEM testing and observations. It is noted that the polishing procedure was carried out in wet environment an thus the specimen, especially in the surface, can absorb the water moisture. The vacuum process at sufficiently high temperature and adequate time can repel back the water from the specimen's surface.

RH = 50% specimen The RH = 50% specimen was first polished and then prepared according to ISO 1110 standard, as the specimen has been conditioned inside a weathering chamber at 70 ^{o}C and RH = 62% until a constant weight was obtained. The procedure was continued by one week specimen conditioning at 23 ^{o}C, RH = 50% to make homogeneous and equilibrium water concentrations in the whole sample. The specimen was then sputtered with a thin layer of gold prior to in situ SEM testing and observations.

RH = 100% specimen The specimen with RH = 100% was obtained by immersing the sample in boiling water for 35 *h*, followed by sample polishing and then water immersion at room temperature for one week. Subsequently, the specimen was sputtered with a thin layer of gold prior to in situ SEM testing and observations.

It is worth noting that the plasticization process governed by the water uptake of the polyamide is a reversible process. The water content of the sample can be thus reduced or increased depending on the RH condition. Therefore, ensuring the material to reach equilibrium water content according to the designated relative humidity condition is important.

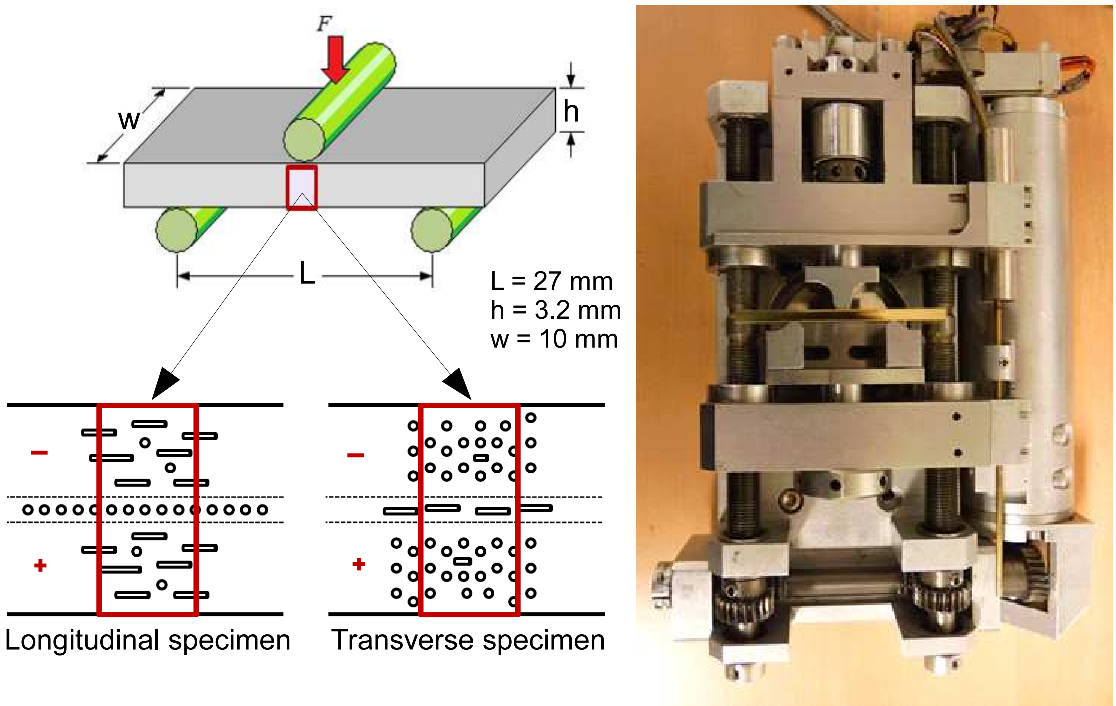

FIGURE 4.12: The in situ SEM experimental setup and the micro-machine testing device.

4.3 Microscopic damage characterization

4.3.1 In situ SEM bending tests

In situ observations were performed by subjecting the specimens into a flexural load using a three-point bending micro-machine (Fig. 4.12), with a span length of 27 mm, positioned inside a large SEM chamber (JEOL JSM-7001F). The crosshead speed of the contact central-point was set up to 400 μm/min. The displacement of the crosshead speed was interrupted in fixed positions to allow the in situ observation and images acquisition. To reduce the relaxation effect in the material, the observation time while maintaining the load was limited to 3 minutes. The observation area corresponded to the thickness surface of the composite with a particular emphasize at the outermost tensile region of the specimen, notably at the shell layer of the specimen. The three-point bending loading condition leads to a maximum stress at the outermost tensile region, which has an advantage to narrow down the observation to the zone where the maximum damage can be expected.

It must be emphasized that since the main objective of the current work is to focus on the damage mechanisms investigation, the in situ SEM observations carried out at very local and high magnification are hence required. Therefore, local fiber configurations such as fibers close to each other, fiber orientation perpendicular and transverse to the macroscopic stress direction were frequently observed regardless to the fact that the in situ observations were mainly performed on the shell layer where average fiber orientation is parallel *(for the longitudinal specimen)* and perpendicular *(for the transverse specimen)* to the macroscopic stress direction.

4.3.2 Micro-computed tomography observations

For a confirmation purpose of the in situ SEM observations, damage investigation by post-mortem μCT technique was carried out. The confirmation by μCT is important as the observed damage mechanisms by SEM are based on surface phenomena. The μCT technique offers a better damage investigation method as it can reveal the damage occurrence in the whole volume of the specimen. However, since the μCT image (voxel) resolution is lower than that of the SEM, the damage dimension is usually must be higher than the μCT image resolution in order to allow damage visualization by μCT. Therefore, the results of the two associated independent observation techniques would complement each other for a better understanding of the damage mechanisms in PA66/GF30.

For this confirmation work, the μCT technique was employed to investigate the damage mechanisms of PA66/GF30 specimens conditioned at RH = 0% and 50% that have been subjected to tensile loading. Dog-bone tensile specimens were machined in longitudinal direction to the MFD from the PA66/GF30 rectangular plate. The μCT experiment on virgin non-tested sample with RH = 0% was also carried out as a reference. The μCT experiments were performed at beam line ID19 of European Synchrotron Radiation

Facility (ESRF) in Grenoble, France [ID19 ESRF]. The voxel resolutions achieved by the ID19 system were 0.7 and 1.4 μm. Both resolutions provided qualitatively relevant physical information. The μCT experiments were performed on samples with the size of $2 \times 2 \times 3.2$ mm^3. The tensile loaded μCT samples were extracted from the specimens that have been tensile loaded up to failure. The cutting locations of the tensile loaded samples were far from the fracture surface in order to avoid fast crack propagation effect due to the final failure. It is expected that ultimate damage mechanisms can be found at this maximum load.

4.4 Effect of relative humidity on the damage mechanisms of PA66/GF30

In this section, the effects of relative humidity on the overall mechanical properties and damage mechanisms in *longitudinal specimen* of PA66/GF30 are presented.

4.4.1 Overall mechanical properties

Fig. 4.13 shows the normalized load vs. displacement responses of the in situ SEM three-point bending tests of longitudinal specimens conditioned at various RH conditions. For each specimen, the relative ultimate loads before failure were recorded. Flexural strength (σ_f) was defined, for each RH content, as the maximum flexural stress in the specimen at the ultimate load according to ISO 178 standard. Relative flexural stress was defined to be the ratio of flexural stress in the area of observation with respect to the flexural strength.

As described in Fig. 4.13, the RH content highly influences the mechanical properties of PA66/GF30. Flexural strength and stiffness of PA66/GF30 decreases with the increase of RH. The noticeable differences on the strength and modulus of PA66/GF30 by variation of RH are assumed to be due to the damage and plasticization effect. Indeed, the RH = 0%, 50% and 100% specimens represent the conditions where the composites are respectively in glassy ($T_g > T_{room}$), glass transition ($T_g \approx T_{room}$) and rubbery states ($T_g < T_{room}$) [Hassan 2011, Launay 2013b]. Strain to failure in RH = 50% and 100% specimens are higher than that in RH = 0% specimen, whereas no significant difference is observed between the strain to failure at RH = 50% and 100% specimens. The current observation has been confirmed by Akay [Akay 1994] and the internal data of Solvay Engineering Plastics which show that the RH condition has no strong effect on the strain to failure of the reinforced polyamide-66 composite. The increase of strain to failure as the RH content increases is only noticeable for pure polyamide-66.

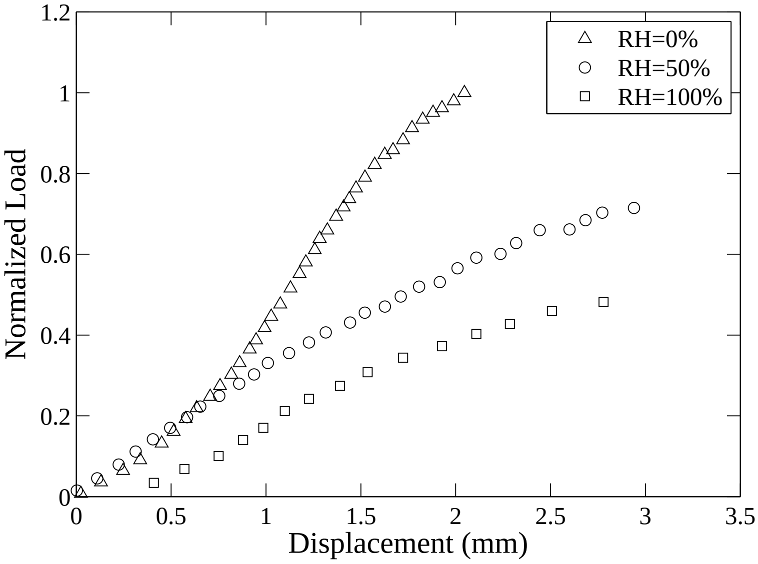

FIGURE 4.13: Normalized load vs. displacement curve of PA66/GF30 longitudinal specimens with variation of relative humidity.

4.4.2 Experimental results on relative humidity effects

4.4.2.1 SEM observations and analysis

Fig. 4.14 shows typical microstructure observed on the thickness surface specimen before applying any load. For the three studied RH conditions (RH = 0%, 50% and 100%), the local views, corresponding respectively to Figs. 4.14a, b and c confirm that no indication of initial damage is observed regardless of the RH conditions.

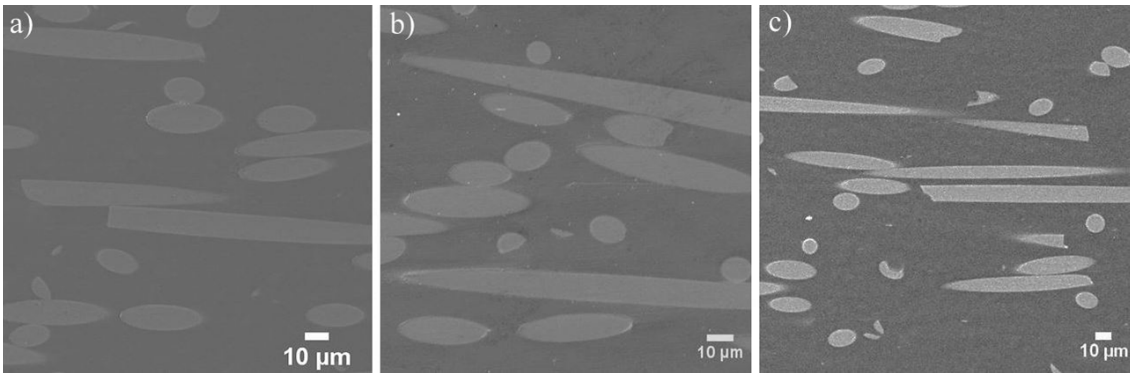

FIGURE 4.14: Local views of virgin surface (at zero level stress) of longitudinal PA66/GF30 specimen for the three RH contents: a) RH = 0%, b) RH = 50% and c) RH = 100%. One can notice that no indication of initial damage is detected regardless of the RH conditions.

RH = 0% specimen The damage on RH = 0% specimen starts to be noticeable at around 33% σ_f. Damage initiations in the form of interfacial debonding at fiber end and fiber breakages are observed (Fig. 4.15a). Also, it can be noticed in Fig. 4.15b that the local matrix deformation at location where fibers are close to each other is larger than the one at the rest zones of matrix. It is assumed that the damage has high possibility to initiate from this location due to the local stress concentration generation. As the load increases, damage propagation along fiber/matrix interface (Fig. 4.15c) and fiber breakages at new locations are observed. At high relative flexural stress (95% σ_f), matrix microcracks occur at location where broken fibers are close to each other (Fig. 4.25a).

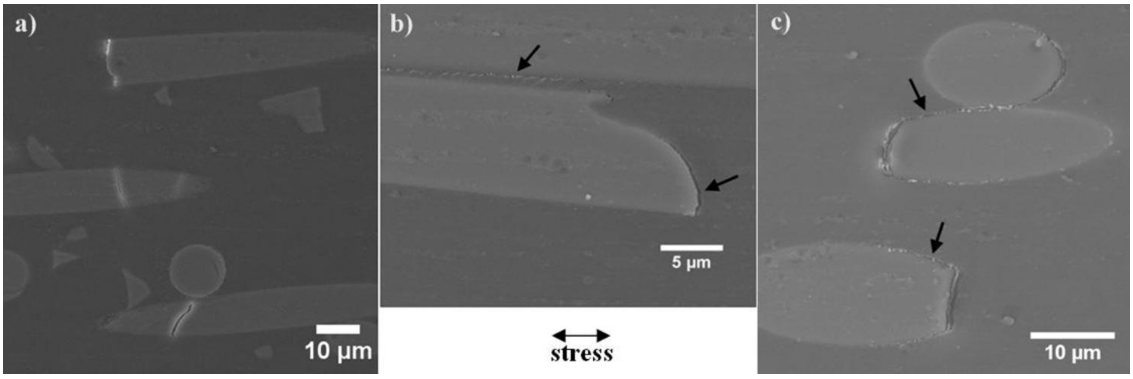

FIGURE 4.15: PA66/GF30, RH = 0% longitudinal specimen, a) damage at fiber end and fiber breakages at 33% σ_f, b) damage at fiber end and high plastic deformation between two adjacent fibers at 48% σ_f, and c) damage propagation along fiber/matrix interface at 85% σ_f.

RH = 50% specimen Fig. 4.16a shows the surface of the specimen conditioned at RH = 50% subjected to a 30% σ_f. It can be seen that the damage is initiated in the form of interfacial debonding. However, it must be noticed that this damage initiation is not only observed at fiber ends but also at many locations where fibers are close to each other. The damage then propagates along the fiber/matrix interface, occurring both through the in-plane and out-of-plane directions, as shown in Fig. 4.16b. Some fiber breakages are evidenced at high relative flexural stress. However these fiber breakages are statistically small and hence cannot be considered predominant in terms of damage level. At high relative flexural stress (98% σ_f), matrix microcracks are observed (Figs. 4.16, 4.17, 4.18 and 4.25b). In addition, locally strained zone around fiber and cohesive fiber/matrix interface debonding are also evidenced, as shown in Figs. 4.17, 4.18.

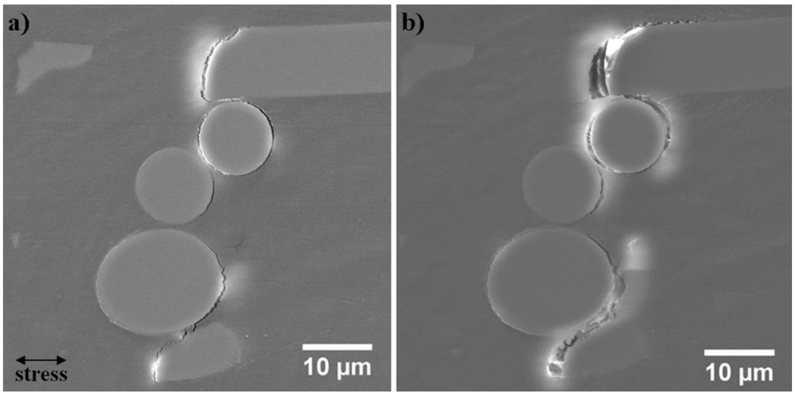

FIGURE 4.16: PA66/GF30, RH = 50% longitudinal specimen, a) damage initiation at 30% σ_f, b) damage propagation at 83% σ_f.

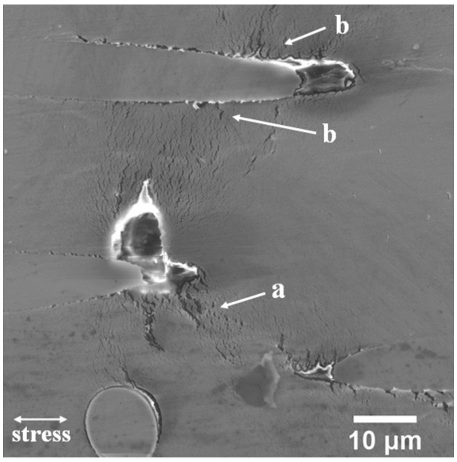

FIGURE 4.17: PA66/GF30, RH = 50% longitudinal specimen at 98% σ_f, a) matrix microcracks and b) locally strained zones around fiber.

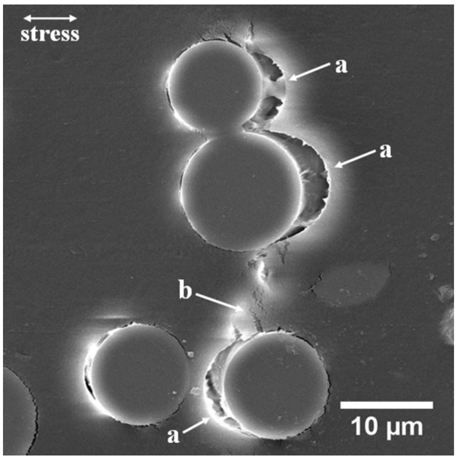

FIGURE 4.18: PA66/GF30, RH = 50% longitudinal specimen at 98% σ_f, a) fiber/matrix interface debonding and b) matrix microcracks. The local view shows that fibers are oriented transversely to the applied load direction.

RH = 100% specimen Likewise to the RH = 50% specimen, the damage in RH = 100% specimen initiates at around 30% σ_f by fiber/matrix debonding at fiber ends and at locations where fibers are close to each other. Afterwards, the debonding propagates along the fiber/matrix interface. At high relative flexural stress, some fiber breakages are noticed. However, these fiber breakages cannot be considered predominant in terms of damage level as the number is statistically small. Matrix deformation bands and debonded fiber/matrix interfaces accompanied with locally strained zone around the fibers are also frequently observed at high relative flexural stress (98% σ_f), as shown in Figs. 4.19, 4.20 and 4.25c. Matrix deformation band is the zone where local matrix deformation is high. Compared to RH = 50% specimen, the RH = 100% specimen possesses significantly higher number of damaged area and higher occurrence of matrix microcracks and matrix deformation bands (Fig. 4.25c).

The sequential images of the RH = 100% specimen from its initial state to the stress level right before the final failure which describes completely the whole chronology of damage mechanisms in RH = 100% specimen can be seen in Fig. 4.21.

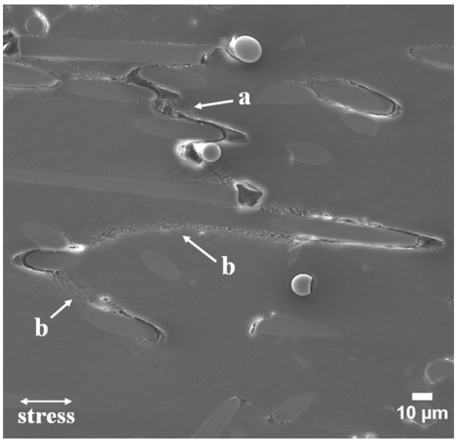

FIGURE 4.19: PA66/GF30, RH = 100% longitudinal specimen at 98% σ_f, a) matrix microcracks and b) matrix deformation band.

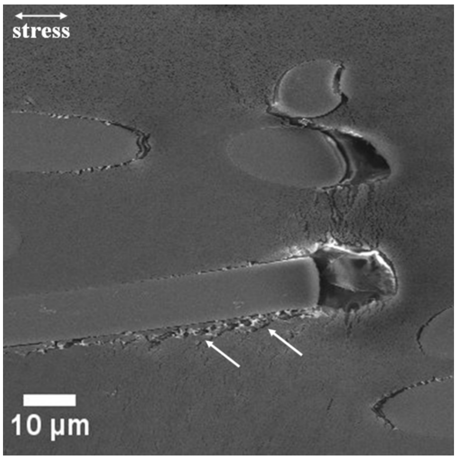

FIGURE 4.20: Locally strained zone around fiber of PA66/GF30, RH = 100% longitudinal specimen at 98% σ_f (indicated by arrow lines).

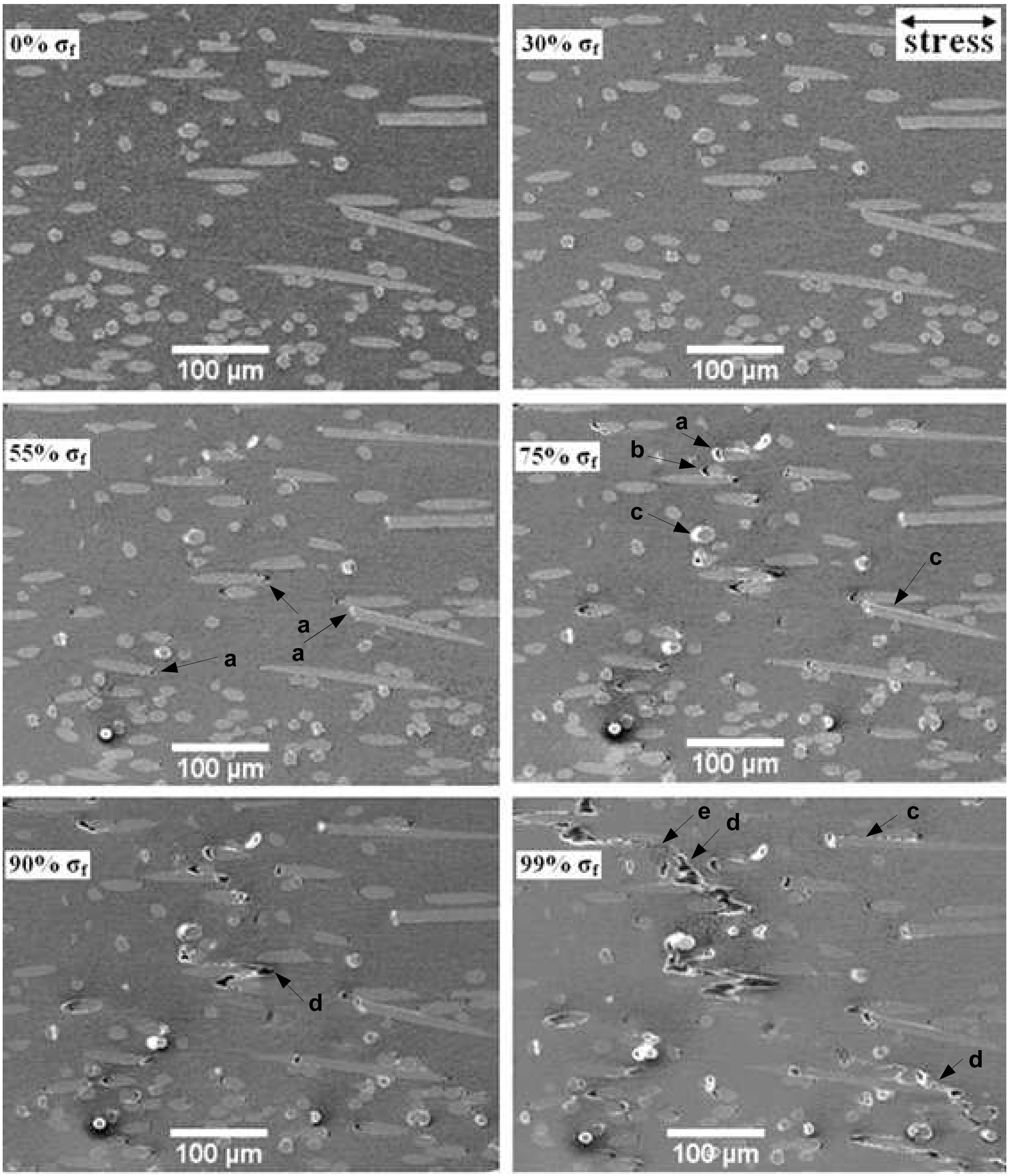

FIGURE 4.21: SEM image sequences representing damage evolution of PA66/GF30, RH = 100% longitudinal specimen from the virgin state to the stage prior to failure. The arrow lines indicate the following damage mechanisms; a) void at fiber end, b) void at location where fibers close to each other, c) fiber/matrix interfacial debonding, d) matrix microcrack and e) plastic deformation band.

4.4.2.2 Micro-computed tomography investigation and analysis of damage mechanisms

Damage mechanisms in PA66/GF30 composite with RH = 0% and 50% were assessed by μCT technique. The specimens were subjected to a tensile loading, which possesses the same loading as the outermost tensile region of the specimen under three-point bending load. As mentioned in section 4.3.2, the μCT investigations were performed on samples extracted from the specimens that have been tensile loaded up to failure. These samples were extracted far from the fracture surface in order to focus the investigation in a damaged region and to avoid considering the localized failure zone.

As shown in Figs. 4.22 and 4.23 obtained by μCT investigation of RH = 0% and 50% specimens, debonding at fiber ends and fiber sides, matrix microcracks and fiber breakages are observed. These findings confirm and strengthen the observations of in situ SEM test. The noticeable difference between RH = 0% and 50% specimens consists in the occurring of matrix microcracks. Indeed, while for RH = 0% specimen, the matrix microcracks exhibit brittle propagation, the ones in RH = 50% coalesce in ductile way. The damage mechanisms found in the bulk material therefore correspond to the in situ SEM observations of the surface. This comparison confirms the validity of the in situ SEM observation technique described in this work to identify damage mechanisms. The μCT observations at RH = 0% and 50% specimens are therefore considered sufficiently representative to complement the in situ SEM tests to investigate the damage mechanisms in dry and humid conditions.

For a purpose of qualitative comparison of these investigations with those on a virgin sample (non-tested), μCT observations have been performed on a non-tested sample extracted from an injected plate (as received). Fig. 4.24 performed at a resolution of 0.7 μm does not show any noticeable damage for this non-tested sample. It confirms thus that the damage mechanisms evidenced on samples extracted from specimens loaded up to failure (Figs. 4.22 and 4.23) are induced by the applied stress. Consequently, they cannot be ascribed to a degradation induced by the injection process, to that induced by the machining during the μCT samples preparation and to that induced by the μCT artifacts.

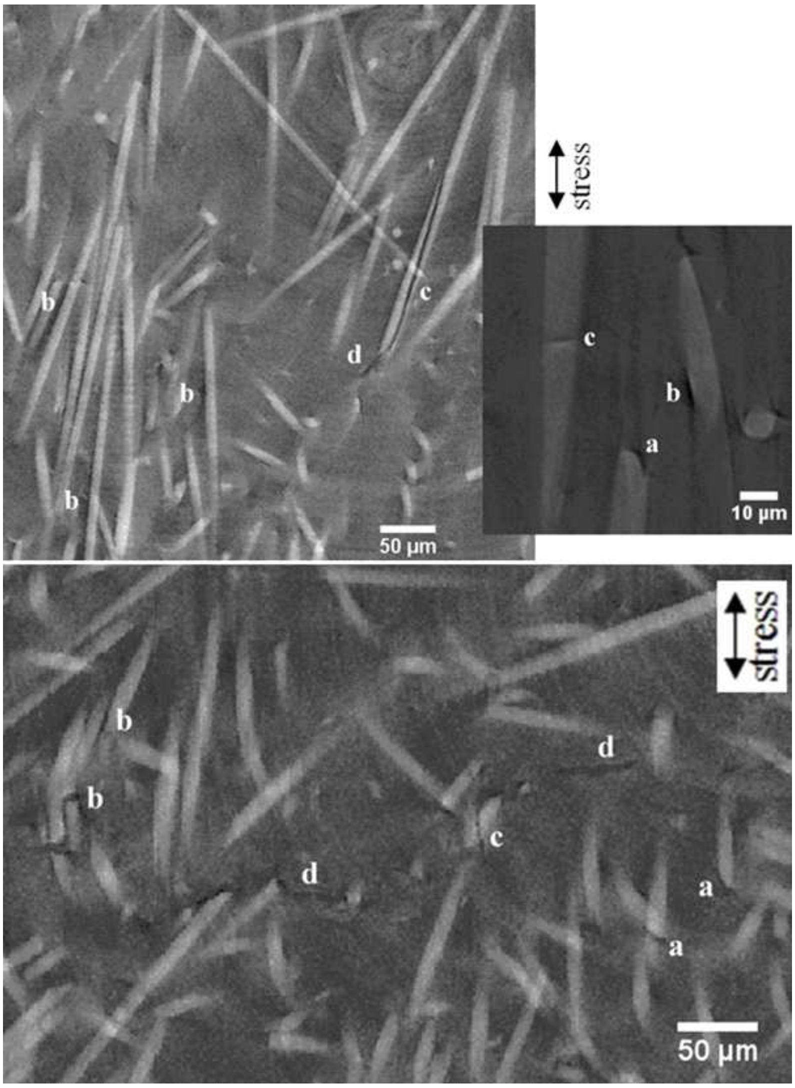

FIGURE 4.22: Damage mechanisms observed by μCT in tensile specimen of PA66/GF30, RH = 0%: a) debonding at fiber ends, b) debonding at fiber/matrix interfaces, c) fiber breakages and d) matrix microcracks.

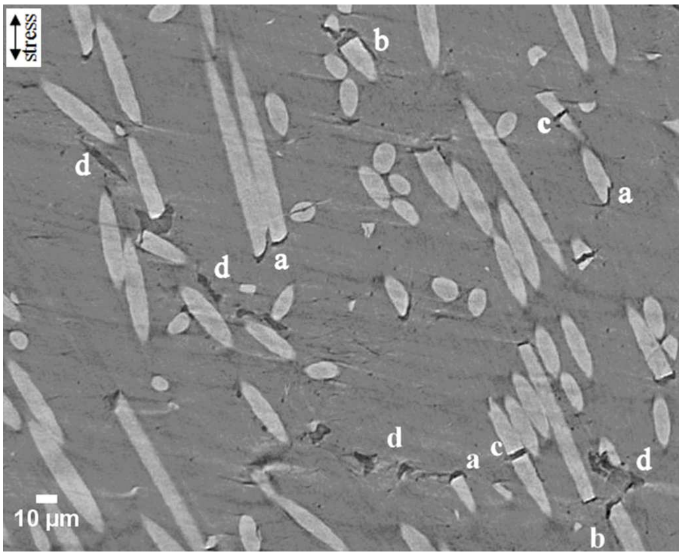

FIGURE 4.23: Damage mechanisms observed by μCT in tensile specimen of PA66/GF30, RH = 50%: a) debonding at fiber ends, b) debonding at fiber/matrix interfaces, c) fiber breakages and d) matrix microcracks. It is noted that the global fiber orientation is parallel to the applied load direction.

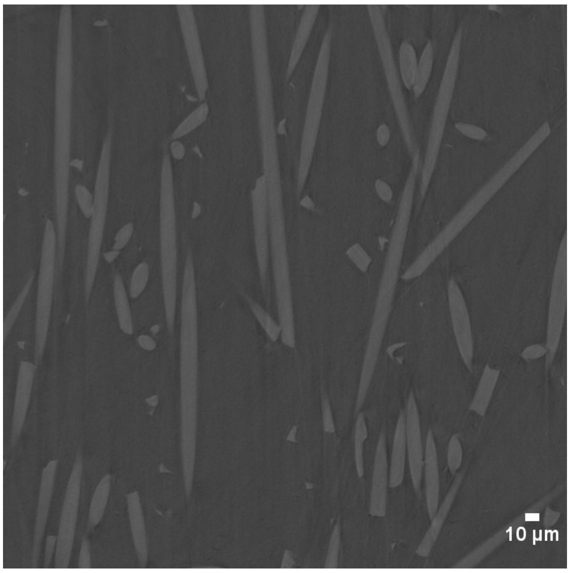

FIGURE 4.24: An overview of μCT observation carried-out on a virgin sample (non-tested) extracted from an injected plate of PA66/GF30, RH = 0%. Noticeable damage, which can be induced by injection process or sample cutting preparation, is not observed.

4.4.3 Discussion

The damage mechanisms observed in PA66/GF30 are strongly affected by the moisture content variation. The flexural strength is reduced with increasing moisture content, which is assumed to be due to the combination of damage and polyamide plasticization effects (Fig. 4.13).

Consistent results are also observed regarding to the qualitative observation of **the number of damaged zone** on the composites surface which shows that the higher RH results in higher damage level, at every stage of the loading. Moreover, Fig. 4.25 shows a comparison of damaged area for the three specimens with different moisture content at high relative flexural stress near to the failure. It is obvious that the number of damaged area increases while increasing the moisture content. The presence of water molecules inside the composite can reduce the mechanical performances of the polyamide as well as the fiber/matrix interfacial properties due to the plasticization effect and the mismatched fiber-matrix expansion during the ageing period. This might bring about a change in the overall mechanical and damage properties of PA66/GF30.

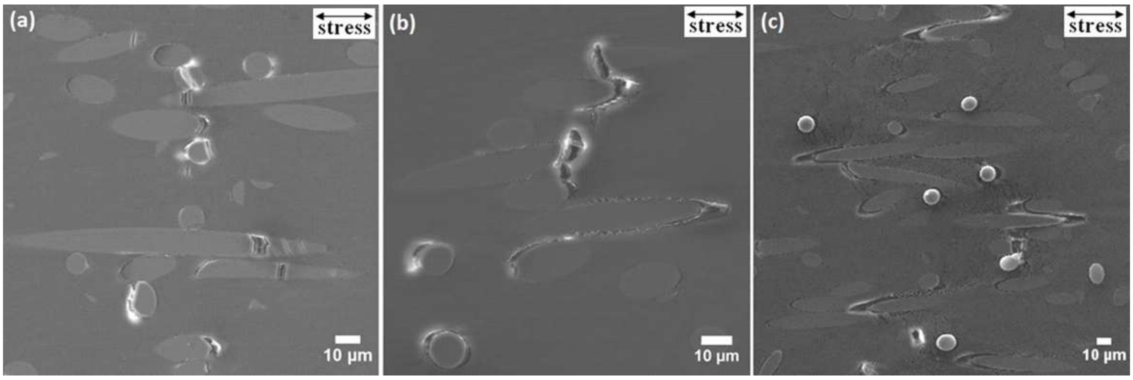

FIGURE 4.25: Damage mechanisms of longitudinal PA66/GF30 specimen at different RH content, a) fiber breakages and matrix microcracks at 95% σ_f of RH = 0%, b) matrix microcracks at 98% σ_f of RH = 50%, c) matrix microcracks and matrix deformation bands at 98% σ_f of RH = 100%.

The damage initiation in the form of fiber/matrix debonding at fiber ends is observed and this experimental finding confirms the results reported by Sato et. al. [Sato 1984]. However, the interface debonding at fiber ends are not the only locations where the damage initiation exclusively occur. Indeed, the damage also initiates from locations where fibers are relatively close to each other. This mechanism has been observed in all investigated specimens regardless their RH contents. These local configurations generate stress concentrations, which induce an early occurrence of the damage. Several scenarios for the position of damage initiation in PA66/GF30 are then proposed as shown in Fig. 4.26.

The damage initiations for RH = 0%, RH = 50% and RH = 100% specimens start around 30% of their respective flexural strength. If these relative percentages of flexural stresses are converted into the normalized load values based on the y-axes of Fig. 4.13,

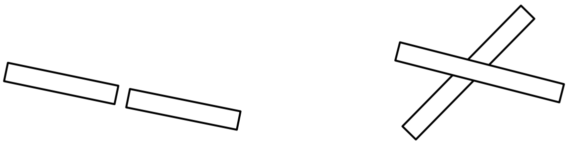

End to end of fibers

Body to body of fibers

End to body of fibers

Fibers parallel to each other

FIGURE 4.26: Several scenarios for the location of damage initiation.

it can be seen that the damage initiations for RH = 0%, RH = 50% and RH = 100% respectively started at 0.33, 0.21 and 0.15 of normalized load values which shows that the damage in RH = 0% specimen starts to develop at significantly higher load level than those in RH = 50% and RH = 100% specimens.

For **RH = 0% specimen** where the water uptake is zero, the damage initiates at high load level and the damage remains confined and low. The damage has been notably observed in the form of fiber/matrix interfacial decohesions and fiber breakages (Fig. 4.15). This indicates that the RH = 0% specimen exhibits good interfacial properties compared to both other RH conditions. This is mainly due to the absence of water content and small level of interfacial decohesion while stress level increases. The good interfacial properties insure a stress distribution in the fibers when the composite is subjected to mechanical loading. This aspect increases the probability of occurring of fiber breakages and thus it is possible to observe few fiber breakages at the damage onset corresponding to 33% of σ_f. As this is only the damage initiation, the number of the fiber breakages is very limited and confined in few locations of the investigated zone. This is common in short fiber reinforced composites due to their aspect ratios, local orientation with respect to the macroscopic applied stress and the local multi-axial stress concentration [Meraghni 1995, Meraghni 1996]. At high relative flexural stress, matrix microcracks initiate at locations where broken fibers are close to each other (Fig. 4.25a). Fiber breakage induces stress redistribution into the matrix and surrounding fibers. Since locations where fibers are close to each other also generate local stress concentration, the matrix microcracks and another breakage of the adjacent fibers would occur. These matrix microcracks than propagate in a brittle way (Fig. 4.22).

The specimens with **RH = 50%** and **RH = 100%** exhibit many fiber/matrix interfacial decohesions, with localized strained matrix around the decohesion zones. The difference between both RH levels is the lower damage level of RH = 50% specimen than that of RH = 100% specimen (Figs. 4.25b and 4.25c). Matrix microcracks that preferably propagate in a ductile way are observed both in RH = 50% and 100% specimens. Matrix deformation bands, which indicate high local deformation of matrix are observed frequently in RH = 100% specimen (Figs. 4.19 and 4.25c). However, this occurrence is not dominant for RH = 50% specimen. It is noted that a high moisture induces a high plasticization effect, which could explain the presence of localized deformation band in the RH = 100% specimen.

It is noted that some **fiber breakages** are observed on the specimens with RH = 50% and RH = 100% at high relative flexural stress level. These fiber breakages occur statistically in small proportions and hence induce a load transfer to the surrounding matrix leading to the matrix microcracks and interfacial debonding propagation. In addition, as abovementioned in this section, fiber/matrix decohesion happens at a stress level significantly lower than in the case of RH = 0%. This indicates that the interfacial properties are degraded when the moisture content is high due the water uptake of the material. The water content has an influence on the matrix and therefore on interfacial properties of PA66/GF30, which induces higher level of fiber/matrix decohesion. Due to the important fiber/matrix debonding, the stress magnitude in the fibers remains low even under high relative flexural stress, which explains why fiber breakages appear in small proportions compared to matrix microcracks and interfacial debonding.

4.5 Effect of microstructure on the damage mechanisms of PA66/GF30

For the sake of completeness of the damage analysis in PA66/GF30, the in situ test has been extended to study the microstructure effect. For this purpose, *the transverse and longitudinal specimens* are compared. Only specimens conditioned at RH = 50% are analyzed in this microstructure study.

The results show that, in terms of **mechanical properties**, the Young modulus and ultimate stress of the transverse specimen are around half than that of the longitudinal specimen, as shown in Fig. 4.27. On the other hand, the ductility of the transverse specimen is around twice than that of the longitudinal specimen. The load transfer efficiency in the transverse specimen is lower than that in the longitudinal specimen, which leads to the lower mechanical properties in the transverse specimen. The trend is the same as the stress-strain curve in dry PA66/GF30 previously discussed in Chapter 3.

The damage mechanisms behavior in the transverse specimen is the same as the one observed in the longitudinal specimens previously discussed in this chapter. The damage is initiated at around 30% σ_f, preferably at locations where fibers are close to each other due to the local stress generation. Due to the microstructure condition in the transverse specimen where the fibers are dominantly perpendicular to the loading direction, only few damage initiations at fiber ends can be observed. An example of sequential images of the transverse specimen with RH = 50% at different relative stress level can be seen in Fig. 4.28.

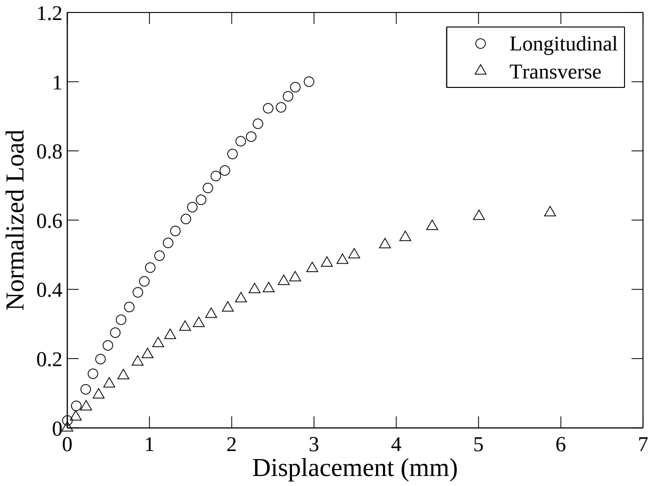

FIGURE 4.27: Tensile properties of longitudinal and transverse specimens conditioned at RH = 50%.

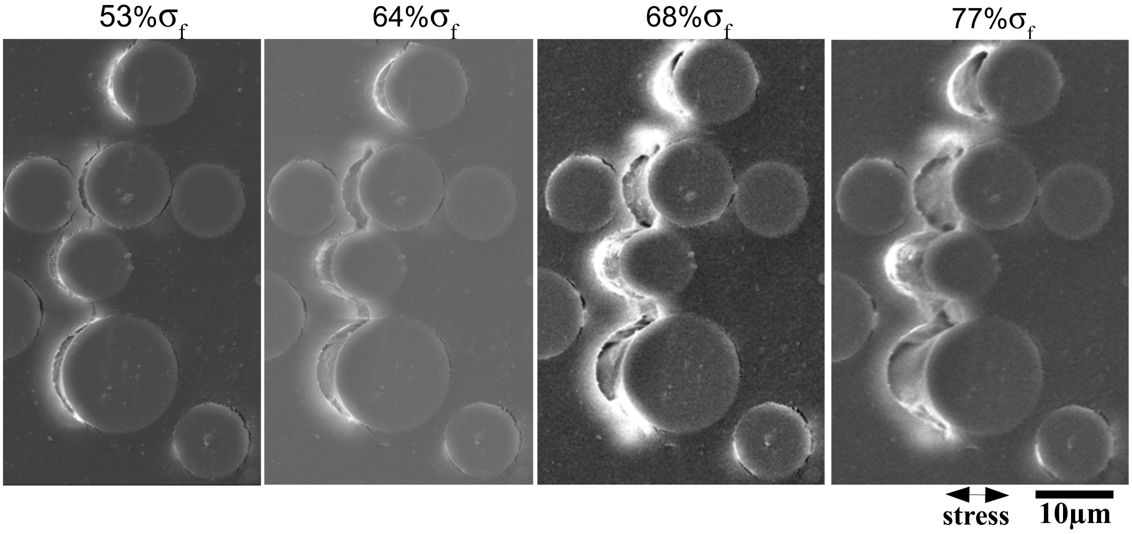

FIGURE 4.28: SEM image sequences representing damage evolution of RH = 50% transverse specimen at several relative stress levels.

In terms of **damage level**, the transverse specimen exhibits higher damage level than that in the longitudinal specimen. In addition to the stress transfer influence on the mechanical properties, the lower stress transfer efficiency in the transverse specimen also impacts its damage level. For a comparison purpose, microscopic damage indicator is proposed to quantify the damage level in PA66/GF30. Due to the nature of the investigation method which involves a localized microscopic view of the damage, the feasible definition of scalar damage parameter is by measuring the debonded area observed by SEM divided by the representative area of the observation. The measurement is performed at each increment of relative stress level. The chosen representative area is based on the known volume fraction of the fiber ($v_f = 18\%$). This damage quantification is based on the assumption that the damage appears in 2D image represents of that happens in the volume. One can see from Fig. 4.29 that the transverse specimen exhibits higher damage than that in the longitudinal specimen.

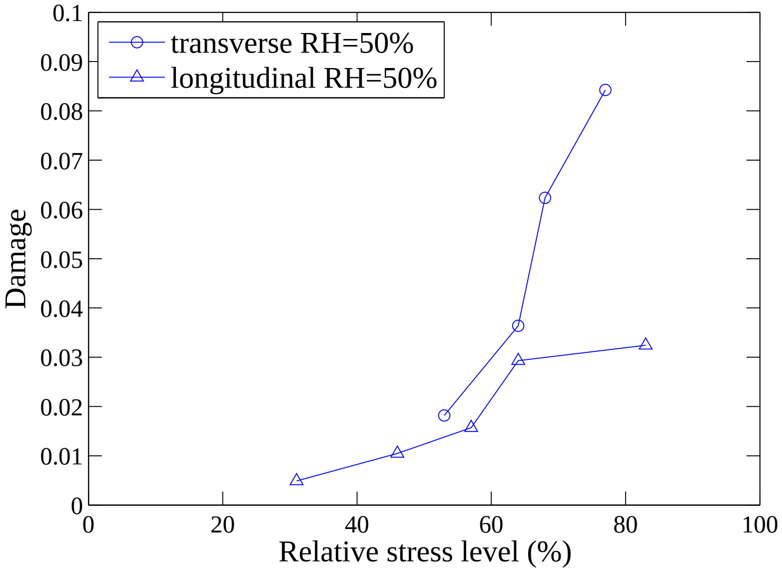

FIGURE 4.29: Damage level of RH = 50%, longitudinal and transverse specimens.

4.6 Damage mechanisms of PA66/GF30 in compressive zone

The damage behavior of PA66/GF30 in the compressive region of the sample is also investigated both in longitudinal and transverse specimens, in all RH contents. It is observed that the damage is mainly in the form of fiber-matrix interfacial debonding. While the damage initiation in the tensile region starts at around 30% of stress level, as discussed in Section 4.4.3, the damage in compressive zone starts to occur at high stress level around more than 80% of the relative flexural stress, regardless of the RH content. As shown in Fig. 4.30, fibers can be completely debonded from the matrix at the stress level near to failure. This could be due to the fiber that doesn't contribute to the stress transfer and due to the localized shear stress at high relative flexural stress. However, the damage in this zone cannot be considered predominant since it occurs only at few local zones at high stress level and it doesn't contribute to the material's final failure.

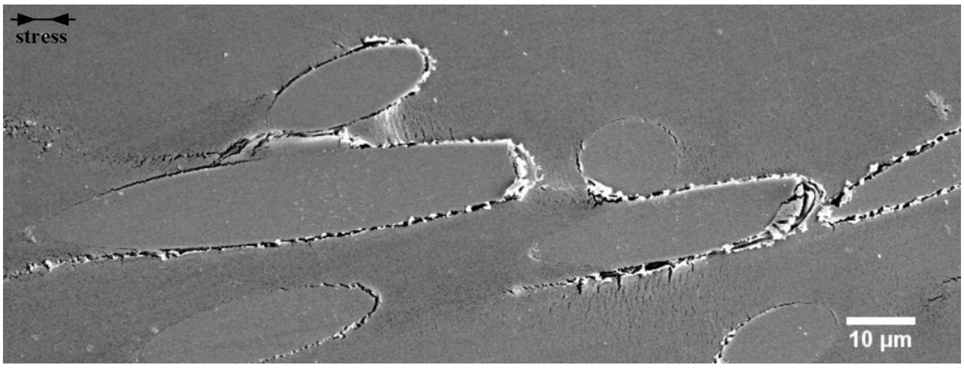

FIGURE 4.30: Damage mechanism in compressive zone of RH = 50%, longitudinal specimen at 99% σ_f.

4.7 Concluding remarks

The damage scenarios for PA66/GF30 specimens conditioned into different relative humidity conditions have been investigated. Experimental results show that the relative humidity conditions strongly impact the damage mechanisms in terms of their level and chronology. The damage in RH = 0% specimen initiates at significantly higher load level that those in RH = 50% and RH = 100% specimens. The higher relative humidity conditions also results in higher damage level.

The predominant damage mechanisms for RH = 0% specimen are fiber/matrix debonding at fiber ends and fiber sides, fiber breakages and brittle matrix crack propagation. RH = 50% and 100% specimens exhibit almost the same predominant damage mechanisms, though damage level between both RH contents is essentially different. For both RH contents, the predominant damage mechanisms are fiber/matrix debonding at fiber ends and fiber sides, accompanied with locally strained matrix zone around the debonded fibers and ductile matrix microcracks. Matrix deformation bands are observed frequently in RH = 100% specimen but this occurrence is not dominant in RH = 50% specimen.

It was observed that longitudinal and transverse specimens exhibit similar damage mechanisms. However, the transverse specimen exhibits higher damage due to its lower stress transfer efficiency.

Comparisons with μCT results indicate that the observations of in situ specimens at the surface matched suitably with that observed inside the specimen for dry and humid specimens.

Based on such observations, damage chronologies that include the effect of moisture content are proposed as follows:

i. Damage initiation occurs in the form of fiber/matrix debonding at fiber ends and more generally at locations where fibers are relatively close to each other due to the generation of local stress concentration (for three studied RH contents). Specifically for RH = 0%, damage initiation can also occur through some fiber breakages besides the previous forms of mechanisms.

ii. Interfacial decohesions further propagate along the fiber/matrix interface (for all studied RH contents) accompanied with locally strained zone around the fiber (for RH = 50% and 100%), and occurrence of new fiber breakages (for RH = 0%).

iii. At high relative flexural stress, matrix microcracks develop and propagate in a brittle way (for RH = 0%) and in a ductile way (for RH = 50% and 100%), accompanied with high matrix deformation bands (for RH = 100%).

iv. The propagation of the matrix microcracks brings about the damage accumulation leading to total failure.

CHAPTER 5

Multiscale fatigue damage characterization in dry PA66/GF30

Contents

During fatigue or cyclic loading of reinforced thermoplastics, several phenomena may develop concurrently, such as damage, cyclic creep and increase of temperature. All of them may contribute to the overall fatigue strength of the material. A comprehensive study of fatigue damage behavior is necessarily a coupled analysis of all interrelating phenomena during fatigue loading.

In this chapter, the study is aimed to characterize fatigue damage mechanisms of dry as molded PA66/GF30 under uniaxial constant amplitude loading. It is proposed to use a combined analysis of dynamic modulus, cyclic creep, dissipated energy and temperature evolution during fatigue testing together with post-mortem 3D damage analysis by X-Ray microtomography (μCT) to further understand the damage mechanisms of PA66/GF30 during fatigue testing. To evaluate the process induced anisotropy, two directions, longitudinal and transverse to the mold flow direction (MFD), are examined. In addition, a particular attention is given to the effect of skin-shell-core formation on the damage mechanisms of PA66/GF30.

For a comprehensive data analysis and discussion, literature review on fatigue behavior and properties, as well as its corresponding fatigue damage development in reinforced thermoplastics are overviewed prior to analyzing the experimental results.

5.1 Review on fatigue behavior and the related damage in reinforced thermoplastics

In general, fatigue behavior of fiber-reinforced composites is a quite complex phenomenon. Composite materials are heterogeneous and anisotropic, and their behavior is more complex than that of homogeneous and isotropic materials such as metals. Under fatigue loading, load-bearing capacity of composites decreases with cycles. This could result in failures at stress levels which are often significantly below the quasi-static tensile strength. One of the reasons of this material deterioration is due to the occurring of damage. Unlike the damage in metals which is predominantly induced by a single crack, the damage mechanisms in polymer composites are in the form of multiple damage modes which are spatially distributed inside the material [Klimkeit 2011, Uleck 2006]. Moreover, the damage in reinforced composites could start very early and then propagate progressively. Different damage modes can occur such as fiber fracture, matrix microcracking, matrix crazing, fiber/matrix interfacial debonding, fiber buckling, etc. These damage mechanisms may interact each other and their damage kinetic may not be the same.

Besides the damage, there are many other factors that influence the fatigue behavior and properties of composites. Among the parameters that influence the fatigue performance are:

- fiber characteristics (length, diameter, orientation, ...)
- matrix material (visoelasticity, viscoplasticity, damping, ...)
- fiber/matrix interfacial properties
- reinforcement type (continuous/discontinuous fiber, unidirectional, laminate, ...)
- environmental condition (moisture absorption, temperature, UV light)
- loading condition (stress ratio R, frequency, amplitude, signal form, ...)

In this section, the contributing factors affecting the overall fatigue strength and behavior of composites, especially the ones related to the current study, are reviewed.

5.1.1 Effect of environmental conditions on the fatigue behavior

As discussed in Chapter 4, the reinforced polyamides can absorb water due to the polar amide groups of the polyamide matrix. The amount of absorbed water, depending on the environmental conditions such as temperature and relative humidity, highly influences the physical, thermal, mechanical, as well as the damage behavior and properties of the composites. In a real service life of a polyamide matrix composite, due to the fluctuating environmental conditions, or due to the increase of water absorption and temperature during fatigue loading, the material properties of the composite may alter drastically. This can happen especially when the material experiences a phase shifting, from the zones above to below the glass transition temperature (T_g) or the opposite. Therefore, for a precise design of components made of reinforced polyamides, considering these factors is crucial. In the open literature, the effects of environmental conditions on the fatigue behavior of reinforced polyamides have been studied by varying the temperature and water content of the composites.

Effect of water content on the fatigue behavior Horst and Spoormaker [Horst 1997b] performed fatigue tests at 23 °C and stress ratio of 0.1 at dry as molded and conditioned samples of short glass fibers reinforced polyamide-6 composites. For the conditioned sample, the specimen has been exposed in laboratory room condition for at least 1 year. They reported that conditioned specimens have matrix material with a much more ductile behavior compared with specimens investigated in their dry as molded state. In both cases, ductility is present, although in the conditioned state the ductility is much more pronounced. The difference in ductility is enhanced by the detrimental effect of water on the fiber/matrix interfacial strength as the water absorption reduces the fiber/matrix interfacial strength of the composite.

Barbouchi et al. [Barbouchi 2007] evaluate the effect of water content on the fatigue behavior of short glass fiber reinforced polyamide-66. It was observed that water influences the fatigue behavior of the composites. The *S*–*N* curve of dried samples (0.2 wt% of water) is above the one of humid samples (3.5 wt%).

Effect of temperature on the fatigue behavior Similar to the effect of water content, the temperature also influences the properties of reinforced polyamides. To observe the temperature effect on the fatigue behavior of composites, usually the material is examined at various temperatures, such as at $T < T_g$, $T > T_g$ and $T \approx T_g$.

Jia and Kagan [Jia 1998] studied the effect temperature variation (-40, 43 and 121 °C) on the tension–tension fatigue behavior of polyamide-66 and polyamide-6 reinforced with 33 wt% short glass fibers. Prior testing, aging was performed in air at 121 °C for 0, 100, 500 and 1000 h. They proposed a material characteristic master curve, indicating a correlation between tensile and fatigue strength, concerning the influence of temperature and thermal aging.

Mourglia-Seignobos [Seignobos 2009] investigated the evolution of mechanical and physical properties of PA66/GF30 under fatigue loading with variation of temperatures ($T < T_g$, $T > T_g$ and $T \approx T_g$). It was reported that the temperature influences the modulus evolution, self heating behavior and density of the composite.

De monte et al. [De Monte 2010a, De Monte 2010b] investigated the effect of temperature on the mechanical properties of polyamide-66 renforced with 35 wt% short glass fibers under tensile and cyclic loading. The influence of temperature on cyclic strengths, both for tension–tension and tension–compression loading, is comparable with the one on tensile loading. At 23 °C, for the applied stress ranges, the material exhibits linearly elastic with negligible hysteresis area of the stress–strain loop, independently from fiber orientation angle, load ratio and specimen thickness. In contrast, at 130 °C, a certain degree of non-linearity of the material response, together with a noticed hysteresis area is observed.

5.1.2 Cyclic creep during fatigue loading

During fatigue loading of short glass fibers reinforced polyamides, cyclic creep phenomena is commonly observed [Horst 1996, Mallick 2004, Bernasconi 2009, Seignobos 2009]. It refers to the occurring of the total strain that grows steadily up to the final failure and to the hysteresis loops that move along the strain axis, as illustrated in Fig. 5.1. The figure also shows a rapid strain increase during initial cycles, followed by a more slowly and constant strain increment, and finally ended up by a sharp strain increase near to the failure.

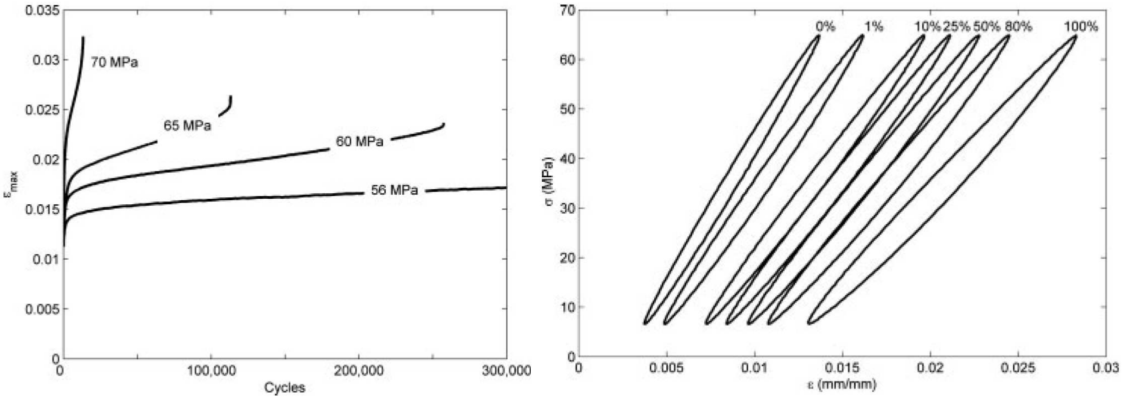

FIGURE 5.1: Cyclic creep: the increase of maximum strain with number of cycles at $f = 2$ Hz (left) and the stress–strain hysteresis loops at $\sigma_{max} = 60$ MPa and $f = 2$ Hz (right) [Bernasconi 2009].

It has also been reported a linear correlation between the number of cycles to failure and the cyclic creep speed, as illustrated in Fig. 5.2 [Horst 1996, Bernasconi 2009, Seignobos 2009]. The cyclic creep rate is defined as the increase of the total mean strain per cycle. The cyclic creep rate is evaluated during the stable stage where the strain increases linearly with the number of cycles. This observation suggests that the fatigue life is somewhat controlled by the cumulative strain.

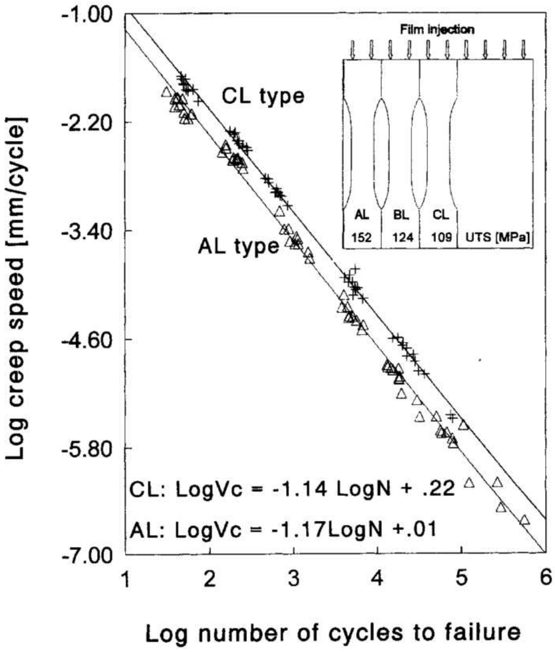

FIGURE 5.2: Cyclic creep rate as a function of the number of cycle to failure [Horst 1996].

5.1.3 Temperature increase during fatigue loading

During fatigue tests, the specimen's temperature tends to increase even when the environmental testing temperature is maintained constant. The temperature increase depends on several factors such as the applied stress and frequency. It was reported that the specimen's surface temperature follows the same trend as the maximum strain evolution. Also, higher applied stress and frequency leads to a higher temperature increase [Bernasconi 2009].

During a fatigue test of short glass fiber reinforced polyamides, two phenomena, thermal and mechanical fatigue can be developed [Noda 2001, Bellenger 2006, Barbouchi 2007, Esmaeillou 2012b]. This phenomenon refers to the temperature of specimen that increases and then stabilizes in a certain extent if the applied load or frequency is moderate or low (mechanical fatigue). In case of high applied stress or frequency, the temperature increases continuously up to the final failure (thermal fatigue). The two fatigue conditions can lead to a different slope of *S–N* curve, as shown in Fig. 5.3 [Bellenger 2006]. This figure describes that, for the specimens tested at 10 Hz, the thermal regime (at low fatigue cycles) exhibits higher slope than that of the mechanical regime (at high fatigue cycles). Both thermal and mechanical fractures occur at specimens fatigue loaded with high frequency (10 Hz). However, for the 2 Hz frequency, the fracture is only mechanical and the matrix is still in the glassy state during final failure. For the 2 Hz samples, the self-heating is low and the sample fractured in brittle mode. For the 10 Hz samples, an extensive plastic deformation of the matrix due to its rubbery state induced by a high self-heating are observed and the sample fracture is ductile.

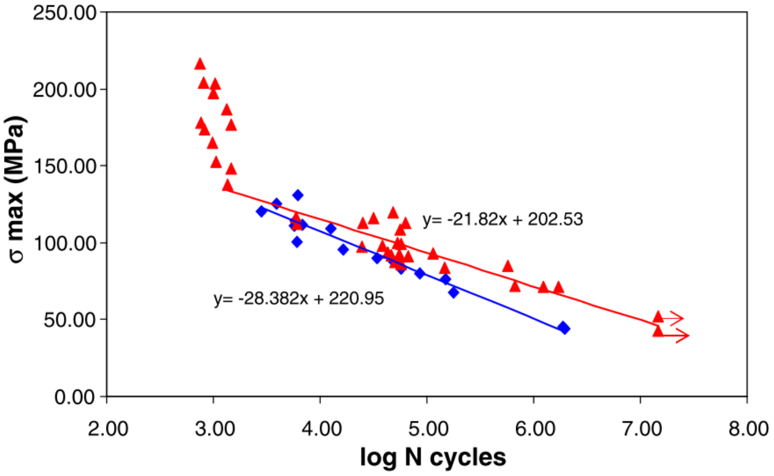

FIGURE 5.3: Wohler curve of short glass fiber reinforced polyamide-66 fatigue loaded at 10 Hz (▲) and 2 Hz (◆) [Bellenger 2006].

The phenomenon of thermal and mechanical regimes has been confirmed by Esmaeillou et al. [Esmaeillou 2012b] at even higher frequency (20 to 60 Hz) of tension-tension fatigue tests of short glass fiber reinforced polyamide-66. They reported that for low frequencies, there is only an effect of the mechanical loading while for high frequencies a coupling effect of mechanical and thermal fatigue is observed.

For the tests performed at dry and humid specimens at room temperature and frequency 10 Hz, it was reported that the 10 Hz frequency is highly enough to induce a strong temperature increase of the material. For all the applied load, the matrix is in a rubbery state when the final failure occurs [Barbouchi 2007].

In fact, when subjected to a repeated loading, microscopic phenomena can initiate and develop, causing the mechanical energy from the material to be dissipated in the form of heat. In reinforced polymers, the main mechanisms causing energy dissipation can be attributed to the viscoelastic nature of the matrix material, matrix cracks, fiber fracture, interface cracking/friction and viscoplastic damping [Steinberger 2006, Barbouchi 2007, Montesano 2013]. The viscoplastic damping is indicated to be the main factor for the case when the amplitude of the applied load is high [Barbouchi 2007].

5.1.4 Fatigue damage mechanisms

Dally and Carrillo [Dally 1969] investigated the fatigue behavior of a group of thermoplastics reinforced with discontinuous glass fibers produced by an injection molding process. It was reported that the fatigue damage of dry as molded polyamide-6 composite is localized, abundant and uniformly distributed. The cracks propagate by debonding, with limited tendency for crack propagation in the matrix. Many localized microcracks propagate and coalesce to form a larger cracked area. Different damage mechanisms were found in the reinforced polyethylene where the matrix is more ductile. Many debonded fibers are observed which lead to a high stiffness reduction. The larger strains are accommodated by the matrix without failure. This strain redistribution causes the debonded zone to progressively enlarge.

Lang et al. [Lang 1987] performed SEM observations on fatigue crack and fracture surfaces of short glass fiber reinforced thermoplastics. Several types of polyamide-66 and polystyrene matrix with different ductility and fiber/matrix adhesion quality were used. They reported that, for composites with good interfacial adhesion, the damage under stable fatigue crack propagation is characterized by microvoids and microcracks at fiber interface without matrix layer adhered on the fiber surface due to the adverse effect of fatigue loading on the fiber/matrix interfacial bond strength. In contrast, in the fast fracture region of the composites with good interfacial adhesion, fibers are covered with a thin matrix layer which indicates a cohesive type of failure. For composites with poor interfacial adhesion, crack propagation under both stable fatigue and fast fracture conditions occurs directly at the fiber interface without any adhered matrix layer.

Lang et al. [Lang 1987] also demonstrated a dependence of the composite's matrix ductility on the fiber orientation, with more matrix ductility in the case of fibers perpendicular to the applied load. Moreover, the fiber/matrix adhesion influences the matrix ductility. Better adhesion gives a higher efficiency on the fiber/matrix load transfer, resulting in a less matrix drawing.

Horst and Spoormaker [Horst 1996, Horst 1997b] performed fractography analysis onto the fracture surface of fatigue loaded short glass fiber reinforced polyamides by scanning electron microscopy (SEM). They proposed a damage mechanisms scenario consisting of formation of bridged cracks as illustrated in Fig. 5.4. They consider the damage mechanisms as follows:

i. The damage starts at fiber ends where local stress concentration is the highest.

ii. The microvoids then propagate along the fiber interface in the form of fiber/matrix interfacial debonding.

iii. As the stress supported by the matrix increases gradually due to the fiber/matrix interfacial debonding, the local stress of the matrix may exceed the yield limit and thus facilitate local plastic deformation of the matrix. The voids become microcracks which propagate in the matrix.

iv. The voids coalesce in the matrix but these matrix microcracks remain bridged with a mechanism similar to craze in unreinforced polymers. Many bridged cracks propagate until it reaches a critical depth and then fails during the last fatigue cycle.

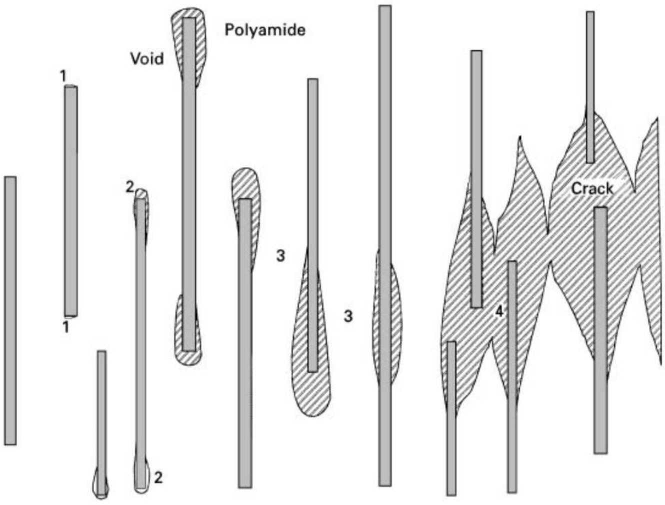

FIGURE 5.4: Damage mechanisms of reinforced polyamides under fatigue loading [Horst 1997b].

The fatigue damage mechanisms of short glass fiber reinforced polyamide-66 were proposed by Noda et al. [Noda 2001] based on optical microscopic observation on cross-section surfaces of the composite prior final failure. The fatigue behavior was classified into two damage mechanisms, depends on whether the fatigue test temperature (T_{exp}) is carried out below or above glass transition temperature (T_g) of the matrix. The proposed fatigue damage mechanisms are detailed as follows:

i. The damage starts by void at fiber ends.

ii. The microcracks propagate around fiber ends ($T_{exp} \leq T_g$), or the microcracks propagate accompanied with debonding along fiber sides, as well as development of crack walls ($T_{exp} \geq T_g$).

iii. The cracks propagate between fiber ends in a brittle manner ($T_{exp} \leq T_g$), or the crack walls remain connected by bridges ($T_{exp} \geq T_g$) in a ductile manner.

iv. The fast crack propagation occurs after the crack reaches a critical size followed by the specimen's failure.

Casado et al. [Casado 2006] analyzed quantitatively the surface damage of fatigue loaded 35 wt% short glass fiber reinforced polyamide-66 by surface roughness measurement. They proposed three stages of the surface roughness evolution during fatigue loading as follows:

i. The surface roughness remains the same as the initial value, associated only to the discontinuities due to fibers.

ii. The surface roughness increases with fatigue cycles, associated to the evolution of pseudo-cracks that can be considered as the damage. This damage evolution is associated linearly to the increase of temperature during fatigue loading, independently of applied stresses.

iii. The surface roughness stabilizes at the maximum value reached at the previous stage and then increases significantly near to the failure.

Based on investigation of macroscopic evolution such as hysteresis curve, elastic and plastic strain, dynamic modulus and dissipated energy, Mourglia-Seignobos proposed three stages related to the evolution of fatigue properties of PA66/GF30 as follows [Seignobos 2009]:

i. The first stage is characterized by the self-heating of the material during low number of initial cycles. This first stage of self-heating is not associated with damage mechanisms that can affect the elastic modulus.

ii. The second stage is the beginning of the mechanical damage and it influences directly the fatigue life of the composite. In this stage the strain increases and creep fatigue is inversely proportional to the length of life, as in the case in static creep. The energy dissipated per cycle is constant and the viscoelastic behavior of the composite is stable. Also, the reduce of dynamic modulus is linear function of the logarithm of the number of cycles.

iii. The final stage demonstrates the dynamic modulus falls abruptly and the evolution of the strain is no longer linear with the logarithm of the number cycles. The failure criterion is independent from the temperature and it corresponds to a critical value of macroscopic elastic strain.

These stages are approximately equivalent to the ones proposed by Casado et al. [Casado 2006] by their surface roughness measurement method, especially to consider that the damage develops at the second stage. Esmaeillou et al. [Esmaeillou 2012b, Esmaeillou 2012a] also proposed equivalent behavior as the damage only starts and develops during the second stage where the temperature profile is more or less stabilized. However, they reported that the dynamic modulus reduction is not observed during this second stage.

Esmaeillou et al. [Esmaeillou 2011] performed tension-tension fatigue tests of PA66/GF30 with 20 Hz frequency. They divided the *S*–*N* curve (Fig. 5.5) into three zones as follows:

I. Stabilized thermal regime, possibility of damage development. Diffuse damage is proposed to establish in this region where the applied maximum stress is low, as the temperature and modulus evolution are approximately stable.

II. Localized temperature rise, no diffuse damage development. For intermediate value of applied maximum stress, the temperature rise is localized, leading to highly deformed (micro-ductile) fracture areas.

III. Very limited temperature rise, brittle failure. For very high maximum applied stress, the micro-ductile areas completely disappear. As the material experiences very high fatigue strain rate, the material cannot accommodate the deformation through localized temperature rise, which leads to a brittle failure.

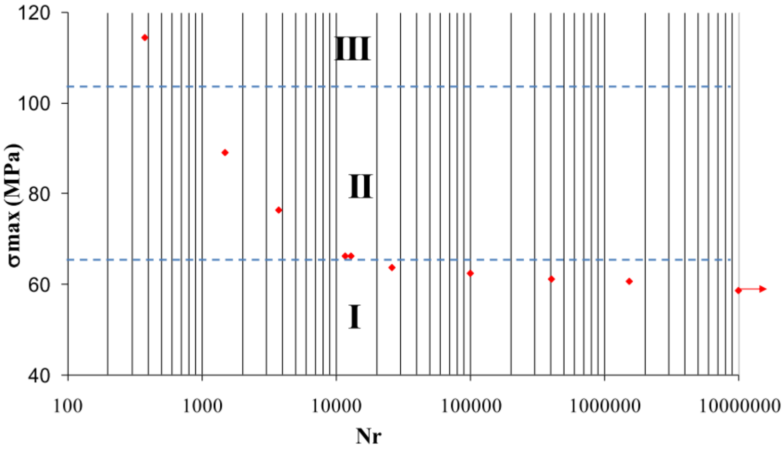

FIGURE 5.5: *S–N* curve of PA66/GF30 under tension-tension fatigue tests with frequency of 20 Hz [Esmaeillou 2011].

Klimkeit et al. [Klimkeit 2011] studied fatigue damage behavior of 30 wt% short glass fiber reinforced PBT and PET composites. Fatigue tests at stress ratio of 0.1 were carried out on dogbone and tubular specimens with different fiber orientations. They reported that propagation of a single macroscopic crack is not the major fatigue damage mechanism. Diffuse damage is observed in the material and void at fiber ends is the initiating point of the fatigue damage mechanisms.

5.1.5 Fatigue damage quantification

Polymer matrix composite is a highly heterogeneous material and thus, under fatigue loading, it may possess stress localizations that can initiate damages. These damages then progressively accumulate which can reduce the performance of the composite. The damage inside the composite can be evaluated through various mechanical quantities as follows:

Modulus reduction The modulus reduction has been commonly used as a damage indicator. It has been applied both in static and fatigue loading. The elastic modulus reduction has been used by Ladeveze and Le Dantec [Ladeveze 1992] to evaluate the damage during quasi-static monotonic loading of laminate composite. Fitoussi et. al. [Fitoussi 2013] applied the elastic modulus reduction to obtain damage parameter for ethylene–propylene glass fiber composite under quasi-static and high strain rate monotonic loading.

In fatigue loading, Mourglia-Seignobos [Seignobos 2009] performed fatigue tests of PA66/GF30 at different temperatures. The tests were interrupted few times to evaluate their Young modulus evolution. Between 0 and 1000 cycles, the elastic modulus increases slightly for temperatures at or above the T_g. Between 1000 cycles and failure, the elastic modulus reduces up to 5% for $T < T_g$ and 20% for $T \approx T_g$ and $T > T_g$.

The dynamic modulus, i.e. the slope of stress-strain hysteresis curve, has been employed by many authors to estimate the damage level in composites during fatigue loading [Ben Cheikh Larbi 2006, Toubal 2006, Seignobos 2009, Nouri 2009a, Meraghni 2011, Nouri 2013]. De Monte et al. [De Monte 2010a, De Monte 2010b] reported that the dynamic modulus decrease of short glass fiber reinforced polyamide-66 depends on applied load level, load ratio and temperature. Mourglia-Seignobos [Seignobos 2009] reported that the dynamic modulus reduces for 12% during fatigue tests of PA66/GF30 at $T < T_g$, while it reduces for 27% during fatigue tests around and above the T_g.

Nouri [Nouri 2009b] performed displacement controlled fatigue tests on short glass fiber reinforced polyamide-6 and the dynamic modulus evolution was evaluated. Two stages of dynamic modulus reduction were observed. The first stage reflects a rapid modulus reduction due to the thermal softening of the polymer matrix. The second stage corresponds to a stable and constant slope of the dynamic modulus reduction, with a less extent of modulus reduction compared to the one during the first stage. This dynamic modulus data is then used as the damage parameter input for a phenomenological fatigue damage modeling approach [Nouri 2009a, Meraghni 2011, Nouri 2013].

Density measurement Density measurement generally can be used to highlight the damage that can induce a change in material's volume such as formation of voids in the matrix, fiber/matrix interfacial debonding and crystalline formation rearrangement. This technique has been employed by Mourglia-Seignobos [Seignobos 2009] by measuring the density of PA66/GF30 specimens in the rupture zone. It was reported that the density decreases by only 0.1% for $T < T_g$ and about 0.15% for $T > T_g$ and $T \approx T_g$. This density decrease doesn't agree very well with the reduction of elastic modulus (up to 20%) and dynamic modulus (up to 27%). It was proposed that the reduce of density is mainly due to the matrix cavity.

Identification of void characteristics X-ray micro-computed tomography (μCT) is a non-destructive technique that allows to visualize an object in 3D. Moreover, by image thersholding technique, the constituents or phases inside the 3D object can be quantified. The image thresholding is a technique that involves evaluation of gray level of each image voxel. It defines whether the gray level is above or below a certain threshold level, which in turn results in obtaining a binary image regrouping the objects to be defined as the same phase. For damage analysis of a material, it can be carried out by identifying the voids developed inside the material through the thresholding technique. Further post treatment is then required to analyze the void characteristics such as their dimensions and Euler orientation angles.

This void identification has been applied in various materials such as brass alloy [Isaac 2008], elastomer [Le Saux 2011] and metal matrix composites [Hosokawa 2013]. For the void characterization in short glass fiber reinforced polyamides, one can refer to the work of Cosmi and Bernasconi [Cosmi 2013]. They analyzed the total void volume inside the composite at several levels of fatigue life. They reported that the volume of microvoids increases with the number of cycles only at the final stage of fatigue life. In some cases, a lower void volume is observed in specimens with increasing fatigue damage, as indicated by the modulus reduction.

Jegou [Jegou 2012] analyzed the features of voids in 50 wt% short glass fibers reinforced polyamide-66 specimens conditioned at 40% relative humidity by μCT technique. The composite was subjected into 2000 cycles of fatigue loading at room temperature, frequency of 1 Hz and several stress amplitudes with stress ratio of $R = \sigma_{min}/\sigma_{max} = 0$. It can be seen from Fig. 5.6 that the void volume fraction, the ratio between the void volume and total studied volume, increases with the increase of stress amplitude.

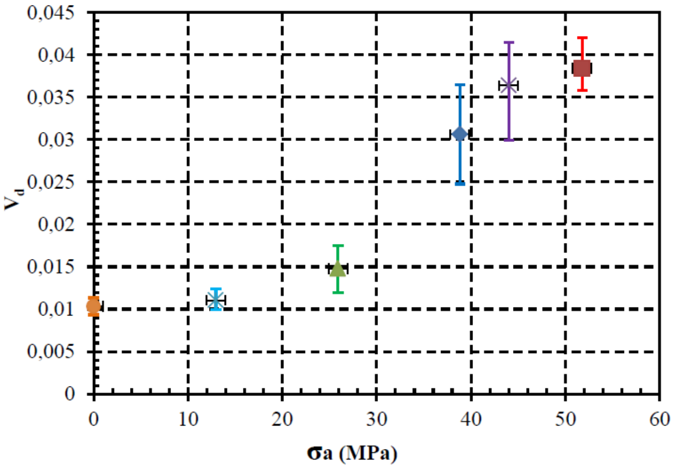

FIGURE 5.6: Void volume fraction vs. stress amplitude of fatigue loaded polyamide-66 composite [Jegou 2012].

5.2 Experimental procedures and fatigue damage investigation techniques

Fatigue tests were performed on dry as molded PA66/GF30 ($< 0.2\%$ water content) at room temperature by applying a sinusoidal signal, under load controlled mode, at constant amplitude and fixed loading ratio. To prevent specimens from buckling, the tests were conducted under tension-tension mode, with a stress ratio of $R = \sigma_{min}/\sigma_{max} = 0.1$. The frequency of 3 Hz was chosen in order to avoid a global heat of the sample reaching the glass transition of dry PA66/GF30 ($\approx 65 - 70\ ^{o}C$) during fatigue loading. Fatigue strength of the material was evaluated within the range of 10^3 to 10^6 cycles. Continuous temperature monitoring of the active zone of the specimen was assured by the CEDIP Jade III MWR infrared camera with a spectral range between 3.9 and 4.5 μm.

Damage mechanisms and its evolution were investigated by the use of μCT analyses performed on longitudinal and transverse specimens after being subjected to fatigue loading up to different percentages of total fatigue life. For this damage investigation, the μCT experimental setup was conditioned to reach voxel resolutions of 0.7 and 1.4 μm. The longitudinal specimens were consistently carried out at 0.7 μm resolution, whereas the transverse specimens were employed at 1.4 μm resolution. Both resolutions demonstrated consistent results though the ones with 0.7 μm provided stronger physical interpretations. The dimensions of the μCT samples were $2 \times 2 \times 3.2$ mm^3, where 3.2 mm corresponds to the sample thickness. The μCT scanning was not carried out through all the sample thickness but it always covered more than half of the thickness so that the skin-shell-core structure can always be captured.

The μCT samples were machined from the central gauge-length zone of the fatigue loaded specimens. For the specimens that have been fatigue loaded up to failure, the extraction locations of the μCT samples were far from the fracture surface in order to avoid fast crack propagation effect due to the final failure. The μCT investigation on virgin sample was also carried out as a reference for the damage analysis of fatigue loaded specimens. By segmentation technique with proper and consistent selection of threshold value, the voids inside the analyzed μCT volume element can be isolated, thereby the void features such as volume, Euler orientation angles and aspect ratio can be quantified. The threshold level was defined and optimized based on visual observation of the voids at fatigue loaded specimens. All the specimens, including the virgin, were treated using similar and constant threshold level in order to allow a direct comparison between them. In this work, μCT images are presented to demonstrate the fatigue damage mechanisms of the composite. The void volume, aspect ratio and Euler orientation angles are also presented to confirm the damage mechanisms and evolution of PA66/GF30.

5.3 Experimental results and discussion

5.3.1 Macroscopic fatigue damage evaluation

5.3.1.1 Thermo-elasto-visco-damage coupling

Fig. 5.7 illustrates the evolution of the monitored parameters, i.e. normalized dynamic modulus (E_N/E_0), maximum strain (ε_{max}) and mean temperature ($T_{mean} - T_{room}$) for the longitudinal and transverse specimens. During cyclic loading, energy dissipation can be associated to different phenomena such as damage development and intrinsic dissipation (viscous behavior). Part of the mechanical strain energy due to the damage development and viscous effect of the material is turned into heat so that thermo-elasto-visco-damage coupling can occur during fatigue loading.

The dynamic modulus reduction can be used as a damage indicator when considering a classical continuum damage mechanics framework [Nouri 2009a, Ladeveze 1992]. For all loading cases encountered in this study, the normalized dynamic modulus evolution demonstrates a stable value for the first 10^3 cycles and then decreases at a rate that depends on the loading level. In all cases, the intensity of the decrease of the normalized dynamic modulus is directly related to the fatigue life of the specimen.

The evolution of mean temperature exhibits two regimes (Fig. 5.7). The first one corresponds to a stable normalized modulus, where heat dissipation seems to be mostly related to the intrinsic energy dissipation associated to the viscous nature of the composite. The second regime is associated to the onset of the decrease of the normalized dynamic modulus and it corresponds to an inflection point on the mean temperature evolution. This regime change can be associated to the fact that the strain energy is not only dissipated into heat due to the viscous nature of the composite but also dissipated into a damage development and accumulation. The evolution of dissipated strain energy shows the same trend as the temperature evolution since the increase of dissipated strain energy is not necessarily to be directly followed by the dynamic modulus reduction (Fig. 5.8).

As shown in Fig. 5.7, the maximum strain continuously increases during fatigue life. The minimum strain exhibits the same trend (Fig. 5.9) so that the strain amplitude is almost constant during fatigue loading. It can then be stated that the observed damage is associated to a combined effect of creep and cyclic loading. However, since the mean strain evolution is maintained in reasonable ranges for most of the fatigue tests (lower than 1%), and that the dynamic modulus reduction is not associated to a change in the mean strain evolution, which could indicate an acceleration of the creep damage, it is believed that most the observed damage is related to the cyclic component of the loading and that the creep damage is limited for these dry as molded specimens. The situation is different for the transverse specimen loaded at the highest maximum stress level. At such high stress level, thermal softening is considered to arise as revealed by the significant increase of the maximum strain at the end of the fatigue life. Therefore, it can be inferred that the dynamic modulus reduction is related to a high extent to the damage evolution, except for the highest loading level of the transverse specimen ($\sigma_{max} = 70\% \ \sigma_u$) where thermal softening may occur and would lead to the final failure.

The longitudinal and transverse specimens exhibit different behavior considering that the thermo-elasto-visco-damage coupling in longitudinal specimens is higher than that in transverse specimens. With the stress levels significantly lower than those in longitudinal specimens, the transverse specimens generate higher changes in dynamic modulus, strain and temperature. This is due to the fact that in transverse specimens, the polyamide-66 matrix has a more important role than that of fibers during the fatigue loading.

It can be summarized that the information of dynamic modulus is important though it becomes more difficult to completely comprehend the fatigue damage behavior without the information of strain, temperature and dissipated energy evolution. The evolution of dynamic modulus can be considered as a damage indicator. However for high stress levels, it may overpredict the damage evolution due to the high viscous effect contribution of the composite, such as the one shown in the highest loading level of the transverse specimen. Therefore, the spatial distribution analysis of damage and the microstructural investigation of damage mechanisms by μCT are necessary to further understand the *fatigue*damage in PA66/GF30.

5.3.1.2 Spatial distribution of damage

In a material discontinuity such as damage, heat transfer is hindered since there is only partial or no contact between the internal surfaces of the damage zone. This could result in a local increase of temperature in the damage zone. If one records the mean and maximum temperature on the active zone area of the specimen, it is expected that the temporal increase of the maximum temperature will be higher than that of the mean temperature when a localized damage is detected. However, the nature of this technique suggests that the level of localized damage should be high enough so that the heat generated in the damage zones can reach the surface and thus can be captured by the infrared thermography camera.

This experimental approach has been examined in PA66/GF30 specimens. As described in Fig. 5.10, the maximum temperature evolution follows that of the mean temperature, with approximately a constant offset. This result indicates that during fatigue loading, there is no macroscopic damage induced strain localization and the damage is preferably diffused over the entire specimen. An increase of maximum temperature is only observed when the number of cycles reaches 99% of fatigue life. This is due to the sudden crack propagation leading to the final fracture of the sample.

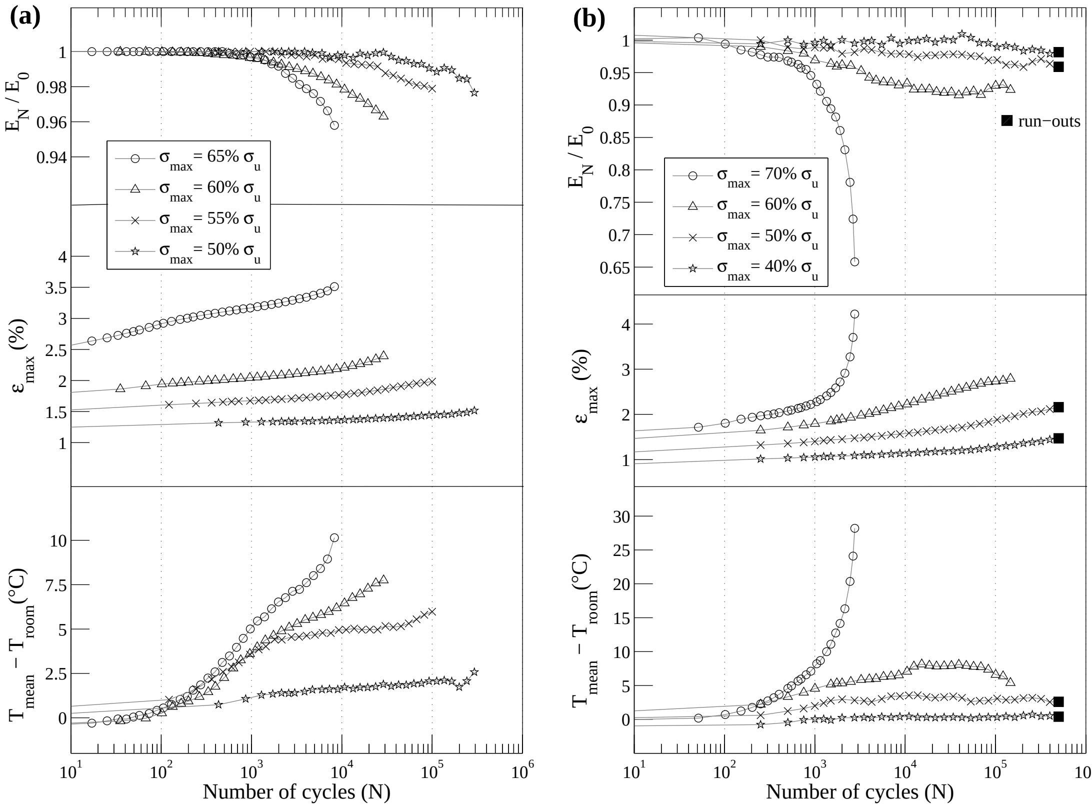

FIGURE 5.7: Evolution of normalized dynamic modulus (E_N/E_0), maximum strain (ε_{max}) and mean temperature ($T_{mean} - T_{room}$) of (a) longitudinal and (b) transverse specimens during fatigue loading of PA66/GF30. (σ_u represents the ultimate tensile strength of its respective orientation angles)

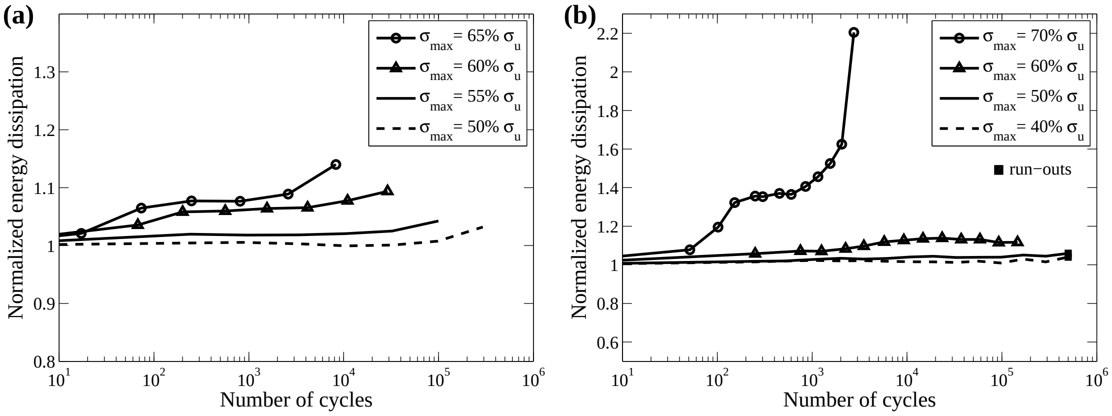

FIGURE 5.8: Evolution of normalized energy dissipation of (a) longitudinal and (b) transverse specimens during fatigue loading of PA66/GF30. The energy dissipation was obtained by evaluating the hysteresis area at each loading cycle normalized by the initial value.

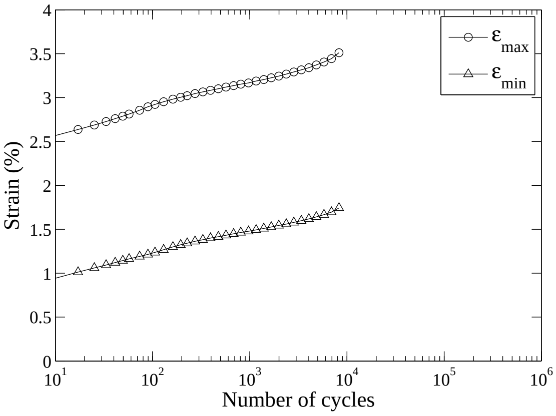

FIGURE 5.9: Evolution of maximum and minimum strain of longitudinal specimen fatigue loaded at maximum stress of 65% σ_u. All loading cases encountered in this study exhibit similar trend as ε_{min} follows ε_{max} at approximately a constant offset.

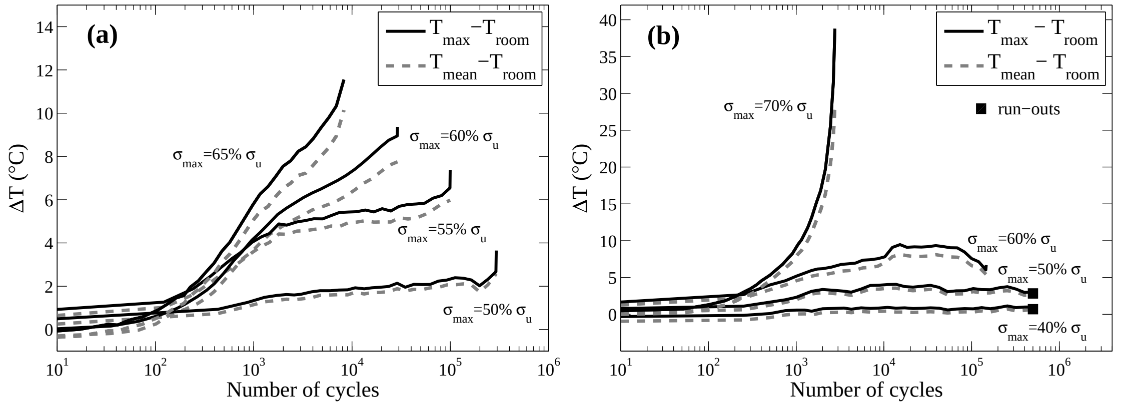

FIGURE 5.10: Evolution of mean and maximum temperature of (a) longitudinal and (b) transverse specimens during fatigue loading of PA66/GF30.

5.3.2 Microscopic fatigue damage evaluation

The μCT is a powerful 3D non-destructive investigation method to analyze microscopic characteristics of a medium. By applying 3D reconstruction, fibers in a composite can be observed and further post-processed to obtain their features such as volume, aspect ratio and orientation angles. Also, voids that are the characteristic of damage can be observed and quantified. Indeed, in fatigue loaded specimens of PA66/GF30, the appearing of zones darker than the matrix is the characteristic of voids. By comparison with virgin specimen, the presence of these dark zones can be associated to fatigue damage.

In virgin specimen, almost no visible damage is observed inside the sample, as shown in Fig. 5.11. Few zones darker than the matrix are observed in the virgin sample, which could be due to the real initial damage or due to the image artifact. In fatigue loaded specimens, these dark zones are frequently observed, notably along fiber interface. These zones correspond to the damage in the form of fiber/matrix interfacial debonding, as shown in Fig. 5.12. However, one cannot asses whether the local damage is adhesive or cohesive from this μCT investigation. Indeed, fiber/matrix interfacial debonding depends on several parameters, among them are relative humidity and fiber orientation. Voids at fiber ends are also observed in the fatigue loaded specimens, though it is not necessarily involved in the fiber/matrix interfacial debonding. Few fiber breakages are also observed but it seems this damage mechanism is not dominant. In a particular case, matrix microcracks can be developed, such as the one observed in the core layer of the transverse specimen (Fig. 5.13). The relatively thin core layer is believed to bear higher stress level due to its longitudinal (parallel) orientation to the applied load direction. Matrix microcracks, with preferential direction transversely to the applied load direction, as well as to the fibers direction, are found to develop favorably in this region.

Since the presence of the damage can be in the form of nanoscopic voids, visual demonstration by the original μCT radiographs is sometimes not sufficient. A further

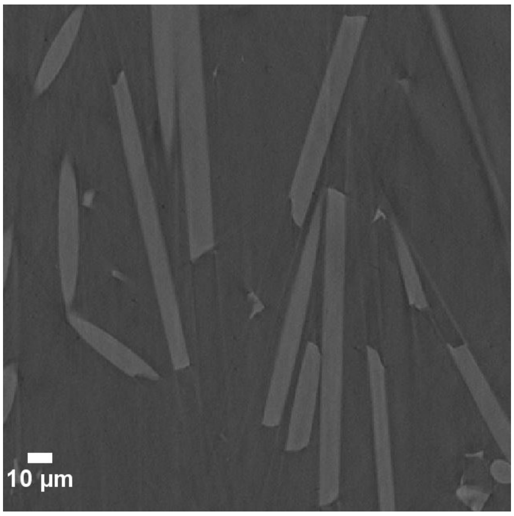

FIGURE 5.11: The μCT image of virgin sample.

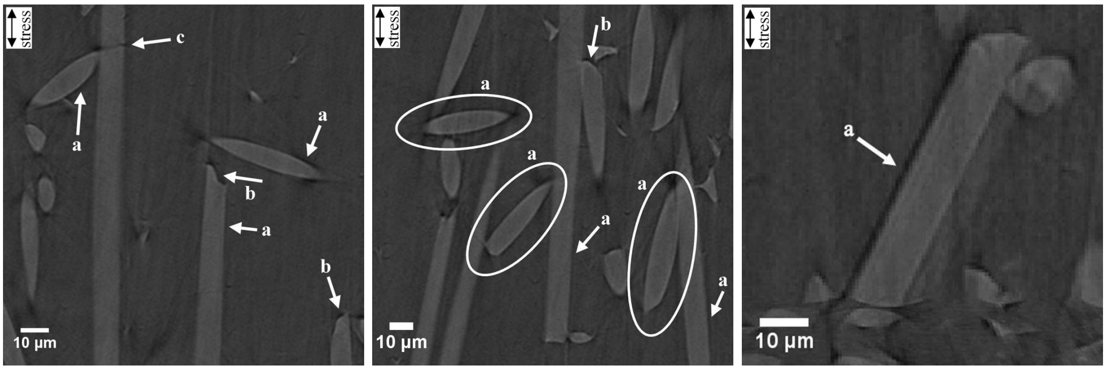

FIGURE 5.12: Damage mechanisms observed in the shell zone of longitudinal specimen that has been fatigue loaded up to failure at maximum stress of 60% σ_u; a) fiber/matrix interfacial debonding, b) void at fiber ends, and c) fiber breakage.

treatment after the segmentation process of μCT volumes has been carried out to allow a joint representation of the damage and fibers, each of them having different colors, and without the matrix on the final images. Fig. 5.14 shows an example of magnified image in a zone with highly debonded fibers. This fiber/matrix interfacial debonding is frequently observed at the fatigue loaded specimens and can be considered as the main fatigue damage mechanism for PA66/GF30. In terms of spatial distribution of damage, though the damage is diffused over the entire specimen, the damage level between different locations inside the specimen is not necessarily the same (Fig. 5.15).

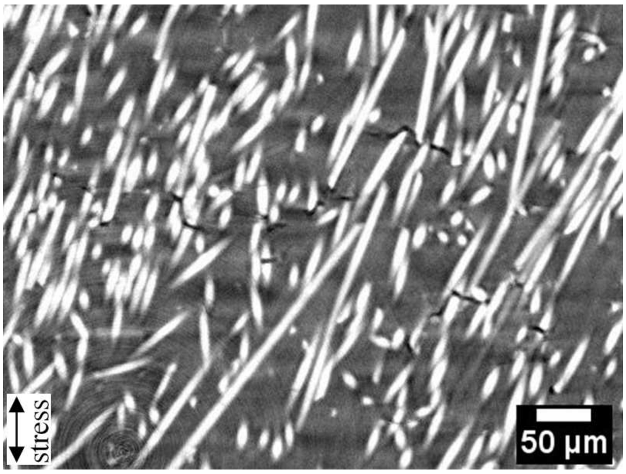

FIGURE 5.13: Matrix microcracks observed at the core zone of transverse specimen that has been fatigue loaded up to failure at maximum stress of 60% σ_u.

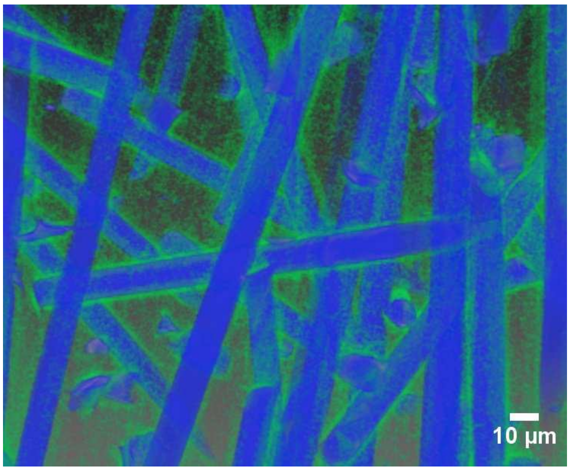

FIGURE 5.14: A rendered μCT image of a zone with highly debonded fibers in the shell layer of longitudinal specimen fatigue loaded up to failure at maximum stress of 60% σ_u. The blue and green colors represent the fiber and damaged zone, respectively.

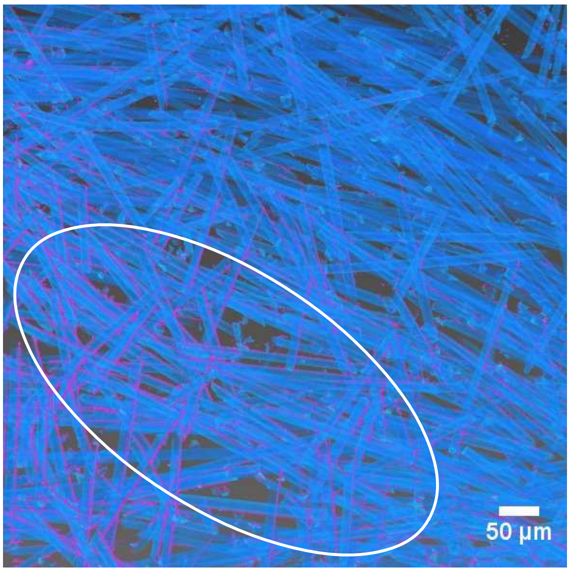

FIGURE 5.15: A rendered μCT image which shows heterogeneous damage level at microscopic scale (the highlighted zone shows higher damage). The image was taken from longitudinal specimen fatigue loaded up to 75% of fatigue life at maximum stress of 60% σ_u. The blue and (magenta) represent the fiber and (damaged zone).

As a first attempt to quantify the damage and to build a more consistent analysis on damage mechanisms of PA66/GF30, the void aspect ratio vs. void orientation angles are analyzed. To reduce the number of analyzed voids and to establish a consistent comparison between the void properties in the shell and core layers, the evaluation of void aspect ratio has been carried out in a 50 μm volume slice of the shell and core layers of the μCT volume, as described in Fig. 5.16. The μCT result of virgin specimen is given in Fig. 5.17 in the form of polar graph. For the virgin specimen, voids with low aspect ratio are observed in the shell layer. The trend in the core layer is the same as the one noticed in the shell layer. These small voids could be partly due to the real initial damage and partly due to the gray level fluctuation-induced inherent artifacts as a result of the thresholding technique. It should be noted that the thresholding technique was defined and optimized based on visual observation of voids in the fatigue loaded specimens. The chosen threshold level is unique and applied to all specimens, including the virgin sample. By this method, one can ensure that any deviations of the subsequent void aspect ratio and volume analyses for the fatigue loaded specimens are not due to the thresholding technique but mostly related to the damage development.

Figs. 5.18 and 5.19 illustrate the void aspect ratio vs. angular position of longitudinal and transverse specimens, respectively, that have been fatigue loaded up to failure at maximum stress level of 60% σ_u. Significant damage is observed when comparing these results to the one of the virgin material (Fig. 5.17). In longitudinal specimen, the voids in the shell and core layers are mainly oriented at 0^o and 90^o, respectively (Fig. 5.18). It is worth noticing that these orientations are the same as the principal fiber orientations

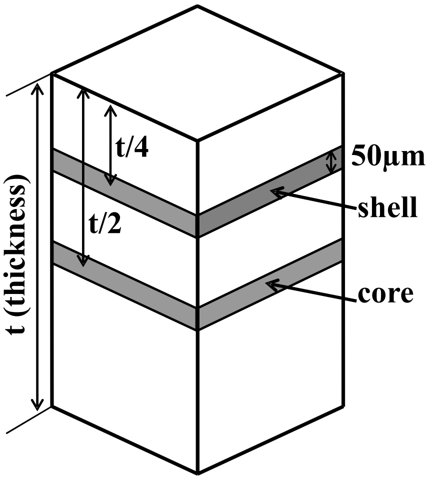

FIGURE 5.16: Description of the analyzed μCT volumes in the shell and core regions of the composite.

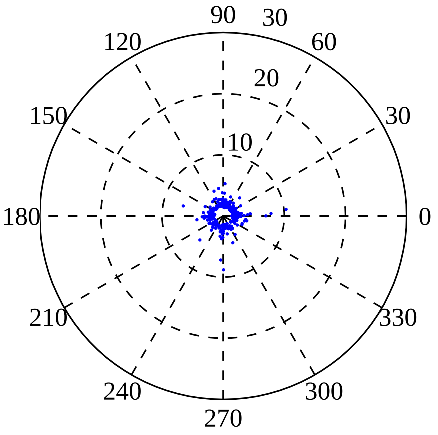

FIGURE 5.17: Void aspect ratio vs. void orientation angle in the shell zone of virgin specimen.

in the shell and core layers. It means the voids are mainly located along fiber interface in the form of fiber/matrix interfacial debonding. For the transverse specimen, the voids in the shell and core layers are both oriented at 90^o, as shown in Fig. 5.19. It shows that fiber/matrix interfacial debondings occur in the shell layer, while matrix microcracks with preferential direction transversely to the applied load as well as to the fibers direction are dominant in the core layer of the composite. The random skin layers in the longitudinal and transverse specimens exhibit the same behavior as those in the shell layers. Even though the thin random skin layers are developed, the degree of random orientation is not high and the fibers in this layer tend to orient according to MFD, which is the same orientation as the ones in the shell layer (Figs. 2.17). For the transverse specimen, less fiber/matrix interfacial debonding is observed. This is probably due to the high development of matrix microcracks in addition to the fiber/matrix interfacial debonding as observed in the 2D images (Figs. 5.12 and 5.13). These figures illustrate clearly the anisotropic nature of the damage developed at the local scale.

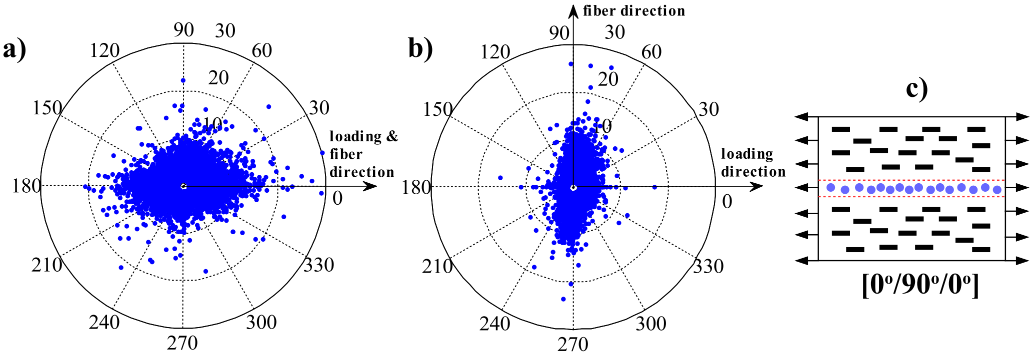

FIGURE 5.18: Void aspect ratio vs. void orientation angle in a) shell and b) core regions of fatigue loaded longitudinal specimen. Laminate representation analogy of longitudinal specimen is presented in c) for an interpretation guideline of void orientation angle.

In addition to the final stage damage investigation, similar μCT analyses were performed on longitudinal specimens that have been fatigue loaded up to several percentages of fatigue life. The voids inside the μCT volume were labeled to ensure identification of individual objects isolated from their neighbors, and each of the void was attributed with different color. It can be seen from Fig. 5.20, which shows the 2D perspective view of a chosen reference plane of the μCT volumes, that the number of void increases with number of cycles. Moreover, Fig. 5.21 illustrates the evolution of void volume as a function of void orientation and number of cycles at the shell layer of longitudinal specimens that have been fatigue loaded up to several percentages of fatigue life. It clearly shows that the void volumes increase throughout the fatigue life. It is worth noting that voids with low volumes are also observed in the virgin sample, which could be due to the real initial

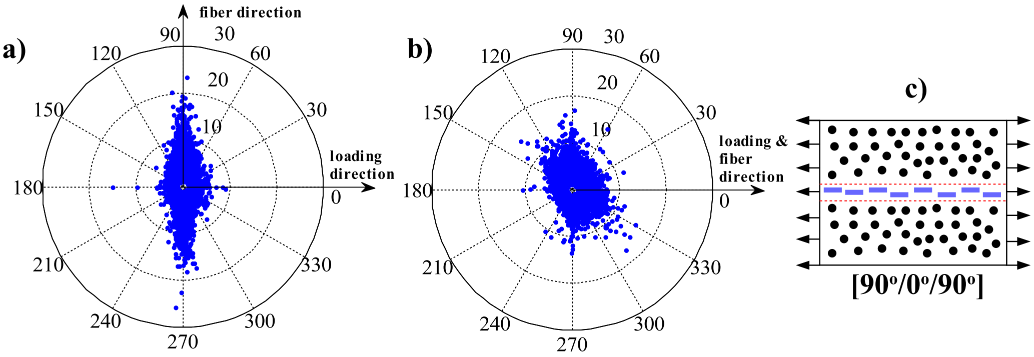

FIGURE 5.19: Void aspect ratio vs. void orientation angle in a) shell and b) core regions of fatigue loaded transverse specimen. Laminate representation analogy of transverse specimen is presented in c) for an interpretation guideline of void orientation angle.

damage or fluctuation of the gray level. The majority of voids with high volume in the shell layers are oriented at 0^o, longitudinal to the fiber orientation as well as to the applied load direction. This signifies that the voids, notably with high volumes, are located along fiber interface in the form of fiber/matrix interfacial debonding. These results are consistent with the aspect ratio analyses performed previously. In terms of evolution, the damage increase shows little evolution in the first 0% to 50%. However it evolves more significantly in the second half of the total fatigue life. It is important to notice that this evolution corresponds to the dynamic modulus evolution given in Fig. 5.7. If one considers the change in the total void volume ΔV with respect to the initial void volume, one can obtain that $\Delta V_{50\%N_f} < 0.5\%$, $\Delta V_{75\%N_f} = 1.3\%$ and $\Delta V_{100\%N_f} = 2.5\%$. This evolution agrees very well with the dynamic modulus evolution in the final stage. However the μCT analyses were not able to capture the damage evolution at the early stage of fatigue life. This is most probably due to the fact that opening of the interface above the resolution limit is needed to make it possible to be detected by the μCT analyses.

In terms of spatial distribution of the damage, based on the macroscopic characterization technique discussed in Section 5.3.1.2, the damage is preferentially diffused over the entire specimen. However, based on the microscopic observation by μCT technique, though the diffuse damage is observed, the damage level between different locations inside the specimen is not necessarily the same. Quantification of the local fiber density and its effects on the fiber/matrix interfacial debonding process is underway and will be the subject of a forthcoming paper.

Finally, it can be summarized that the observed voids can be associated in a large extent to the fiber/matrix interfacial debonding, complete or partial depending on the local configuration of the fibers. However, it is difficult to quantify the degree of interfacial debonding as the fiber length is not unique. Indeed, fiber length variability is developed due to the injection process. Matrix microcracks at high stress level have been observed but do not seems to be dominant in the damage process for dry as molded PA66/GF30.

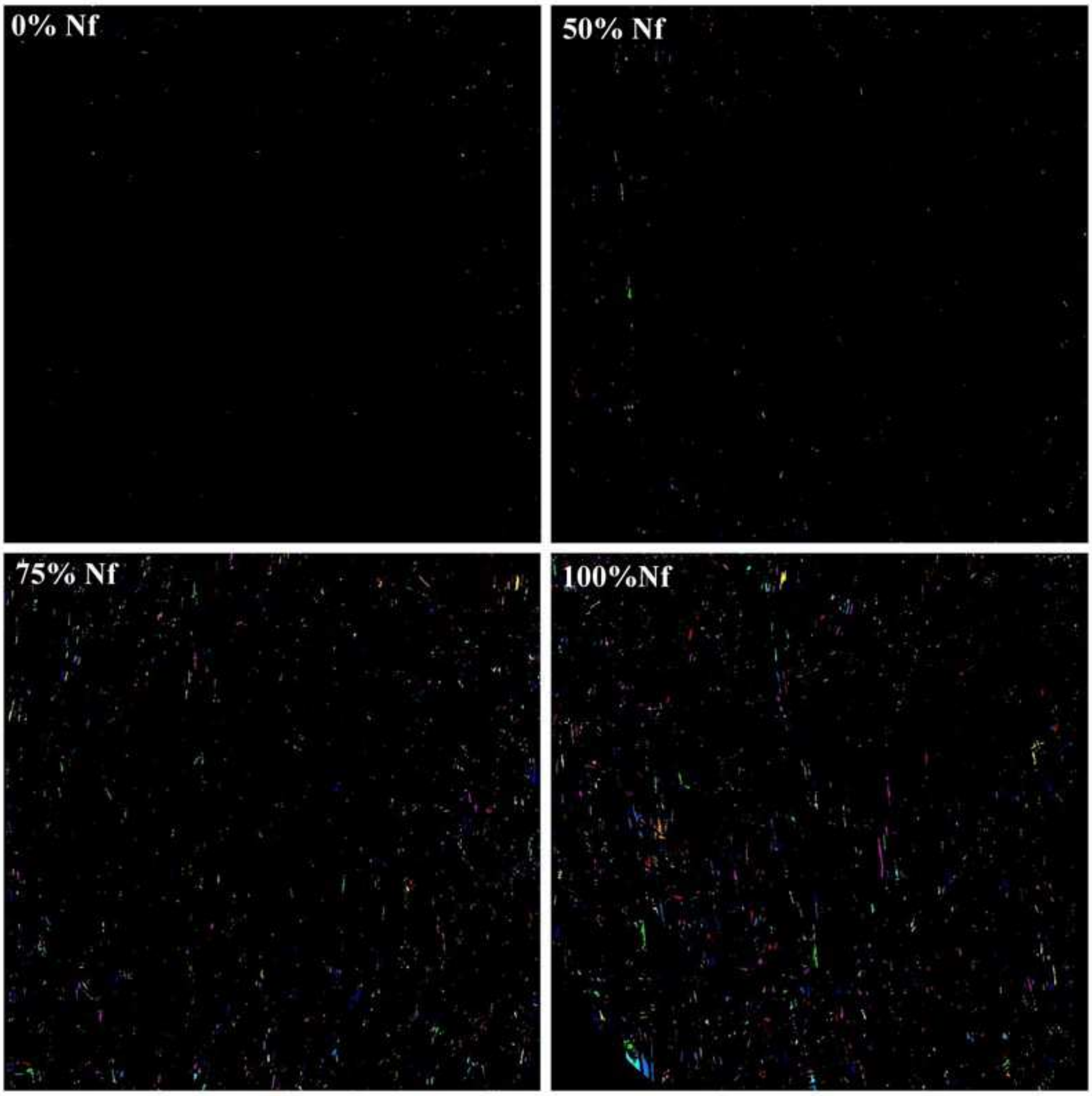

FIGURE 5.20: Label of images of voids in a reference plane of μCT volume of specimens fatigue loaded up to several percentages of fatigue life. The voids are represented by small objects attributed to different colors. It shows that the damage is diffuse and the number of damage increases with cycles.

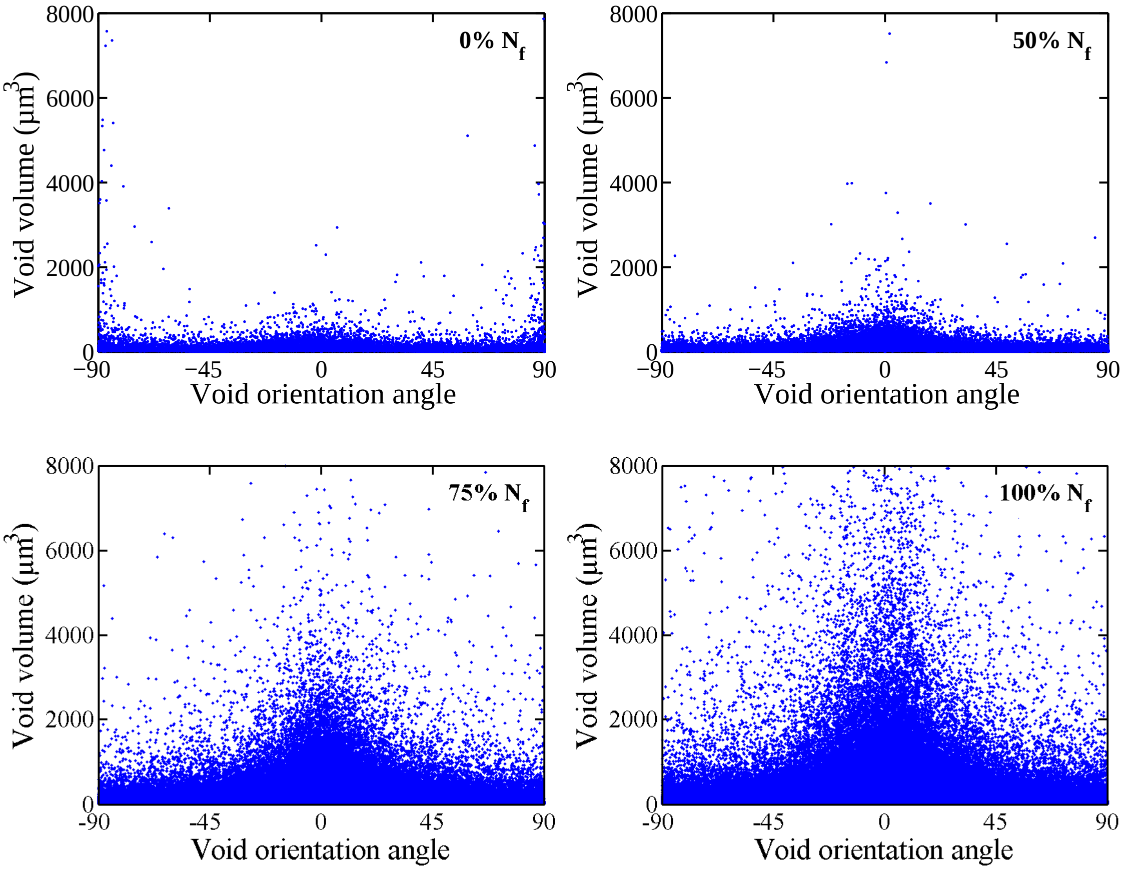

FIGURE 5.21: Void orientation angle vs. void volume graphs of the upper shell layer of longitudinal specimens that have been fatigue loaded up to several percentages of fatigue life (N_f) at maximum stress level of 60% σ_u.

5.4 Concluding remarks

The macroscopic and microscopic fatigue damage indicators of PA66/GF30 have been studied. The experimental results related to the evolution of dynamic modulus, strain, temperature and energy dissipation are important to evaluate the damage evolution. The dynamic modulus can be used as a damage indicator, though in high stress level it may overpredict the damage evolution due to the high viscous effect contribution of the composite.

Based on thermography analysis on PA66/GF30 surface, diffuse damage occurs over the entire specimen. However, the microscopic observation by μCT technique states that the diffuse damage does not necessarily exhibit the same level between different locations inside the specimen.

The μCT analysis shows that the damage is mainly developed along fiber interface in the form of fiber/matrix interfacial debonding, except at the core layer of transverse specimen where matrix microcrack with preferential direction transversely to the applied load is dominant due to the locally high stress concentration.

The μCT results also demonstrate that the damage continuously increases during fatigue loading. However, the damage evolution occurs more significantly in the second half of the fatigue life. Despite high resolutions used in this work, detection of fiber/matrix interfacial debonding in the early stages of fatigue life was difficult. Observation with higher resolution is then required to further investigate the damage mechanisms in these early stages.

CHAPTER 6

General conclusions and further work

General conclusions

The current work was focused on extensive experimental approaches aimed for identifying damage behavior of PA66/GF30 under monotonic and fatigue loading. Prior damage investigation, the microstructure characteristics and overall behavior of the material were investigated.

It was observed that PA66/GF30 exhibit an anisotropic behavior due to the skin-shell-transition-core microstructrue formation developed along the PA66/GF30 thickness. Moreover, the strain rate, temperature and relative humidity content highly influence the mechanical properties of PA66/GF30. The polyamide-66 matrix and PA66/GF30 also exhibit highly viscous behavior. During tensile and fatigue loading, this viscous behavior is coupled with the occurrence of damage. However, by the volume change, thermography and tensile test with full releases techniques, it was difficult to separate the viscous and damage contributions. The tensile test with partial releases produces approximately a reliable result related to the damage level as the viscous effect is suppressed in this test though the real occurring of the damage inside the material remains unknown.

To reveal the real damage behavior of PA66/GF30, in situ SEM investigation technique with variation of relative humidity conditions of the material under monotonic loading was employed. Experimental results demonstrated that the damage are developed inside the material. Relative humidity conditions strongly impact the damage mechanisms in terms of their level and chronology. The damage in RH = 0% specimen initiates at significantly higher load level than those in RH = 50% and 100% specimens. The higher relative humidity conditions also results in higher damage level.

It was observed that the predominant damage mechanisms for RH = 0% specimen are fiber/matrix debonding at fiber ends and fiber sides, fiber breakages and brittle matrix cracks. RH = 50% and 100% specimens exhibit almost the same predominant damage mechanisms, though damage level between both RH contents is essentially different. For both RH contents, the predominant damage mechanisms are fiber/matrix debonding at fiber ends and fiber sides, accompanied with locally strained matrix zone around the debonded fibers and ductile matrix microcracks. Matrix deformation bands are observed frequently in RH = 100% specimen but this occurrence is not dominant in RH = 50% specimen. Comparisons with μCT results indicated that the observations of in situ specimens at the surface matched suitably with that observed inside the specimen for dry and humid specimens.

Based on such observations, general damage chronologies have been proposed as the damage initiates at fiber ends and more generally at locations where fibers are relatively close to each other due to the generation of local stress concentrations. Afterwards, the interfacial decohesions further propagate along the fiber/matrix interface. At high relative flexural stress, matrix microcracks can develop and propagate, leading to the damage accumulation and then final failure. Besides the previous forms of mechanisms, the damage also initiates in the form of fiber breakages (RH=0%). Due to the high ductility of the matrix in humid conditions, the interfacial decohesions in RH = 50% and 100% specimens are also accompanied by a locally strained zone around the fiber. Moreover, while the matrix microcracks in RH=0% tend to propagate in a brittle way, the ones in RH = 50% and 100% tend to propagate in a ductile mode, accompanied with high matrix deformation bands (for RH = 100%).

The study has been extended to fatigue damage behavior. For the current fatigue damage study, only dry as molded material has been analyzed. The macroscopic and microscopic fatigue damage behavior of PA66/GF30 have been studied. It was shown that the experimental results related to the evolution of dynamic modulus, strain, temperature and energy dissipation are important to evaluate the damage evolution. The dynamic modulus can be used as a damage indicator, though in high stress level it may overpredict the damage evolution due to the high viscous effect contribution of the composite.

Based on thermography analysis on PA66/GF30 surface, diffuse damage occurs over the entire specimen. However, the microscopic observation by μCT technique stated that the diffuse damage does not necessarily exhibit the same level between different locations inside the specimen.

The μCT analysis showed that the damage is mainly developed along fiber interface in the form of fiber/matrix interfacial debonding, except at the core layer of transverse specimen where matrix microcrack with preferential direction transversely to the applied load is dominant due to the locally high stress concentration.

The μCT results also demonstrated that the damage continuously increases during fatigue loading. However, the damage evolution occurs more significantly in the second half of the fatigue life. Despite high resolutions used in this work, detection of fiber/matrix interfacial debonding in the early stages of fatigue life was difficult. Observation with higher resolution is then required to further investigate these early stages.

From the results of damage investigation under monotonic and fatigue loading of dry PA66/GF30, it has been indicated that both monotonic and fatigue loading exhibit the same damage mechanisms, with fiber/matrix interfacial debonding as the principal damage mechanisms. Few fiber breakages have also been noticed in both loading conditions though this mechanism is not considered as the main damage mechanism that can highly influence the mechanical behavior and properties of the composite. Moreover, in high stress level, matrix microcracks, with preferential direction perpendicular to the applied load direction, have been observed in both monotonic and fatigue loading conditions.

Since the damage mechanisms in dry as molded condition in both monotonic and fatigue loading are equivalent, the extrapolation to the humid condition is therefore proposed. This has been supported by the results of H. Rolland (PhD student), among them is [Rolland 2014], which demonstrate that the damage mechanisms in humid condition during monotonic and fatigue loading are equivalent and occur according to similar chronology.

Further work

A challenging topic in short fiber reinforced thermoplastics would be to develop reliable and accurate predictive models integrating the damage mechanisms, their initiation and kinetics. However, an extensive bibliographic review on reinforced thermoplastics shows that no modeling approach proposes unified consideration of the whole factors affecting the overall behavior and strength, i.e. composite microstructure, damage mechanisms, polymer rheology, hygrothermal conditions, loading level and paths, etc. [Nouri 2009a, Launay 2011, Kammoun 2011b, Meraghni 2011, Nouri 2013, Launay 2013b].

The current experimental findings on the physical aspect of damage, together with the prospective results of the ongoing work by H. Rolland (PhD student) which focuses on the fatigue damage behavior of humid PA66/GF30 under constant and variable amplitude loading conditions, will be implemented into a predictive micromechanical model towards multiaxial fatigue loading. The modeling task is currently undertaken by N. Despringre (PhD student).

The currently developed micromechanical model [Desrumaux 2000, Jendli 2009] will be extended to include the evolution of damage which integrates fiber/matrix interface damage kinetic coupled with the viscous rheology of the polyamide matrix in relation with the PA66/GF30 microstructure. A particular attention has to be devoted to the impact of the moisture content on the overall mechanical properties of the matrix and to the properties of the fiber/matrix interface to be able to accurately predict the occurrence of damage in PA66/GF30. In this sense, the obtained experimental results would constitute a significant contribution for the on-going modeling work.

The fatigue damage modeling on PA66/GF30 is derived from the Mori-Tanaka model, considering fiber, coating and matrix phases along with damage [Despringre 2014]. As described in Fig. 6.1, the damage scenario can be summarized as follows:

i. Due to the applied load, the damage is initiated and accumulated in a localized viscoelastic coating zone at the fiber interface.

ii. As the damage in coating zone accumulates, the average stress an thus the stress in the viscoelastic matrix increases, which leads to an occurring of matrix crack.

iii. In the final step of damage, local stress in elastic fiber could highly increases and generates fiber breakage. Due to the local stress, fiber failure may occur prior to (or concurrently with) the previously discussed damage mechanisms, especially for PA66/GF30 with low relative humidity content.

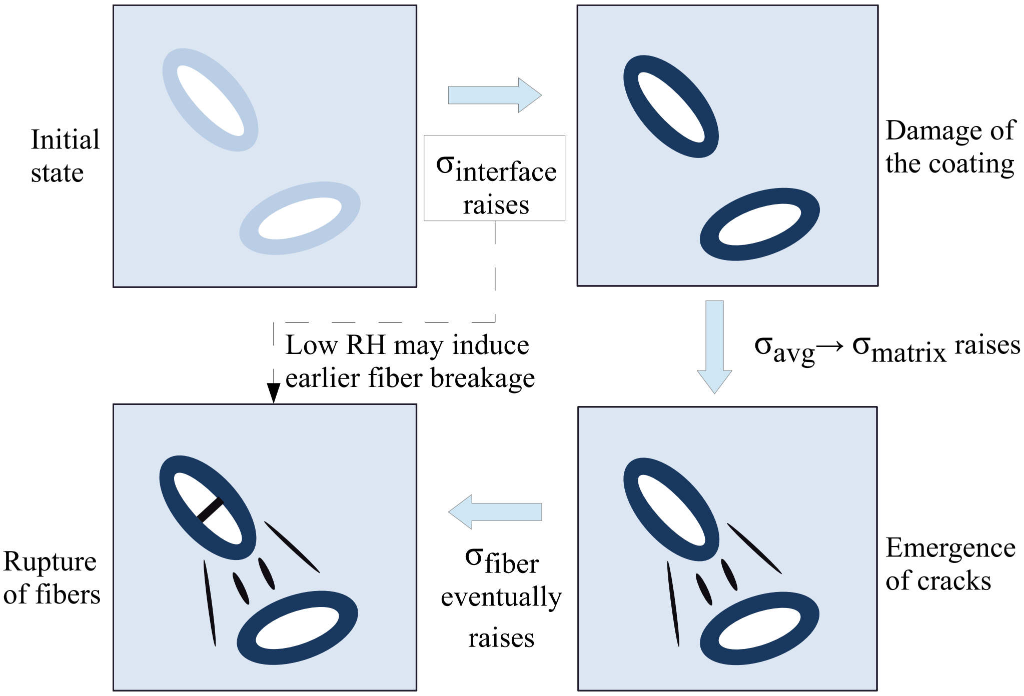

FIGURE 6.1: Proposed scenario of damage modeling in PA66/GF30 [Despringre 2014].

However, it should be noted that the damage mechanisms in the current study are only valid for unnotched specimens under unidirectional macroscopic applied loading conditions. Therefore, implementing the current experimental results for damage modeling of specimens with local macroscopic stress concentration (notched) [Sonsino 2008] and multiaxial loading conditions should be taken carefully. Moreover, the current fatigue damage investigation is only valid for specimens fatigue loaded at 3 Hz frequency. Extending the current experimental results for fatigue damage modeling of specimens loaded at higher frequency, where the matrix self heating starts to be dominant, requires specific analysis.

Bibliography

[Advani 1987] S G Advani and C L Tucker. *The use of tensors to describe and predict fiber orientation in short fiber composites*. Journal of Rheology, vol. 31, 1987. (Cited on pages 47 and 48.)

[Agassant 1991] J.-F. Agassant, P. Avenas, J-Ph. Sergent and P. J. Carreau. Polymer processing: Principles and modeling. Carl Hanser Verlag, Munich, 1991. (Cited on page 46.)

[Akay 1994] M Akay. *Moisture absorption and its influence on the tensile properties of glass-fibre reinforced polyamide 6,6*. Polymers and Polymer Composites, vol. 2, no. 6, pages 349–354, 1994. (Cited on page 90.)

[Alcoutlabi 2003] Mataz Alcoutlabi and J. J. Martinez-Vega. *Modeling of the viscoelastic behavior of amorphous polymers by the differential and integration fractional method: the relaxation spectrum H(τ)*. Polymer, vol. 44, no. 23, pages 7199–7208, November 2003. (Cited on page 74.)

[Arieby 2007] R Arieby. *Caractérisation mécanique et modélisation thermodynamique du comportement anisotrope du polyéthylène à haute densité. Intégration des effets d'endommagement*. PhD thesis, INPL Nancy, 2007. (Cited on page 62.)

[Arif 2014a] M.F. Arif, F Meraghni, Y Chemisky, N Despringre and G Robert. *In situ damage mechanisms investigation of PA66/GF30 composite: Effect of relative humidity*. Composites Part B: Engineering, vol. 58, no. 0, pages 487–495, November 2014. (Cited on pages 62 and 87.)

[Arif 2014b] M.F. Arif, N. Saintier, F. Meraghni, J. Fitoussi, Y. Chemisky and G. Robert. *Multiscale fatigue damage characterization in short glass fiber reinforced polyamide-66*. Composites Part B: Engineering, no. 0, pages –, 2014. (Cited on pages 49 and 87.)

[Awaja 2011] Firas Awaja, Minh-Tam Nguyen, Shengnan Zhang and Benedicta Arhatari. *The investigation of inner structural damage of UV and heat degraded polymer composites using X-ray micro CT*. Composites Part A: Applied Science and Manufacturing, vol. 42, no. 4, pages 408–418, April 2011. (Cited on page 86.)

[Babout 2001] L. Babout, E. Maire, J.Y. Buffière and R. Fougères. *Characterization by X-ray computed tomography of decohesion, porosity growth and coalescence in model metal matrix composites*. Acta Materialia, vol. 49, no. 11, pages 2055–2063, June 2001. (Cited on page 86.)

[Barbouchi 2007] S. Barbouchi, V. Bellenger, A. Tcharkhtchi, Ph. Castaing and T. Jollivet. *Effect of water on the fatigue behaviour of a pa66/glass fibers composite material*. Journal of Materials Science, vol. 42, no. 6, pages 2181–2188, February 2007. (Cited on pages 109, 111 and 112.)

[Barré 1994] S. Barré and M.L. Benzeggagh. *On the use of acoustic emission to investigate damage mechanisms in glass-fibre-reinforced polypropylene*. Composites Science and Technology, vol. 52, no. 3, pages 369–376, January 1994. (Cited on page 84.)

[Bellenger 2006] V. Bellenger, A. Tcharkhtchi and Ph. Castaing. *Thermal and mechanical fatigue of a PA66/glass fibers composite material*. International Journal of Fatigue, vol. 28, no. 10, pages 1348–1352, October 2006. (Cited on pages xv, 111 and 112.)

[Ben Cheikh Larbi 2006] A. Ben Cheikh Larbi, K. Sai, H. Sidhom and D. Baptiste. *Constitutive Model of Micromechanical Damage to Predict Reduction in Stiffness of a Fatigued SMC Composite*. Journal of Materials Engineering and Performance, vol. 15, no. 5, pages 575–580, October 2006. (Cited on pages 66 and 117.)

[Bergeret 2001] A. Bergeret, I. Pires, M.P. Foulc, B. Abadie, L. Ferry and A. Crespy. *The hygrothermal behaviour of glass-fibre-reinforced thermoplastic composites: a prediction of the composite lifetime*. Polymer Testing, vol. 20, no. 7, pages 753–763, January 2001. (Cited on page 78.)

[Bergeret 2009] A Bergeret, L Ferry and P Ienny. *Influence of the fibre/matrix interface on ageing mechanisms of glass fibre reinforced thermoplastic composites (PA-6,6, PET, PBT) in a hygrothermal environment*. Polymer Degradation and Stability, vol. 94, no. 9, pages 1315–1324, September 2009. (Cited on page 78.)

[Bernasconi 2007] A. Bernasconi, P. Davoli, A Basile and A Filippi. *Effect of fibre orientation on the fatigue behaviour of a short glass fibre reinforced polyamide-6*. International Journal of Fatigue, vol. 29, no. 2, pages 199–208, February 2007. (Cited on pages 46 and 69.)

[Bernasconi 2008] Andrea Bernasconi, F. Cosmi and D. Dreossi. *Local anisotropy analysis of injection moulded fibre reinforced polymer composites*. Composites Science and Technology, vol. 68, no. 12, pages 2574–2581, September 2008. (Cited on page 49.)

[Bernasconi 2009] A. Bernasconi and Robb M. Kulin. *Effect of frequency upon fatigue strength of a short glass fiber reinforced polyamide 6: A superposition method based on cyclic creep parameters*. Polymer Composites, vol. 30, no. 2, pages 154–161, February 2009. (Cited on pages xv, 110 and 111.)

[Bernasconi 2012] Andrea Bernasconi, F. Cosmi and P.J. Hine. *Analysis of fibre orientation distribution in short fibre reinforced polymers: A comparison between optical and tomographic methods*. Composites Science and Technology, vol. 72, no. 16, pages 2002–2008, November 2012. (Cited on page 49.)

[Bohse 2000] J Bohse. *Acoustic emission characteristics of micro-failure processes in polymer blends and composites*. Composites Science and Technology, vol. 60, no. 8, pages 1213–1226, June 2000. (Cited on page 84.)

[Bourmaud 2013] a. Bourmaud, G. Ausias, G. Lebrun, M.-L. Tachon and C. Baley. *Observation of the structure of a composite polypropylene/flax and damage mechanisms under stress*. Industrial Crops and Products, vol. 43, pages 225–236, May 2013. (Cited on page 83.)

[Bradley 1995] W. L. Bradley and T. S. Grant. *The effect of the moisture absorption on the interfacial strength of polymeric matrix composites*. Journal of Materials Science, vol. 30, no. 21, pages 5537–5542, 1995. (Cited on page 83.)

[Buffière 1999] J.-Y Buffière, E Maire, P Cloetens, G Lormand and R Fougères. *Characterization of internal damage in a MMCp using X-ray synchrotron phase contrast microtomography*. Acta Materialia, vol. 47, no. 5, pages 1613–1625, March 1999. (Cited on page 86.)

[Bull 2013] D.J. Bull, L. Helfen, I. Sinclair, S.M. Spearing and T. Baumbach. *A comparison of multi-scale 3D X-ray tomographic inspection techniques for assessing carbon fibre composite impact damage*. Composites Science and Technology, vol. 75, pages 55–61, February 2013. (Cited on page 86.)

[Carmona 2009] V Carmona. *Étude de l'endommagement de matériaux composites par tomographie X et émission acoustique*. PhD thesis, INSA de Lyon, 2009. (Cited on pages xiii, 50 and 51.)

[Carrascal 2005] I Carrascal, J.A. Casado, J.A. Polanco and F. Gutiérrez-Solana. *Absorption and diffusion of humidity in fiberglass-reinforced polyamide*. Polymer Composites, vol. 26, no. 5, pages 580–586, October 2005. (Cited on page 78.)

[Casado 2006] JA Casado, F. Gutiérrez-Solana, J.A. Polanco and I. Carrascal. *The assessment of fatigue damage on short-fiber-glass reinforced polyamides (PA) through the surface roughness evolution*. Polymer Composites, vol. 27, no. 4, pages 349–359, August 2006. (Cited on pages 114 and 115.)

[Chanda 2007] M Chanda and S K Roy. Plastics Technology Handbook. CRC Press, 2007. (Cited on pages xiv, 42, 79 and 80.)

[Chateau 2011] C. Chateau, L. Gélébart, M. Bornert, J. Crépin, E. Boller, C. Sauder and W. Ludwig. *In situ X-ray microtomography characterization of damage in SiCf/SiC minicomposites*. Composites Science and Technology, vol. 71, no. 6, pages 916–924, April 2011. (Cited on page 86.)

[Chung 2002] D H Chung and T H Kwon. *Fiber orientation in the processing of polymer composites*. Korea-Australia Rheology Journal, vol. 14, no. 4, pages 175–188, 2002. (Cited on page 47.)

[Clarke 1995] A.R. Clarke, G. Archenhold and N.C. Davidson. *A novel technique for determining the 3D spatial distribution of glass fibres in polymer composites*. Composites Science and Technology, vol. 55, no. 1, pages 75–91, January 1995. (Cited on page 46.)

[Cosmi 2013] F. Cosmi and A. Bernasconi. *Micro-CT investigation on fatigue damage evolution in short fibre reinforced polymers*. Composites Science and Technology, vol. 79, pages 70–76, April 2013. (Cited on pages 87 and 118.)

[Cunha 2000] A.M. Cunha and S. Fakirov. Structure development during polymer processing. Nato Science Series, 2000. (Cited on page 46.)

[Dally 1969] J W Dally and D H Carrillo. *Fatigue behavior of glass-fiber fortified thermoplastics*. Polymer Engineering & Science, vol. 9, no. 6, pages 434–444, 1969. (Cited on page 113.)

[De Monte 2010a] M. De Monte, E. Moosbrugger and Marino Quaresimin. *Influence of temperature and thickness on the off-axis behaviour of short glass fibre reinforced polyamide 6.6 - cyclic loading*. Composites Part A: Applied Science and Manufacturing, vol. 41, no. 10, pages 1368–1379, October 2010. (Cited on pages 69, 110 and 117.)

[De Monte 2010b] M. De Monte, E. Moosbrugger and Marino Quaresimin. *Influence of temperature and thickness on the off-axis behaviour of short glass fibre reinforced polyamide 6.6 - Quasi-static loading*. Composites Part A: Applied Science and Manufacturing, vol. 41, no. 7, pages 859–871, July 2010. (Cited on pages 46, 49, 110 and 117.)

[Despringre 2014] N. Despringre, Y. Chemisky, M.F. Arif, G. Robert and F. Meraghni. *Multi-scale viscoelastic damage model of short glass fiber reinforced polyamide-66 under highcycle fatigue*. In 16th European Conference on Composite Materials (Accepted), Seville-Spain, 2014. (Cited on pages xvi, 137 and 138.)

[Desrumaux 2000] F Desrumaux, F Meraghni and ML Benzeggagh. *Micromechanical modelling coupled to a reliability approach for damage evolution prediction in composite materials*. Applied Composite Materials, vol. 7, pages 231–250, 2000. (Cited on pages 30 and 137.)

[Dray 2006] D Dray. *Prédiction des propriétés thermo-élastiques d'un composite injecté et chargé de fibres courtes*. PhD thesis, Arts et Métiers ParisTech, 2006. (Cited on page 46.)

[Dwight 2000] D W Dwight. *Glass fiber reinforcements*. Comprehensive composite materials, pages 231–261, 2000. (Cited on page 40.)

[Eberhardt 2001] C N Eberhardt and Ashley Clarke. *Fibre-orientation measurements in short-glass-fibre composites. Part I: automated, high-angular-resolution measurement by confocal microscopy*. Composites Science and Technology, vol. 61, no. 10, pages 1389–1400, August 2001. (Cited on pages 46 and 47.)

[Eberhardt 2002] C N Eberhardt and a R Clarke. *Automated reconstruction of curvilinear fibres from 3D datasets acquired by X-ray microtomography.* Journal of microscopy, vol. 206, no. Pt 1, pages 41–53, April 2002. (Cited on page 49.)

[Erhard 2006] G Erhard. Designing with Plastics. Hanser Gardner Publications, 2006. (Cited on page 82.)

[Esmaeillou 2011] B Esmaeillou, J. Fitoussi, A Lucas and A. Tcharkhtchi. *Multi-scale experimental analysis of the tension-tension fatigue behavior of a short glass fiber reinforced polyamide composite*. Procedia Engineering, vol. 10, pages 2117–2122, January 2011. (Cited on pages xv, 115 and 116.)

[Esmaeillou 2012a] B Esmaeillou, P Fereirra, V. Bellenger and A. Tcharkhtchi. *Fatigue damage initiation of a PA66/glass fibers composite material.* Journal of Applied Polymer Science, vol. 125, no. 5, pages 4007–4014, September 2012. (Cited on page 115.)

[Esmaeillou 2012b] B Esmaeillou, P Ferreira, V. Bellenger and A. Tcharkhtchi. *Fatigue behavior of polyamide 66/glass fiber under various kinds of applied load.* Polymer Composites, vol. 33, no. 4, pages 540–547, April 2012. (Cited on pages 111, 112 and 115.)

[European Environment Agency 2012] European Environment Agency. *Monitoring CO2 emissions from new passenger cars in the EU: summary of data for 2012.* 2012. (Cited on page 34.)

[Fidan 2012] Sinan Fidan, Tamer Sınmazçelik and Egemen Avcu. *Internal damage investigation of the impacted glass/glass+aramid fiber reinforced composites by micro-computerized tomography*. NDT & E International, vol. 51, pages 1–7, October 2012. (Cited on page 86.)

[Fitoussi 2013] Joseph Fitoussi, Michel Bocquet and Fodil Meraghni. *Effect of the matrix behavior on the damage of ethylene-propylene glass fiber reinforced composite subjected to high strain rate tension*. Composites Part B: Engineering, vol. 45, no. 1, pages 1181–1191, February 2013. (Cited on page 117.)

[Gautier 1999] L Gautier, B Mortaigne and V Bellenger. *Interface damage study of hydrothermally aged glass-fibre-reinforced polyester composites*. Composites Science and Technology, vol. 59, no. 16, pages 2329–2337, December 1999. (Cited on page 83.)

[Günzel 2012] Stephan Günzel, Stefan Hickmann, Christian Wittemeyer and Volker Trappe. *Effects of Fiber Orientation and Moisture on the Crack Growth in Short Glass Fiber Reinforced Polyamide*. Advanced Engineering Materials, vol. 14, no. 10, pages 867–872, October 2012. (Cited on pages 85, 86 and 87.)

[Hand 1961] George Louis Hand. *A theory of anisotropic fluids*. PhD thesis, Cambridge Univ Press, 1961. (Cited on page 47.)

[Hassan 2011] A. Hassan, N. M. Salleh, R. Yahya and M. R. K. Sheikh. *Fiber length, thermal, mechanical, and dynamic mechanical properties of injection-molded glass-fiber/polyamide 6,6: plasticization effect*. Journal of Reinforced Plastics and Composites, vol. 30, no. 6, pages 488–498, April 2011. (Cited on pages 74, 83, 85 and 90.)

[Hassan 2012] Aziz Hassan, Normasmira A. Rahman and Rosiyah Yahya. *Moisture absorption effect on thermal, dynamic mechanical and mechanical properties of injection-molded short glass-fiber/polyamide 6,6 composites*. Fibers and Polymers, vol. 13, no. 7, pages 899–906, September 2012. (Cited on page 74.)

[Horst 1996] J. J. Horst and J. L. Spoormaker. *Mechanisms of fatigue in short glass fiber reinforced polyamide 6*. Polymer Engineering & Science, vol. 36, no. 22, pages 2718–2726, November 1996. (Cited on pages xv, 69, 110, 111 and 113.)

[Horst 1997a] J. J. Horst. *Influence of fibre orientation on fatigue of short glassfibre reinforced Polyamide*. PhD thesis, TUDelft, 1997. (Cited on page 46.)

[Horst 1997b] J. J. Horst and J. L. Spoormaker. *Fatigue fracture mechanisms and fractography of short-glassfibre-reinforced polyamide 6*. Journal of materials science, vol. 32, no. 14, pages 3641–3651, 1997. (Cited on pages xv, 109, 113 and 114.)

[Hosokawa 2013] Akihide Hosokawa, David S. Wilkinson, Jidong Kang, Masakazu Kobayashi and Hiroyuki Toda. *Void growth and coalescence in model materials investigated by high-resolution X-ray microtomography*. International Journal of Fracture, vol. 181, no. 1, pages 51–66, March 2013. (Cited on page 118.)

[Hufenbach 2012] W. Hufenbach, R. Böhm, M. Gude, M. Berthel, A. Hornig, S. Ručevskis and M. Andrich. *A test device for damage characterisation of composites based on in situ computed tomography*. Composites Science and Technology, vol. 72, no. 12, pages 1361–1367, July 2012. (Cited on page 86.)

[ID19 ESRF] ID19 ESRF. *www.esrf.eu/UsersAndScience/Experiments/Imaging/ID19*. (Cited on pages 5, 52 and 90.)

[Isaac 2008] A. Isaac, F. Sket, W. Reimers, B. Camin, G. Sauthoff and A.R. Pyzalla. *In situ 3D quantification of the evolution of creep cavity size, shape, and spatial orientation using synchrotron X-ray tomography*. Materials Science and Engineering: A, vol. 478, no. 1-2, pages 108–118, April 2008. (Cited on page 118.)

[Jeffery 1922] G. B. Jeffery. *The Motion of Ellipsoidal Particles Immersed in a Viscous Fluid*. Proceedings of the Royal Society A: Mathematical, Physical and Engineering Sciences, vol. 102, no. 715, pages 161–179, November 1922. (Cited on page 47.)

[Jegou 2012] L. Jegou. *Caractérisation rapide des propriétés en fatigue d'un polymère renforcé par des fibres courtes, pour une application automobile*. PhD thesis, Université de Bretagne Occidentale, 2012. (Cited on pages xv, 87 and 118.)

[Jendli 2009] Zouhaier Jendli, Fodil Meraghni, Joseph Fitoussi and Didier Baptiste. *Multi-scales modelling of dynamic behaviour for discontinuous fibre SMC composites*. Composites Science and Technology, vol. 69, no. 1, pages 97–103, January 2009. (Cited on pages 30 and 137.)

[Jia 1998] Nanying Jia and VA Kagan. *Effects of time and temperature on the tension-tension fatigue behavior of short fiber reinforced polyamides*. Polymer composites, vol. 19, no. 4, 1998. (Cited on page 109.)

[Kammoun 2011a] S. Kammoun. *Micromechanical modeling of the progressive failure in short glass-fiber reinforced thermoplastics*. PhD thesis, Université catholique de Louvain, 2011. (Cited on page 61.)

[Kammoun 2011b] S. Kammoun, I. Doghri, L. Adam, G. Robert and L. Delannay. *First pseudo-grain failure model for inelastic composites with misaligned short fibers*. Composites Part A: Applied Science and Manufacturing, vol. 42, no. 12, pages 1892–1902, December 2011. (Cited on page 137.)

[Klimkeit 2011] B. Klimkeit, S. Castagnet, Y. Nadot, A. El Habib, G. Benoit, S. Bergamo, C. Dumas and S. Achard. *Fatigue damage mechanisms in short fiber reinforced PBT+PET GF30*. Materials Science and Engineering: A, vol. 528, no. 3, pages 1577–1588, January 2011. (Cited on pages 46, 108 and 116.)

[Ladeveze 1992] P Ladeveze and E Le Dantec. *Damage modelling of the elementary ply for laminated composites*. Composites Science and Technology, vol. 43, no. 3, pages 257–267, 1992. (Cited on pages 21, 116 and 120.)

[Laiarinandrasana 2010] L. Laiarinandrasana, T. F. Morgeneyer, H. Proudhon and C. Regrain. *Damage of semicrystalline polyamide 6 assessed by 3D X-ray tomography: From microstructural evolution to constitutive modeling*. Journal of Polymer Science Part B: Polymer Physics, vol. 48, no. 13, pages 1516–1525, May 2010. (Cited on page 49.)

[Lambert 2012] J. Lambert, A.R. Chambers, I. Sinclair and S.M. Spearing. *3D damage characterisation and the role of voids in the fatigue of wind turbine blade materials*. Composites Science and Technology, vol. 72, no. 2, pages 337–343, January 2012. (Cited on page 86.)

[Lang 1987] RW Lang, J. a. Manson and R. W. Hertzberg. *Mechanisms of fatigue fracture in short glass fibre-reinforced polymers*. Journal of Materials Science, vol. 22, no. 11, pages 4015–4030, November 1987. (Cited on page 113.)

[Laspalas 2008] M. Laspalas, C. Crespo, M.a. Jiménez, B. García and J.L. Pelegay. *Application of micromechanical models for elasticity and failure to short fibre reinforced composites. Numerical implementation and experimental validation*. Computers & Structures, vol. 86, no. 9, pages 977–987, May 2008. (Cited on page 47.)

[Launay 2011] A Launay, M.H. Maitournam, Y. Marco, I. Raoult and F. Szmytka. *Cyclic behaviour of short glass fibre reinforced polyamide: Experimental study and constitutive equations*. International Journal of Plasticity, vol. 27, no. 8, pages 1267–1293, August 2011. (Cited on pages 74 and 137.)

[Launay 2013a] A Launay, M.H. Maitournam, Y. Marco and I. Raoult. *Multiaxial fatigue models for short glass fiber reinforced polyamide - Part I: Nonlinear anisotropic constitutive behavior for cyclic response*. International Journal of Fatigue, vol. 47, pages 382–389, February 2013. (Cited on page 47.)

[Launay 2013b] A. Launay, Y. Marco, M.H. Maitournam and I. Raoult. *Modelling the influence of temperature and relative humidity on the time-dependent mechanical behaviour of a short glass fibre reinforced polyamide*. Mechanics of Materials, vol. 56, pages 1–10, January 2013. (Cited on pages 74, 83, 90 and 137.)

[Le Saux 2011] Vincent Le Saux, Yann Marco, Sylvain Calloch and Pierre Charrier. *Evaluation of the fatigue defect population in an elastomer using X-ray computed micro-tomography*. Polymer Engineering & Science, vol. 51, no. 7, pages 1253–1263, July 2011. (Cited on page 118.)

[Lee 2002] Yong Lee, Seok Lee, Jae Youn, Kwansoo Chung and Tae Kang. *Characterization of fiber orientation in short fiber reinforced composites with an image processing technique*. Materials Research Innovations, vol. 6, no. 2, pages 65–72, September 2002. (Cited on pages 46 and 47.)

[Lindhagen 1998] J Lindhagen and L Berglund. *Microscopical damage mechanisms in glass fiber reinforced polypropylene*. Journal of Applied Polymer Science, vol. 69, no. 7, pages 1319–1327, August 1998. (Cited on page 83.)

[Little 2012] John Eric Little, Xiaowen Yuan and Mark Ian Jones. *Characterisation of voids in fibre reinforced composite materials*. NDT & E International, vol. 46, pages 122–127, March 2012. (Cited on page 86.)

[Madi 2006] K Madi. *Influence de la morphologie tridimensionnelle des phases sur le comportement mécanique de réfractaires électrofondus*. PhD thesis, Mines ParisTech, 2006. (Cited on pages xiii and 50.)

[Maire 2001a] E Maire, L Babout, J.-Y Buffiere and R Fougeres. *Recent results on 3D characterisation of microstructure and damage of metal matrix composites and a metallic foam using X-ray tomography*. Materials Science and Engineering: A, vol. 319-321, pages 216–219, December 2001. (Cited on page 86.)

[Maire 2001b] E. Maire, J. Y. Buffière, Luc Salvo, Jean Jacques Blandin, Wolfgang Ludwig and J. M. Létang. *On the Application of X-ray Microtomography in the Field of Materials Science*. Advanced Engineering Materials, vol. 3, no. 8, page 539, August 2001. (Cited on page 49.)

[Mallick 2000] P K Mallick. *Particulate and Short Fiber Reinforced Polymer Composites*. In A Kelly and C Zweben, editors, Comprehensive Composite Materials, pages 291–331. Pergamon, Oxford, 2000. (Cited on page 40.)

[Mallick 2004] P. K. Mallick and Y Zhou. *Effect of mean stress on the stress-controlled fatigue of a short E-glass fiber reinforced polyamide-6,6*. International Journal of Fatigue, vol. 26, no. 9, pages 941–946, September 2004. (Cited on pages 69 and 110.)

[McCombe 2012] G.P. McCombe, J. Rouse, R.S. Trask, P.J. Withers and I.P. Bond. *X-ray damage characterisation in self-healing fibre reinforced polymers*. Composites Part A: Applied Science and Manufacturing, vol. 43, no. 4, pages 613–620, April 2012. (Cited on page 86.)

[Megally 2005] A Megally. *Etude et Modélisation de l'orientation de fibres dans des thermoplastiques renforcés*. PhD thesis, Mines ParisTech, 2005. (Cited on page 47.)

[Meraghni 1995] F. Meraghni and M.L. Benzeggagh. *Micromechanical modelling of matrix degradation in randomly oriented discontinuous-fibre composites*. Composites Science and Technology, vol. 55, no. 2, pages 171–186, January 1995. (Cited on page 101.)

[Meraghni 1996] F Meraghni, CJ Blakeman and ML Benzeggagh. *Effect of interfacial decohesion on stiffness reduction in a random discontinuous-fibre composite containing matrix microcracks*. Composites Science and Technology, vol. 56, no. 5, pages 541–555, January 1996. (Cited on page 101.)

[Meraghni 2002] F. Meraghni, F. Desrumaux and M.L. Benzeggagh. *Implementation of a constitutive micromechanical model for damage analysis in glass mat reinforced composite structures*. Composites Science and Technology, vol. 62, no. 16, pages 2087–2097, December 2002. (Cited on page 84.)

[Meraghni 2011] F. Meraghni, H. Nouri, N Bourgeois, C. Czarnota and P. Lory. *Parameters identification of fatigue damage model for short glass fiber reinforced polyamide (PA6-GF30) using digital image correlation*. Procedia Engineering, vol. 10, pages 2110–2116, January 2011. (Cited on pages 66, 117 and 137.)

[Miettinen 2012] Arttu Miettinen, Cris L. Luengo Hendriks, Gary Chinga-Carrasco, E. Kristofer Gamstedt and Markku Kataja. *A non-destructive X-ray microtomography approach for measuring fibre length in short-fibre composites*. Composites Science and Technology, vol. 72, no. 15, pages 1901–1908, October 2012. (Cited on page 49.)

[Moffat 2008] AJ Moffat, P. Wright, J.-Y. Buffière, I. Sinclair and S.M. Spearing. *Micromechanisms of damage in 0° splits in a [90/0]s composite material using synchrotron radiation computed tomography*. Scripta Materialia, vol. 59, no. 10, pages 1043–1046, November 2008. (Cited on page 86.)

[Monson 2008] L Monson, M. Braunwarth and C. W. Extrand. *Moisture absorption by various polyamides and their associated dimensional changes*. Journal of Applied Polymer Science, vol. 107, no. 1, pages 355–363, January 2008. (Cited on page 81.)

[Montesano 2013] John Montesano, Zouheir Fawaz and Habiba Bougherara. *Use of infrared thermography to investigate the fatigue behavior of a carbon fiber reinforced polymer composite*. Composite Structures, vol. 97, pages 76–83, March 2013. (Cited on page 112.)

[Mouhmid 2006] B. Mouhmid, Abdellatif Imad, N. Benseddiq, S. Benmedakhène and A. Maazouz. *A study of the mechanical behaviour of a glass fibre reinforced polyamide 6,6: Experimental investigation*. Polymer Testing, vol. 25, no. 4, pages 544–552, June 2006. (Cited on pages 62, 84 and 85.)

[MSCI 2013] MSCI. *http : //www.msci.com/insights/responsible_investing/chart_of_the_month_which_car_manufacturers_are_best_prepared_to_meet_2015_eu_vehicle_emissions_stand.html*. August 2013. (Cited on page 34.)

[Müller 2013] V Müller, F Dillenberger, B Brylka, T Böhlke, R Glöckner and S Kolling. *Homogenization of elastic properties of short fiber reinforced composites based on micro computed tomography data.* In The 19th International Conference on Composite Materials, Montréal, Canada, 2013. (Cited on page 49.)

[Noda 2001] K Noda, A Takahara and T Kajiyama. *Fatigue failure mechanisms of short glass-fiber reinforced nylon 66 based on nonlinear dynamic viscoelastic measurement.* polymer, vol. 42, pages 5803–5811, 2001. (Cited on pages 111 and 114.)

[Nouri 2009a] H. Nouri, F. Meraghni and P. Lory. *Fatigue damage model for injection-molded short glass fibre reinforced thermoplastics.* International Journal of Fatigue, vol. 31, no. 5, pages 934–942, May 2009. (Cited on pages 21, 66, 117, 120 and 137.)

[Nouri 2009b] Hedi Nouri. *Modélisation et identification de lois de comportement avec endommagement en fatigue polycyclique de matériaux composite a matrice thermoplastique.* PhD thesis, Arts et Métiers ParisTech, 2009. (Cited on pages 46, 67 and 117.)

[Nouri 2013] Hedi Nouri, Christophe Czarnota and Fodil Meraghni. *Experimental Parameters Identification of Fatigue Damage Model for Short Glass Fiber Reinforced Thermoplastics GFRP.* In Mohamed Haddar, Lotfi Romdhane, Jamel Louati and Abdelmajid Ben Amara, editors, Design and Modeling of Mechanical Systems, Lecture Notes in Mechanical Engineering, pages 523–530. Springer Berlin Heidelberg, Berlin, Heidelberg, 2013. (Cited on pages 66, 117 and 137.)

[Ramirez-Jimenez 2004] C.R Ramirez-Jimenez, N Papadakis, N Reynolds, T.H Gan, P Purnell and M Pharaoh. *Identification of failure modes in glass/polypropylene composites by means of the primary frequency content of the acoustic emission event.* Composites Science and Technology, vol. 64, no. 12, pages 1819–1827, September 2004. (Cited on page 84.)

[Rask 2012] Morten Rask, Bo Madsen, Bent F. Sø rensen, Julie L. Fife, Karolina Martyniuk and Erik M. Lauridsen. *In situ observations of microscale damage evolution in unidirectional natural fibre composites.* Composites Part A: Applied Science and Manufacturing, vol. 43, no. 10, pages 1639–1649, October 2012. (Cited on page 86.)

[Redjeb 2007] A Redjeb. *Simulation numérique de l'orientation de fibres en injection de thermoplastique renforcé*. PhD thesis, Mines ParisTech, 2007. (Cited on page 47.)

[Rolland 2014] H. Rolland, N. Saintier and G. Robert. *Damage mechanisms into short glass fiber reinforced thermoplastic during in situ microtomographic tensile tests*. In 16th European Conference on Composite Materials (Accepted), Seville-Spain, 2014. (Cited on page 137.)

[Sato 1984] N Sato, T Kurauchi, S Sato and O Kamigaito. *Mechanism of fracture of short glass fibre-reinforced polyamide thermoplastic*. Journal of materials science, vol. 19, pages 1145–1152, 1984. (Cited on pages 15 and 100.)

[Sato 1991] N. Sato, T Kurauchi, S Sato and O Kamigaito. *Microfailure behaviour of randomly dispersed short fibre reinforced thermoplastic composites obtained by direct SEM observation*. Journal of Materials Science, vol. 26, no. 14, pages 3891–3898, July 1991. (Cited on pages xiv, 62, 83, 84 and 85.)

[Schilling 2005] Paul J. Schilling, BhanuPrakash R. Karedla, Arun K. Tatiparthi, Melody a. Verges and Paul D. Herrington. *X-ray computed microtomography of internal damage in fiber reinforced polymer matrix composites*. Composites Science and Technology, vol. 65, no. 14, pages 2071–2078, November 2005. (Cited on page 86.)

[Schoß ig 2011] Marcus Schoß ig, Armin Zankel, Christian Bierögel, Peter Pölt and Wolfgang Grellmann. *ESEM investigations for assessment of damage kinetics of short glass fibre reinforced thermoplastics - Results of in situ tensile tests coupled with acoustic emission analysis*. Composites Science and Technology, vol. 71, no. 3, pages 257–265, February 2011. (Cited on page 83.)

[Scott 2012] A. E. Scott, I. Sinclair, S. M. Spearing, A. Thionnet and A. R. Bunsell. *Damage accumulation in a carbon/epoxy composite: Comparison between a multiscale model and computed tomography experimental results*. Composites Part A: Applied Science and Manufacturing, vol. 43, no. 9, pages 1514–1522, September 2012. (Cited on page 86.)

[Seignobos 2009] E Seignobos. *Compréhension des mécanismes physiques de fatigue dans le polyamide vierge et renforcé de fibres de verre*. PhD thesis, INSA Lyon, 2009. (Cited on pages 46, 66, 110, 115 and 117.)

[Seltzer 2013] R. Seltzer, C. González, R. Muñoz, J. LLorca and T. Blanco-Varela. *X-ray microtomography analysis of the damage micromechanisms in 3D woven composites under low-velocity impact*. Composites Part A: Applied Science and Manufacturing, vol. 45, pages 49–60, February 2013. (Cited on page 86.)

[Shen 2004] Hongbin Shen, Steven Nutt and David Hull. *Direct observation and measurement of fiber architecture in short fiber-polymer composite foam through micro-CT imaging*. Composites Science and Technology, vol. 64, no. 13-14, pages 2113–2120, October 2004. (Cited on page 49.)

[Sims 2000] G D Sims and W R Broughton. *Glass Fiber Reinforced Plastics-Properties*. In Anthony Kelly and Carl Zweben, editors, Comprehensive Composite Materials, pages 151–197. Pergamon, Oxford, 2000. (Cited on page 40.)

[Sket 2012] F. Sket, R. Seltzer, J.M. Molina-Aldareguía, C. Gonzalez and J. LLorca. *Determination of damage micromechanisms and fracture resistance of glass fiber/epoxy cross-ply laminate by means of X-ray computed microtomography*. Composites Science and Technology, vol. 72, no. 2, pages 350–359, January 2012. (Cited on page 86.)

[Solvay Engineering Plastics 2009] Solvay Engineering Plastics. *Technyl polyamide range for automotive market*. 2009. (Cited on page 36.)

[Sonsino 2008] C.M. Sonsino and E. Moosbrugger. *Fatigue design of highly loaded short-glass-fibre reinforced polyamide parts in engine compartments*. International Journal of Fatigue, vol. 30, no. 7, pages 1279–1288, July 2008. (Cited on pages 69 and 138.)

[SPE] SPE. *http://www.4spepro.org*. SPE Plastic research online, acessed on Feb 2014. (Cited on pages xii and 44.)

[Steinberger 2006] R Steinberger, T. I. Valadas Leitao, E Ladstatter, G Pinter, W Billinger and R. W. Lang. *Infrared thermographic techniques for non-destructive damage characterization of carbon fibre reinforced polymers during tensile fatigue testing*. International Journal of Fatigue, vol. 28, no. 10, pages 1340–1347, October 2006. (Cited on page 112.)

[Stock 2008] S. R. Stock. *Recent advances in X-ray microtomography applied to materials*. International Materials Reviews, vol. 53, no. 3, pages 129–181, May 2008. (Cited on page 49.)

[Suuronen 2012] Jussi-Petteri Suuronen, Aki Kallonen, Marika Eik, Jari Puttonen, Ritva Serimaa and Heiko Herrmann. *Analysis of short fibres orientation in steel fibre-reinforced concrete (SFRC) by X-ray tomography*. Journal of Materials Science, vol. 48, no. 3, pages 1358–1367, October 2012. (Cited on page 49.)

[Szabo 2002] Jeffrey P Szabo and Irvin a Keough. *Method for analysis of dynamic mechanical thermal analysis data using the Havriliak-Negami model*. Thermochimica Acta, vol. 392-393, pages 1–12, September 2002. (Cited on page 74.)

[Tan 2011] K.T. Tan, N. Watanabe and Y. Iwahori. *X-ray radiography and micro-computed tomography examination of damage characteristics in stitched composites subjected to impact loading*. Composites Part B: Engineering, vol. 42, no. 4, pages 874–884, June 2011. (Cited on page 86.)

[Toubal 2006] L Toubal, M Karama and B Lorrain. *Damage evolution and infrared thermography in woven composite laminates under fatigue loading*. International Journal of Fatigue, vol. 28, no. 12, pages 1867–1872, December 2006. (Cited on page 117.)

[Uleck 2006] Kevin R Uleck. *A hybrid model for fatigue life estimation of polymer matrix composites*. PhD thesis, University of Maryland, College Park, 2006. (Cited on page 108.)

[Wilkinson 1998] A N Wilkinson and A J Ryan. Polymer processing and structure development. Kluwer Academic Publishers, 1998. (Cited on pages xii, 45 and 46.)

[Withers 2012] Philip J. Withers and Michael Preuss. *Fatigue and Damage in Structural Materials Studied by X-Ray Tomography*. Annual Review of Materials Research, vol. 42, no. 1, pages 81–103, August 2012. (Cited on page 49.)

[Wright 2010] P. Wright, AJ Moffat, I. Sinclair and S.M. Spearing. *High resolution tomographic imaging and modelling of notch tip damage in a laminated composite*. Composites Science and Technology, vol. 70, no. 10, pages 1444–1452, September 2010. (Cited on page 86.)

[Zhou 2005] Y Zhou and P.K. Mallick. *A non-linear damage model for the tensile behavior of an injection molded short E-glass fiber reinforced polyamide-6,6*. Materials Science and Engineering: A, vol. 393, no. 1-2, pages 303–309, February 2005. (Cited on page 84.)

[Zhou 2006] Y Zhou and P.K. Mallick. *Fatigue performance of an injection-molded short E-glass fiber-reinforced polyamide 6,6. I. Effects of orientation, holes, and weld line*. Polymer Composites, vol. 27, no. 2, pages 230–237, April 2006. (Cited on page 69.)

APPENDIX A

DIC measurement

Digital Image Correlation (DIC) is a non-contact technique employed for evaluation of deformation and strain of a material. The DIC experimental technique involves pattern creation of the material's surfaces on the investigated zone (e.g. gauge length zone). Various types of patterns have been employed, such as lines, grids, dots, and random speckle arrays. The random arrays pattern serves as the most commonly used approaches in DIC. The repeated images of the patterned material's surfaces of a deforming object are acquired using a camera with an acquisition controller, and then stored in a digital form. The collection of images is then analyzed (image correlation process) in order to extract full-field deformation or strain of an object.

In this work, DIC image acquisition and correlation were carried out on the width and thickness surfaces of the specimen. By this method, the strain in three principal directions, i.e. $\varepsilon_{11}, \varepsilon_{22}$ and ε_{33} can be obtained. The DIC experimental setup is illustrated in Fig. A.1. In order to allow the image correlation, spray-gun black and white painting onto the specimen's surfaces were employed to produce a fine random speckle pattern, as shown in Fig. A.2a. The Vic-2D software was employed for the image correlation process. The pattern size of the image correlation was set up to 21×5 pixels. Therefore, the achieved spatial resolution is about 21 pixel. By the current experimental setup, the resolution in terms of the measured strain was 5×10^{-3}. An example of the strain profile after the correlation process can be seen in Fig. A.2b. In the current study, the reported strain is the mean value over the gauge length zone of the specimen.

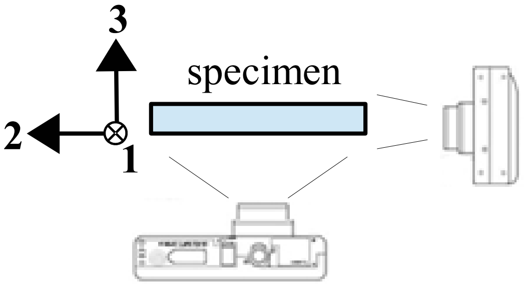

FIGURE A.1: Experimental setup of strain measurement by DIC.

Since the $\varepsilon_{11}, \varepsilon_{22}$ and ε_{33} can be obtained by the current DIC setup, the volume change in the specimen can also be computed. If one considers V_0 and V respectively as the initial and final volumes, L_1, L_2, L_3 and (l_1, l_2, l_3) as the initial and (final) lengths at three principal directions, one can obtain that $V_0 = L_1 \times L_2 \times L_3$ and $V = l_1 \times l_2 \times l_3$.

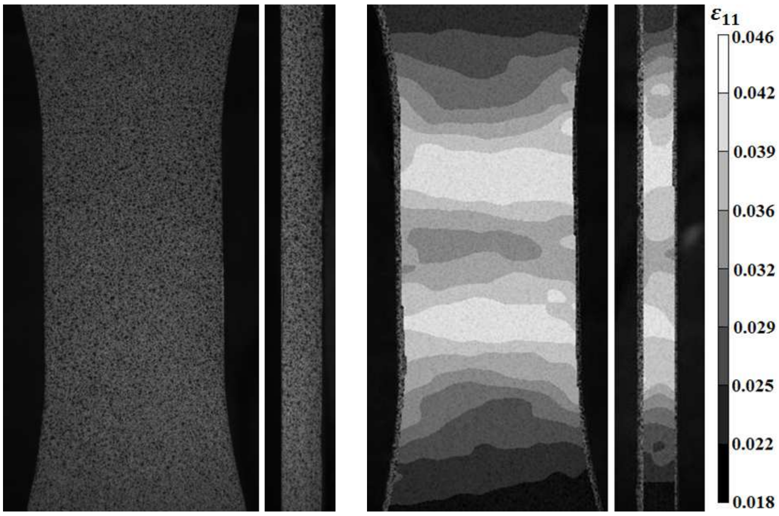

(a) Random speckle patterns (b) Strain profile

FIGURE A.2: DIC analysis on the width and thickness surfaces of the specimen.

The dimensional changes of each principal direction can be expressed as:

$$\begin{aligned} l_1 &= (1+\varepsilon_{11}) \times L_1 \\ l_2 &= (1+\varepsilon_{22}) \times L_2 \\ l_3 &= (1+\varepsilon_{33}) \times L_3 \end{aligned} \tag{A.1}$$

Therefore, V can be expressed as:

$$\begin{aligned} V = l_1 + l_2 + l_3 &= (1+\varepsilon_{11}) \times L_1 \times (1+\varepsilon_{22}) \times L_2 \times (1+\varepsilon_{33}) \times L_3 \\ &\approx (1+\varepsilon_{11}+\varepsilon_{22}+\varepsilon_{33}) \times L_1 \times L_2 \times L_3 \end{aligned} \tag{A.2}$$

Finally, the volume change $\delta V/V$ of the material can be defined as:

$$\begin{aligned} \frac{V-V_0}{V_0} &= \frac{((1+\varepsilon_{11}+\varepsilon_{22}+\varepsilon_{33}) \times L_1 \times L_2 \times L_3) - (L_1 \times L_2 \times L_3)}{L_1 \times L_2 \times L_3} \\ &= \varepsilon_{11}+\varepsilon_{22}+\varepsilon_{33} = trace(\bar{\bar{\varepsilon}}) \end{aligned} \tag{A.3}$$

APPENDIX B
Publications

Journals

1. M.F. Arif, N. Saintier, F. Meraghni, J. Fitoussi, Y. Chemisky, G. Robert, *Multi-scale fatigue damage characterization in short glass fiber reinforced polyamide-66*, Composites Part B, 61, 55–65, 2014.
2. M.F. Arif, F. Meraghni, Y. Chemisky, N. Despringre, G. Robert, *In situ damage mechanisms investigation of PA66/GF30 composite: Effect of relative humidity*, Composites Part B, 58, 487-495, 2014.

Conferences

1. M.F. Arif, F. Meraghni, N. Saintier, Y. Chemisky, J. Fitousi and G. Robert, *Fatigue damage investigation of PA66/GF30 by X–Ray Microtomography*, 16th European Conference on Composite Materials, 22-26 June, 2014, Seville–Spain.
2. N. Despringre, Y. Chemisky, M.F. Arif, G. Robert, F. Meraghni, *Multi-scale viscoelastic damage model of short glass fiber reinforced polyamide-66 under high-cycle fatigue*, 16th European Conference on Composite Materials, 22-26 June, 2014, Seville–Spain.
3. M.F. Arif, N. Saintier, F. Meraghni, Y. Chemisky, J. Fitoussi, G. Robert, *Fatigue damage characterization in short glass fiber reinforced polyamide-66*, 19th International Conference on Composite Materials, July 28-August 2, 2013, Montréal–Canada.
4. M.F. Arif, N. Despringre, Y. Chemisky, G. Robert, F. Meraghni, *In Situ damage mechanisms investigation of polyamide/short glass fiber composite*, 19th International Conference on Composite Materials, July 28-August 2, 2013, Montréal–Canada.
5. M.F. Arif, N. Despringre, Y. Chemisky, G. Robert, F. Meraghni, *In situ SEM damage mechanisms investigation of short glass fiber reinforced polyamide composite*, 18èmes Journées Nationales sur les Composites, 12-14 June 2013, Nantes–France.
6. M.F. Arif, F. Meraghni, N. Saintier, J. Fitoussi, G. Robert, *Experimental fatigue damage evaluation of short glass fiber reinforced polyamide composites*, 8th European solid mechanics conference, July 9-13, 2012, Graz–Austria.

MECANISMES D'ENDOMMAGEMENT DU POLYAMIDE-66 RENFORCE PAR DES FIBRES DE VERRE COURTES, SOUMIS A UN CHARGEMENT MONOTONE ET EN FATIGUE : INFLUENCE DE L'HUMIDITE RELATIVE ET DE LA MICROSTRUCTURE INDUITE PAR LE MOULAGE PAR INJECTION

RESUME : Le présent travail s'appuie sur une approche expérimentale étendue visant l'identification des mécanismes d'endommagement en chargement monotone et en fatigue du PA66/GF30, en prenant notamment en compte l'influence de la teneur en eau et de la microstructure induite par le moulage par injection. Les essais et les observations in situ au MEB mettent en exergue le rôle déterminant de l'humidité relative sur l'initiation, le niveau et la chronologie de l'endommagement. Une analyse par micro-tomographie aux rayons X sur des échantillons ayant subi un chargement de fatigue montre que l'endommagement augmente continuellement et progressivement au cours de la fatigue, et plus significativement dans la deuxième moitié de sa durée de vie. Les résultats obtenus en monotone et en fatigue révèlent des mécanismes d'endommagement similaires, notamment une décohésion des interfaces fibre/matrice. Une chronologie générale de l'endommagement est établie. Celui-ci s'initie en extrémités de fibres ou plus globalement là où les fibres sont relativement proches les unes des autres. Il s'ensuit des décohésions interfaciales se propageant le long des fibres. A une contrainte en flexion plus élevée, des microfissures de la matrice peuvent apparaître et se propager par coalescence, ce qui aboutira à la rupture. Ces résultats expérimentaux permettent d'alimenter une modélisation multi-échelles de l'endommagement à fort contenu physique. Celle-ci contribuera alors à une prédiction pertinente de l'endommagement dans les thermoplastiques renforcés pour application automobile.

Mots clés : Composites à matrice polymère, polyamide, moulage par injection, relation procédé-structure, mécanismes d'endommagement, essais in-situ (MEB), fatigue, tomographie, humidité relative.

DAMAGE MECHANISMS IN SHORT GLASS FIBER REINFORCED POLYAMIDE-66 UNDER MONOTONIC AND FATIGUE LOADING: EFFECT OF RELATIVE HUMIDITY AND INJECTION MOLDING INDUCED MICROSTRUCTURE

ABSTRACT: The current work focuses on extensive experimental approaches to identify monotonic and fatigue damage behavior of PA66/GF30 considering various effects such as relative humidity and injection process induced microstructure. By using in situ SEM tests, it was observed that relative humidity conditions strongly impact the damage mechanisms in terms of their initiation, level and chronology. The X-ray micro-tomography analysis on fatigue loaded samples demonstrated that the damage continuously increases during fatigue loading, but the evolution occurs more significantly in the second half of the fatigue life. From the results of damage investigation under monotonic and fatigue loading, it was established that both loading types exhibit the same damage mechanisms, with fiber/matrix interfacial debonding as the principal damage mechanisms. General damage chronologies were proposed as the damage initiates at fiber ends and more generally at locations where fibers are relatively close to each other due to the generation of local stress concentrations. Afterwards, interfacial decohesions further propagate along the fiber/matrix interface. At high relative flexural stress, matrix microcracks can develop and propagate, leading to the damage accumulation and then the final failure. The experimental findings are important to provide a physically based damage mechanisms scenarios that can be integrated into multiscale damage models. These models will contribute towards reliable predictions of damage in reinforced thermoplastics for lightweight automotive applications.

Keywords: polymer-matrix composites, polyamide, injection molding, process-structure relation, damage mechanisms, in situ SEM test, fatigue testing, tomography, relative humidity.

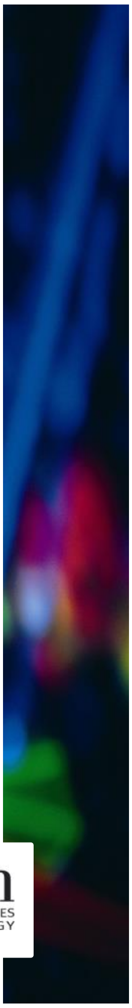

ARTS
ET MÉTIERS
ParisTech

ParisTech
INSTITUT DES SCIENCES ET TECHNOLOGIES
PARIS INSTITUTE OF TECHNOLOGY